

FLORIDA STATE UNIVERSITY
COLLEGE OF ARTS AND SCIENCES

PHOTOPRODUCTION OF CASCADE BARYONS USING THE GLUEX DETECTOR AT
JEFFERSON LABORATORY

By

ASHLEY ERNST

A Dissertation submitted to the
Department of Physics
in partial fulfillment of the
requirements for the degree of
Doctor of Philosophy

2020

Copyright © 2020 Ashley Ernst. All Rights Reserved.

Ashley Ernst defended this dissertation on July 1st, 2020.
The members of the supervisory committee were:

Volker Crede
Professor Directing Dissertation

Tomasz Plewa
University Representative

Simon Capstick
Committee Member

Paul Eugenio
Committee Member

Rachel Yohay
Committee Member

The Graduate School has verified and approved the above-named committee members, and certifies that the dissertation has been approved in accordance with university requirements.

”It is no good to try to stop knowledge from going forward.
Ignorance is never better than knowledge.”

- Enrico Fermi

ACKNOWLEDGMENTS

TABLE OF CONTENTS

List of Tables	vii
List of Figures	viii
Abstract	xiv
1 Introduction	1
1.1 Quantum Chromodynamics	1
1.1.1 Asymptotic Freedom	2
1.1.2 Confinement	3
1.2 Hadron Spectroscopy	3
1.2.1 Meson Spectroscopy	4
1.2.2 Baryon Spectroscopy	6
1.3 Cascade Baryons	7
1.3.1 Previous Experiments: Kaon Production	9
1.3.2 Previous Experiments: Photoproduction	11
2 GlueX Collaboration at Jefferson Lab	14
2.1 Continuous Electron Beam Accelerator Facility	14
2.2 The GlueX Beamline	16
2.2.1 The Bremsstrahlung Technique and the Tagger Hall	16
2.3 The GlueX Spectrometer	19
2.3.1 Target and Start Counter	19
2.3.2 Drift Chambers	21
2.3.3 Calorimetry	22
2.3.4 The Time-of-Flight Spectrometer	23
2.3.5 Detection of Internally Reflected Cherenkov Detector	27
3 Data Sets and Analysis Framework	29
3.1 Data Sets	29
3.2 Analysis Framework	29
3.2.1 Tagger Accidentals	33
3.2.2 Kinematic Fitting	34
4 Ground State Cascade Baryons $\Xi^-(1320)$ at GlueX	36
4.1 Event Selection: Kinematic Fitting	38
4.2 Events After Selection	40
5 Monte Carlo Event Simulation for $\Xi^-(1320)$	45
5.1 Monte Carlo Generation	45
5.2 Monte Carlo/Data Matching	46

6	Cross Section of $\Xi^-(1320)$	51
6.1	Fitting of Data	52
6.2	Monte Carlo Efficiency	53
6.3	Flux	54
6.4	Total Production Cross Section Results	55
6.5	Differential Cross Section	56
6.6	Systematic Errors and Studies	58
6.6.1	Phase Space Coverage	59
6.6.2	Effect of χ^2/NDF Cut	61
6.6.3	Signal Resolution and Stability	62
6.6.4	Effect of Binning and Fit Functions	63
6.6.5	Miscellaneous Studies	63
7	Search for Excited States	68
7.1	Channel Motivation for the Decay $\Xi^{-*} \rightarrow K^- \Lambda$	68
7.2	Event Selection	70
7.2.1	Second Look	72
7.3	Results	73
7.3.1	Second Look	76
8	Summary and Outlook	80
Appendix		
A	Tabulated Results	82
B	Decay Channels	83
	Bibliography	88
	Biographical Sketch	91

LIST OF TABLES

1.1	The current status of the Cascade resonances from the 2019 update of the PDG. Red denotes an assumption based on the quark model.[1]	8
1.2	The current status of the Cascade resonances from the 2019 version of the PDG compared to the status in 1981 and the results from the MPS [1][2]	11
3.1	The timing requirements for each relevant particle hypothesis in the 4 detectors with timing information [3].	31
A.1	The values for each run period used for the total cross section. The quoted uncertainty on all values is statistical.	82
B.1	Decay channels of interest and branching ratios from the PDG Review [1]	84

LIST OF FIGURES

1.1	The strong coupling constant as a function of momentum transfer Q . The points represent measurements from experiments and the curve is the prediction for QCD. Reproduced from [4] which is licensed under CC BY NC ND.	2
1.2	The pseudoscalar meson nonet (left) and the vector meson nonet (right) representing the ground state mesons with $L = 0$	4
1.3	The symmetric decuplet (left) and the mixed symmetry octet (right) from SU(3) flavor symmetry.	6
1.4	Lattice QCD predictions for Ξ baryons where the color denotes the flavor multiplet. [5]	9
1.5	(left) Schematic of the MPS; (right) Results of the experiment: (from top to bottom) detector acceptances, missing mass squared detector A and B. Reproduced from [2]. .	10
1.6	Schematic of the CLAS detector previously located in Hall B at Jefferson Lab [6]. . .	12
1.7	(left) Missing mass spectrum for $\gamma p \rightarrow K^+K^+(X)$, which shows a clear signal for $\Xi^-(1320)$ and $\Xi^-(1530)$. (right) Total production cross section for $\gamma p \rightarrow K^+K^+(X)$ for $\Xi^-(1320)$. Reproduced from [7].	13
1.8	(left) Missing mass spectrum for $\gamma p \rightarrow K^+K^+(X)$ for the CLAS g12 experiment (right) Total production cross section for CLAS g12 for $\gamma p \rightarrow K^+K^+(X)$ for $\Xi^-(1320)$. Reprinted figures with permission from [8] Copyright 2018 by the American Physical Society.	13
2.1	(Top) Schematic for the Continuous Electron Beam Accelerator Facility (CEBAF) at Jefferson Lab showing the 4 experimental halls. (Bottom) The aerial view of the accelerator with the individual experimental halls marked in red. Both are reproduced from [6]	15
2.2	Schematic for the GlueX beamline. Reproduced from [?].	16
2.3	An example of the flux determined by the PS and the degree of polarization obtained from the TPOL. Reproduced from [9]	18
2.4	An image of the pair spectrometer in the hall. The beam travels from left to right across the image.	19
2.5	Schematic of the overall GlueX detector located in Hall D at Jefferson Lab. Reproduced from [10].	20
2.6	Schematic of the start counter detector and the target cell. Reproduced from [11]. . .	20

2.7	Image of the central drift chamber (left) and forward drift chamber (right). Reproduced from [12].	22
2.8	Image of the barrel calorimeter prior to it being placed into the solenoid (left) and forward calorimeter without the front cover to show the crystals (right). Reproduced from [12].	23
2.9	Image of the time of flight spectrometer in the hall prior to the upgrade but with the inclusion of the Lucite shielding.	24
2.10	The cross section of the Time-of-Flight spectrometer before and after the implementation of the Lucite shielding.	26
2.11	A diagram of the Time-of-Flight spectrometer demonstrating the increased segmentation and beam hole size.	26
2.12	A schematic for the placement of the DIRC within the GlueX detector. [13]	27
3.1	Example of a β plots for the Time-of-Flight spectrometer for positively charged candidates and negatively charged candidates. Taken from the monitoring histograms produced for run 51582 of the Fall 2018 run period	30
3.2	(left) Example of a Δt plot for the Time-of-Flight spectrometer for K^+ candidates and (right) of the energy deposition in the Central Drift Chamber. Both plots were taken from the monitoring histograms produced for run 51582 of the Fall 2018 run period.	32
3.3	Example of the beam bunch distribution for the Spring 2017 data set.	33
4.1	Feynman diagrams for photoproduction of the octet ground state Ξ baryons. The top diagram is for a negatively-charged $\Xi(1320)$ while the bottom diagrams are the two production mechanisms for $\Xi^0(1320)$	37
4.2	Simulations for momentum vs polar angular for all tracks where the red box denotes the kaon-pion separation currently possible in the TOF. The three high intensity regions consist of kaons, kaons and protons, and pions from highest momentum to lowest. Reproduced from [14].	37
4.3	Invariant mass spectrum for $\Xi^-(1320) \rightarrow \Lambda\pi^-$ versus the χ^2/NDF from the kinematic fit in the Spring 2017 data set (top left), Spring 2018 (top right), Fall 2018 (bottom left). The yields in the slice of $\Lambda\pi^-$ mass containing $\Xi^-(1320)$ as a function of the χ^2/NDF for data and Monte Carlo. All distributions are flat beyond χ^2/NDF of 15. (bottom right).	39
4.4	Invariant mass spectrum for $\Xi^-(1320) \rightarrow \Lambda\pi^-$ in the Spring 2017 data set (top), Spring 2018 (middle), and Fall 2018 (bottom).The left column shows the $\Lambda\pi^-$ invariant mass using the measured and kinematically fit 4-momenta while the right shows the overall fit of the data.	41

4.5	Measured momentum vs polar angle distributions for events within the $\Xi^-(1320)$ mass peak for the Spring 2017 run period. The distributions are for the two kaons (top left), two pions (top right), and the proton (bottom).	42
4.6	Vertex locations in the GlueX coordinate system for the production vertex, the decay vertex of Ξ , and the decay vertex of Λ for Spring 2017 (top left), Spring 2018 (top right), and Fall 2018 (bottom).	43
4.7	(left) The $-t$ distributions for each of the different run periods.(right) The invariant mass of the intermediate hyperon formed from the low momentum kaon and Ξ	44
5.1	Efficiency by run number for each of the different run periods: Spring 2017 (top left), Spring 2018 (top right), and Fall 2018 (bottom)	46
5.2	The comparison of the momentum (left) and polar angle (right) for the two kaons in Monte Carlo. K_2 denotes the kaon from the decay of the intermediate hyperon and K_1 denotes the initial kaon produced at the production vertex.	47
5.3	The distributions of $-t$ for Fall 2018 (blue) and varying input parameter tests. The colors represent different input t -slopes, across a row increases the width of the intermediate hyperon (0.4, 0.6, 0.8, 1.0 GeV), and down a column increases the mass (2.0, 2.4, 2.8 GeV).	48
5.4	The distributions of $-t$ for each of the data sets with the chosen input parameters for generation of t -slope = 1.4 GeV^{-2} , and an intermediate of mass 2.0 GeV and width 0.4 GeV.	49
5.5	Kinematic comparison between data and Monte Carlo. The left histograms show the momentum distributions while the right column show polar angle distributions. The top row is for kaons, middle is pions, and bottom row is the proton.	50
6.1	(left) The signal yields for Spring 2017 (green), Spring 2018 (red), and Fall 2018 nominal energy range (blue) resulting from the fits to each bin. (right) The fit for the low energy data from the Fall 2018 run period.	52
6.2	The Monte Carlo efficiency for Spring 2017 (green), Spring 2018 (red), and Fall 2018 nominal energy range (blue) found by dividing the yields in Monte Carlo by the amount of events generated.	53
6.3	The incoming beam flux as a function of beam energy for Spring 2017 (green), Spring 2018 (red), Fall 2018 nominal energy range (blue), and Fall 2018 low energy range (violet).	54
6.4	The total production cross section for $\gamma p \rightarrow K^+ K^+ \Xi^-$ as a function of beam energy for Spring 2017 (green), Spring 2018 (red), Fall 2018 nominal energy range (blue), and Fall 2018 low energy range (violet).	55

6.5	The efficiency and differential production cross section for $\gamma p \rightarrow K^+ K^+ \Xi^-$ as a function of momentum transfer to the kaon for Spring 2017 (green), Spring 2018 (red), and Fall 2018 nominal energy range (blue).	56
6.6	The differential production cross section on a log scale for $\gamma p \rightarrow K^+ K^+ \Xi^-$ as a function of momentum transfer to the kaon and beam energy for Spring 2017 (green), Spring 2018 (red), and Fall 2018 nominal energy range (blue).	57
6.7	The differential production cross section on a linear scale for $\gamma p \rightarrow K^+ K^+ \Xi^-$ as a function of momentum transfer to the kaon and beam energy for Spring 2017 (green), Spring 2018 (red), and Fall 2018 nominal energy range (blue).	58
6.8	Depiction of the Gottfried-Jackson reference frame in which the intermediate hyperon is at rest and the z -axis is along the beam direction.	60
6.9	Polar angle vs azimuthal angle for the decay kaon in the Gottfried-Jackson rest frame of the intermediate hyperon for data (left) and Monte Carlo (right) for the Spring 2017 data set.	60
6.10	Polar angle vs azimuthal angle for the decay kaon in the Gottfried-Jackson rest frame of the intermediate hyperon for generated Monte Carlo (left) and the difference in the reconstructed and thrown polar angles (right) for the Spring 2017 data set.	61
6.11	The total production cross section for $\gamma p \rightarrow K^+ K^+ \Xi^-$ as a function of χ^2/NDF for the kinematic fit for Spring 2017 (green), Spring 2018 (red), and Fall 2018 nominal energy range (blue).	62
6.12	The mass (left) and width (right) for $\Xi^-(1320)$ for $\gamma p \rightarrow K^+ K^+ \Xi^-$ as a function of beam energy for Spring 2017 (green), Spring 2018 (red), and Fall 2018 nominal energy range (blue).	63
6.13	The total production cross section for $\gamma p \rightarrow K^+ K^+ \Xi^-$ as a function of beam energy for Spring 2017 with variations in energy range width (left) and energy range start values (right).	64
6.14	The total production cross section for $\gamma p \rightarrow K^+ K^+ \Xi^-$ as a function of incoming beam energy for the Spring 2017 data set with (light green) and without (dark green) the scaling factor included in the accidental subtraction.	64
6.15	The total production cross section for $\gamma p \rightarrow K^+ K^+ \Xi^-$ as a function of incoming beam energy for the Spring 2017 data set using the generated beam energy (dark green) and reconstructed beam energy (light green) in the determination of the efficiency.	66
6.16	The total production cross section for $\gamma p \rightarrow K^+ K^+ \Xi^-$ as a function of incoming beam energy for the Spring 2017 data set using the nominal uniqueness tracking and tracking all particles.	67
7.1	A depiction of the quark placement for a Cascade baryon.	69

7.2	The quark line drawings for examples of the two major decays of an excited Cascade baryon within the first excitation band. If the excitation is between the strange quark pair, as with the lowest mass excitation, the state preferentially decays to KY or $K\Lambda$ as shown in the figure.	70
7.3	Feynman diagram for the reaction $\gamma p \rightarrow K^+ K^+ \Xi^{-*} \rightarrow K^+ K^+ K^- \Lambda$	70
7.4	Example plot for momentum vs polar angular for all the experimental K^+ tracks for the Fall 2018 data set.	71
7.5	Possible reconstruction chains for background reaction $\gamma p \rightarrow \phi N^* \rightarrow K^+ K^+ K^- \Lambda$. . .	72
7.6	(left) Invariant mass histogram of $K^+ K^-$ showing strong signal for ϕ background; (right) Invariant mass of $p\pi^-$ versus the invariant mass $K^+ K^-$ showing clean signal Λ signal and clear correlation with ϕ	72
7.7	The distribution of the $K^- \Lambda$ invariant mass while stepping through the values for χ^2/NDF for Spring 2017 (green), Spring 2018 (red), and Fall 2018 (blue).	73
7.8	The distribution of the $K^- \Lambda$ invariant mass while stepping through the values for the flight significance for Spring 2017 (green), Spring 2018 (red), and Fall 2018 (blue). . .	74
7.9	The distribution of the $K^- \Lambda$ invariant mass versus χ^2/NDF (left) and versus the flight significance of Λ for the Fall 2018 data set.	74
7.10	Invariant mass spectrum for ΛK^- for Spring 2017 (top left), Spring 2018 (top right), and Fall 2018 (bottom left). The combined distributions is shown in the bottom right. This decay channel has known branching ratios for the states: $\Xi^-(1690)$, $\Xi^-(1820)$, $\Xi^-(1950)$, $\Xi^-(2030)$, and $\Xi^-(2120)$ [1].	75
7.11	The fitted invariant mass spectrum for ΛK^- for Spring 2017 (top left), Spring 2018 (top right), and Fall 2018 (bottom left). The combined distributions is shown in the bottom right. This decay channel has known branching ratios for the states: $\Xi^-(1690)$, $\Xi^-(1820)$, $\Xi^-(1950)$, $\Xi^-(2030)$, and $\Xi^-(2120)$ [1].	77
7.12	The invariant mass spectrum for ΛK^- for Spring 2017 (green), Spring 2018 (red), and Fall 2018 (blue) with the new selection requirements.	78
7.13	The new fitted invariant mass spectrum for ΛK^- for Spring 2017 (top left), Spring 2018 (top right), and Fall 2018 (bottom left). The combined distributions is shown in the bottom right. This decay channel has known branching ratios for the states: $\Xi^-(1690)$, $\Xi^-(1820)$, $\Xi^-(1950)$, $\Xi^-(2030)$, and $\Xi^-(2120)$ [1].	79
B.1	Possible reconstruction chains of interest for $\Xi \rightarrow \Lambda\pi$, the octet ground state using the previously mentioned decays. Branching ratios are those from the PDG and current as of the 2019 update [1].	83

B.2	Possible reconstruction chains of interest for $\Xi^* \rightarrow \Xi\pi$ using the previously mentioned decays. Branching ratios are those from the PDG and current as of the 2019 update [1].	85
B.3	Possible reconstruction chains of interest for $\Xi^* \rightarrow \Lambda K$ using the previously mentioned decays. Branching ratios are those from the PDG and current as of the 2019 update [1].	85
B.4	Possible reconstruction chains of interest for $\Xi \rightarrow \Xi\gamma$ using the previously mentioned decays. Branching ratios are those from the PDG and current as of the 2019 update [1].	86
B.5	Possible reconstruction chains of interest for $\Xi^* \rightarrow \Sigma K$ using the previously mentioned decays. Branching ratios are those from the PDG and current as of the 2019 update [1].	86
B.6	Possible reconstruction chains of interest for $\Xi^* \rightarrow \Xi\pi\pi$ through a three-body decay or via a two-body decay with an intermediate $\Xi(1530)$ using the previously mentioned decays in B.2. Branching ratios are those from the PDG and current as of the 2019 update [1].	87
B.7	Possible reconstruction chains of interest for $\Xi^* \rightarrow K\Lambda\pi$ using the previously mentioned decays. Branching ratios are those from the PDG and current as of the 2019 update [1].	87

ABSTRACT

Multi-strange baryons have played an important role in understanding the strong interaction. Despite their importance to advancing quantum chromodynamics (QCD), little is known about such hyperons due to the lack of a strange probe. Almost all knowledge of Cascade baryons today stems from kaon-nucleon interactions in bubble chamber experiments performed in the 1960s and 1970s, of which only the octet and decuplet ground states, $\Xi(1320)$ and $\Xi(1530)$ respectively, are well established. This research uses the GlueX experiment at Jefferson Laboratory to map out the spectrum of doubly-strange Cascade resonances that have little or no evidence, as well as measure the cross section for $\Xi^-(1320)$ in hopes to further understand the relevant degrees of freedom of quantum chromodynamics. The first phase of GlueX running has recently been completed. As a result, this is the ideal time to search for the unknown Cascade resonances and measure their properties.

CHAPTER 1

INTRODUCTION

Modern Nuclear physics has many open questions with answers still being worked towards. The Nuclear Science Advisory Committee (NSAC) composes a long range plan for the field every 4-8 years. This long range plan is the basis of which funding is provided and frames the major open questions of interest for the field as a whole. The current open questions include [15]: How does matter emerge? How do subatomic particles arrange themselves? Is there more to learn about the four fundamental forces? How can nuclear physics benefit society?

The work presented here is in regards to the second question, "how do subatomic particles arrange themselves?" All matter is composed of elementary particles, particularly the quarks and leptons of the standard model. The standard model is composed of six quarks (up/down, charm/strange, and top/bottom), six leptons (electrons, muons, taus, and their corresponding neutrinos), and four force carriers or gauge bosons (W^\pm/Z bosons, photon, and gluon). The four fundamental forces of nature associated with these force carriers listed in increasing strength are gravity, weak nuclear force (W^\pm/Z bosons), electromagnetic force (photon), and the strong nuclear force (gluon). With the exception of gravity, these forces interact through the mediation of a known force carrier.

The electromagnetic force accounts for the binding of the nucleus with the electrons in an atom. Within the nucleus, nucleons, protons and neutrons, are bound to each of other by the strong force. Nucleons are composed of quarks, specifically the lightest quarks (up and down). These quarks, along with the gluon, are bound together by the strong force. The strong interaction is described by the quantum field theory known as quantum chromodynamics (QCD).

1.1 Quantum Chromodynamics

Hadrons, such as nucleons, are any composite particle of quarks and gluons that are bound by the strong interaction. The theory of QCD is analogous to the theory of electromagnetism on small scales, Quantum Electrodynamics (QED). QED represents the interaction between charged

particles through the exchange of photons. In QED, the photons interact through the electric charge. Since photons do not have electric charge, they do not interact with other photons. While in QCD, the gluons interact with the color charge and do have color charge themselves. This allows gluons to be able to interact among themselves. Another peculiarity is the strength of the interaction at different energy scales which leads to two unique features: asymptotic freedom and confinement.

1.1.1 Asymptotic Freedom

Asymptotic freedom describes the characteristic of the interaction strength between any two strongly interacting particles at high momentum transfer Q . The distance between two quarks is inversely proportional to the momentum transfer between them. As the distance between two quarks decreases, or Q increases, the strength of the interaction decreases.

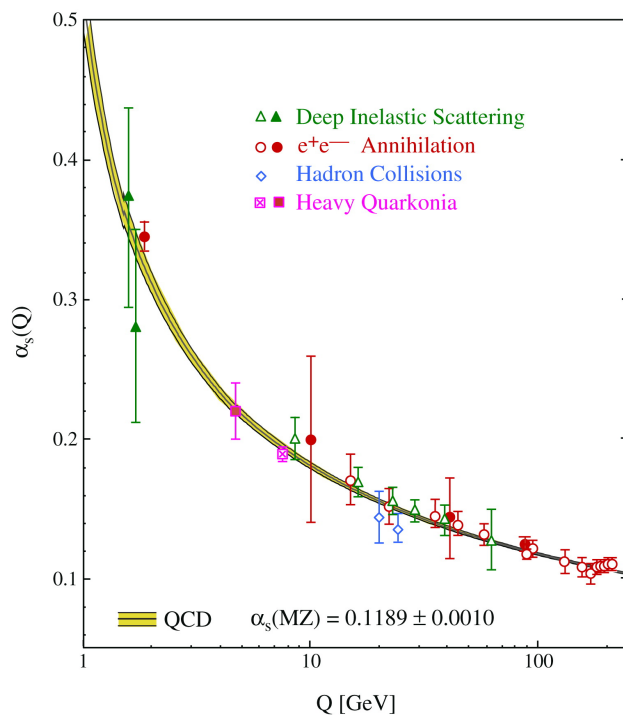


Figure 1.1: The strong coupling constant as a function of momentum transfer Q . The points represent measurements from experiments and the curve is the prediction for QCD. Reproduced from [4] which is licensed under CC BY NC ND.

The characteristic strength of the interaction is denoted by the coupling constant, α_s . The function of the coupling strength as a function of the momentum transfer is shown in figure 1.1[4]. It can

be seen that at high momentum transfers, the coupling strength vanishes asymptotically. This feature was first explained mathematically by David Gross and Frank Wilczek [16] and independently by H. David Politzer [17] in 1973, awarding all three of them the Nobel prize in 2004.

1.1.2 Confinement

Confinement is the effect at low momentum transfer or large distances. This property describes the effect in which the quarks are confined within hadrons. Analogous to the electric charge in QCD, each of the constituents carry a charge, referred to as the color charge. There are three types of color charge: red, blue, and green and the corresponding anti-colors: anti-red, anti-blue, and anti-green. Confinement, or more precisely color confinement is the notion that all particles must be color neutral. Color neutral can be achieved in two ways, the combination of a color and its anti-color or all the colors (or anti-colors) combined together. Consequently, hadrons come mainly in two forms: mesons and baryons. A meson is a boson (integer spin) consisting primarily of a quark and antiquark. A baryon is a fermion (half integer spin) composed of three quark.

As quarks themselves are not color neutral, 'free' quarks do not appear in nature. The strength of the strong interaction increases as the distance between two quarks increases. The energy required to separate a quark from a hadron is greater than that of production of a quark anti-quark pair. Since coupling strength of QCD at these energy scales is so large, QCD is not able to be solve via perturbative methods, and is referred to as the non-perturbative regime. The non-perturbative regime is not solvable via analytical methods and thus there is no theoretical proof for confinement unlike asymptotic freedom, as shown by Gross, Wilczek, and Politzer.

1.2 Hadron Spectroscopy

Much like that of atomic spectroscopy, hadron spectroscopy seeks to understand the spectrum of particles. Hadrons have previously been described as mesons or baryons, which are composed of a quark anti-quark pair or three quarks, respectively. These quarks, known as valence quarks, give rise to the quantum numbers of the hadrons they compose. Hadrons additionally contain gluons and an infinite 'sea' of quark anti-quark pairs that do not contribute to the overall quantum numbers of a given hadron. Thus in further discussions regards the quantum numbers of mesons and baryons, only the valence quarks are considered. Since QCD is non-perturbative in this energy

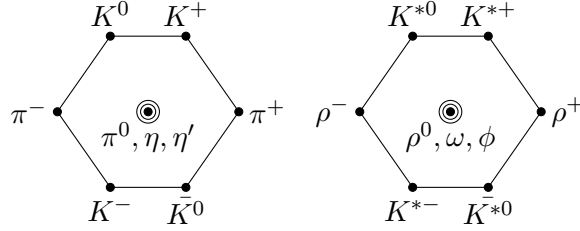


Figure 1.2: The pseudoscalar meson nonet (left) and the vector meson nonet (right) representing the ground state mesons with $L = 0$.

range, its properties are studied through the exploration of the spectrum of hadrons. It is of particular interest how the quarks and gluons give rise to the excited spectrum of hadrons.

The quantum numbers used to describe a hadron include the total angular momentum J , the parity P , and the isospin I . The total angular momentum quantum number, J , is frequently referred to as the spin. It is the combination of the orbital angular momentum l and the intrinsic spin s . Parity represents the invariance under spatial transformations. Isospin reveals that there are $2I + 1$ different charged states exist with the same quantum numbers. For example, the nucleon has isospin $1/2$ resulting in two charges states, namely the proton and the neutron.

1.2.1 Meson Spectroscopy

While not the directly related to this work, meson spectroscopy, particularly mapping the spectrum of exotic mesons, is the main motivation for the GlueX collaboration which will be discussed extensively for the remainder of this report. The meson multiplets can be constructed using $SU(3)$ flavor symmetry, where the 3 denotes the three lightest quark flavors: up, down, and strange. For ground state mesons, this results in the multiplet structure of $\mathbf{3} \otimes \bar{\mathbf{3}} = \mathbf{8} \oplus \mathbf{1}$. Each of these values represent the dimensions of the irreducible multiplet. Unlike the baryons discussed in section 1.2.2, the octet and singlet are not generally considered independent. In principle, there are two non-strange, isospin zero states in which one belongs to the octet and one to the singlet. The octet state is constructed without the use of strange quarks and the singlet state is pure $s\bar{s}$. These two states are not eigenstates and therefore, the two wave-functions mix. The resulting mixing angle stems from the diagonalization of the mass matrix to the observed states.

The η meson in each the octet and in the singlet, typically denoted η_8 and η_1 . These two eigenstates mix resulting in the observed particles η and η' , which are included in a nonet of

pseudoscalar mesons with $J^P = 0^{-+}$ for the ground state, as shown in figure 1.2. There is also a nonet of heavier particles, referred to as vector mesons with $J^P = 1^{--}$. Similar to the pseudoscalar mesons, the eigenstates of this multiplet are ω_8 and ω_1 which mix to form the observed hadrons ω and ϕ .

Allowed Quantum Numbers. Hadrons are typically identified by their name, mass, and spin-parity measurements J^P . The parity of a hadron has two components: the intrinsic parity ± 1 and the orbital momentum contribution $(-1)^l$. Due to the antiquark in mesons, the intrinsic parity is negative, while baryons are positive. Neutral mesons are assigned an additional quantum number the charge conjugation or C-parity which represents the behavior under the symmetry operator of changing the sign of all "charges." Charge conjugation flips all the internal quantum numbers of a state (charge, flavor, baryon, and lepton numbers). When applied to a state, the result is its antiparticle, therefore, it is only a relevant quantum number for particles that are their own antiparticles, specifically only neutral mesons [1]. The value for charge conjugation is found using $C = (-1)^{l+s}$. This can be extended to G-parity which includes states that are not flavor neutral. G-parity can be found by $G = (-1)^{I+l+s}$, where I is the isospin of the meson.

Exotics are considered all hadrons that differ from the ordinary quark structure of $q\bar{q}$ for mesons and qqq for baryons. Due to the negative intrinsic parity for mesons, there are certain combinations of quantum numbers that are not possible. The quantum numbers for a meson are defined such that:

$$P = (-1)^{l+1} \qquad C = (-1)^{l+s} \qquad J = l + s \qquad (1.1)$$

There are two possibilities for s , 0 for anti-aligned spins and 1 for aligned spins. It can be seen that the allowed quantum numbers for mesons include:

$$J^{PC} = 0^{-+}, 0^{++}, 1^{--}, 2^{++}, \dots \qquad (1.2)$$

. There are clearly combinations that are not allowed with the conventional view of mesons. If the gluons are considered and are allowed degrees of freedom within the meson, the other quantum numbers become accessible. These include:

$$J^{PC} = 0^{+-}, 0^{-+}, 1^{-+}, 2^{+-}, \dots \qquad (1.3)$$

1.2.2 Baryon Spectroscopy

Baryons are strongly interacting fermions, which generally consist of 3 quarks. The strong interaction between any quark pair is independent of flavor and is the dominating term in the interaction Hamiltonian. Therefore, SU(3) flavor symmetry may be considered among the up, down, and strange quarks. The flavor symmetry results in $\mathbf{3} \otimes \mathbf{3} \otimes \mathbf{3} = \mathbf{10}_S \oplus \mathbf{8}_{MS} \oplus \mathbf{8}_{MA} \oplus \mathbf{1}_A$, which can be found using the Young Tableau formulation from group theory [1]. All particles in each multiplet, as seen in figure 1.2.2, should have the similar properties. The ground state decuplet is entirely symmetric in terms of quark flavor while the ground state octet has mixed symmetry and is either symmetric or antisymmetric under the exchange of two quarks. The wavefunction of a baryon must be overall antisymmetric and consists of four components: flavor ϕ , spin χ , spatial ψ_l , and color C .

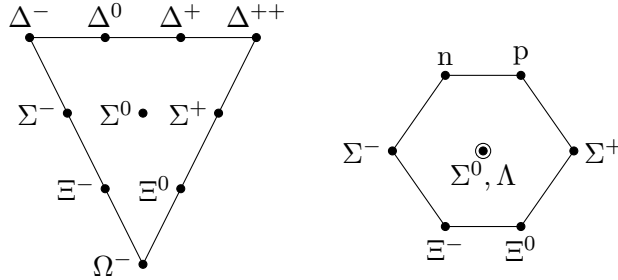


Figure 1.3: The symmetric decuplet (left) and the mixed symmetry octet (right) from SU(3) flavor symmetry.

The flavor and spin are commonly coupled together resulting in an overall symmetry of SU(6) by $SU(3) \otimes SU(2) = SU(6)$, which decomposes to $\mathbf{6} \otimes \mathbf{6} \otimes \mathbf{6} = \mathbf{56}_S \oplus \mathbf{70}_{MS} \oplus \mathbf{70}_{MA} \oplus \mathbf{20}_A$. Analogous to the harmonic oscillator, excitation bands can be formed by combining the multiplets with units of orbital angular momentum. The excitation bands are commonly referred to by their multiplet and the total orbital angular momentum between the oscillators and parity l^P . All observed hadrons are a part of the color singlet C^A , which requires that a baryon wave function must be overall symmetric in the remaining three components.

For the decuplet, the flavor wavefunction is entirely symmetric and may couple to spin to be overall symmetric or mixed symmetry. To make the overall wavefunction antisymmetric, the spatial portion must be symmetric or mixed, respectively. For the ground state, the symmetric

spatial portion is $L = 0$ resulting in the wavefunction $\phi^S \chi^S \psi_0^S C^A$. This results in a spin-parity of $J^P = \frac{3}{2}^+$.

For the octet, coupling the flavor wavefunction to spin results in a flavor-spin symmetry of either symmetric, mixed, or antisymmetric. To create the overall wavefunction, the spatial component must be symmetric, mixed, or antisymmetric in nature. The ground state octet baryons must have $l = 0$ orbital momentum and therefore flavor and spin couple together symmetrically. The resulting ground state wavefunction is $\frac{1}{\sqrt{2}}(\phi^{MS} \chi^{MS} + \phi^{MA} \chi^{MA}) \psi_0^S C^A$.

The ground state octet have spin parity of $J^P = \frac{1}{2}^+$. Both the decuplet and the octet ground states are a part of the $[56, 0^+]$ ground state band. Higher excitation bands require more orbital angular momentum within the baryon and result in more complicated wavefunctions for the flavor and spin in order to remain overall antisymmetric of the baryons, as later discussed in section 7.1.

Baryons are not bound by the charge conjugation invariance and therefore have no combinations of quantum numbers that are not allowed. Exotic baryons are those that are different from the qqq state, such as the pentaquark which is a baryon consisting of four quarks and an anti-quark. Since quantum numbers alone can not identify if a baryon is exotic, the internal structure has to be studied to determine through other means.

The strange baryons are considered the bridge between light-flavor and heavy-flavor regimes. These hadrons are essential in determining the relevant degrees of freedom of quantum chromodynamics in the non-perturbative regime. Experimentally, the strangeness is costly to produce in terms of energy with the lack of a strange probe resulting in little being known about the spectrum. With each additional strange quark, less is known about the corresponding hyperons.

1.3 Cascade Baryons

The Cascade baryons, Ξ , are doubly-strange baryons, which are either $|uss\rangle$ or $|dss\rangle$ in quark content. There are only two states in which the existence is certain and four states in which the existence is very likely [1]. Flavor SU(3) symmetry implies that particles within the same multiplet have similar properties, and only differ in quark content. Therefore, by not discriminating by charge, there should be as many Ξ states as there are N^* and Δ^* states combined in which the Particle Data Group (PDG) lists 25 with very likely existence [1]. The quantum numbers of the strange hadrons are mostly unknown. The spin-parity measurements J^P in the PDG table rely

heavily on quark model predictions such that all parity values are predictions. The understanding of the Cascade baryons has remained mostly unchanged since 1988 [1]. A summary of the previously observed Cascade baryons is shown in table 1.3. This table includes the masses of the known states as well as their total spin and parity, J^P . Additionally, each state and decay mode is given a star rating ranging from zero stars to four stars that denote the amount of evidence available for a particular state. Four stars represents that the existence of the state is certain, three is very likely, two is evidence is fair, one is evidence is poor, and zero is no evidence [1].

Table 1.1: The current status of the Cascade resonances from the 2019 update of the PDG. Red denotes an assumption based on the quark model.[1]

Particle	J^P	Overall Status	– Status as seen in –			
			$\Xi\pi$	ΛK	ΣK	$\Xi(1530)\pi$
$\Xi(1318)$	$1/2^+$	****				
$\Xi(1530)$	$3/2^+$	****	****			
$\Xi(1620)$		*	*			
$\Xi(1690)$		***		***	**	
$\Xi(1820)$	$3/2^-$	***	**	***	**	**
$\Xi(1950)$		***	**	**		*
$\Xi(2030)$	$5/2^?$	***		**	***	
$\Xi(2120)$		*		*		
$\Xi(2250)$		**				
$\Xi(2370)$		**				
$\Xi(2500)$		*		*	*	

For the known lower mass resonances, the widths Γ are only 10-20 MeV, which is 5-30 times narrower than the corresponding N^* and Δ^* states. The octet ground state $\Xi(1320)$ decays weakly, which results in a long lifetime relative to strongly decaying hadrons. This lifetime corresponds directly to the width as $\Gamma = 1/\tau$ resulting in a much smaller width than the strongly decaying N^* and Δ^* states.

The Lagrangian of QCD is not able to be solved analytically in the non-perturbative regime. Numerical approximations are considered in what is known as Lattice QCD. Using Lattice QCD, a large amount of Cascade baryon states are predicted. The results from the Hadron Spectrum collaboration are shown in figure 1.4 [5]. The colors of the states are used to distinguish between the two SU(3) flavor multiplets, yellow being decuplet and blue the octet. The two lowest excitation

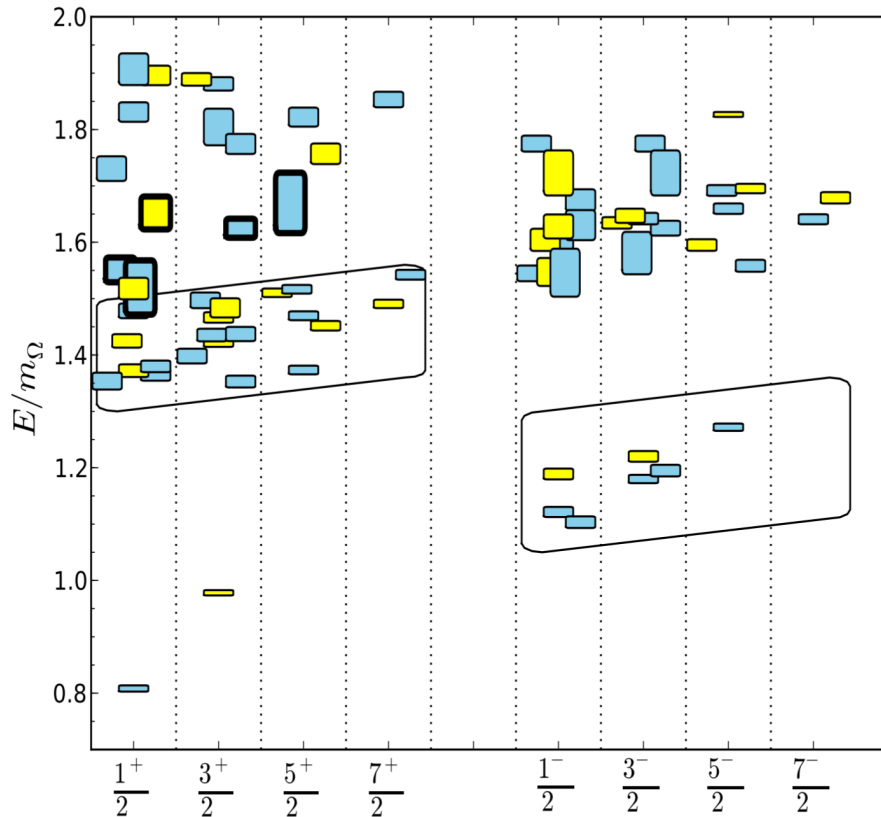


Figure 1.4: Lattice QCD predictions for Ξ baryons where the color denotes the flavor multiplet. [5]

bands are marked. As can be seen, all the excited states in the first excitation band are at or lower than 2 GeV in mass. The discussion of these first excitation band states continues in section 7.1.

1.3.1 Previous Experiments: Kaon Production

Cascade spectroscopy has been mainly studied through kaon beams in the 1960s through 1980s, primarily at the Lawrence Radiation Laboratory and Brookhaven National Laboratory. These studies have resulted in little progress due to the low-intensity and technological limitations, both in electronics and computing. The first of these experiments was performed in low-sensitivity bubble chamber experiments and the latter of which were able to include electronics to help improve the sensitivity and statistics [1]. These kaon-induced experiments have provided much of what is

currently known about the Cascade baryons. During this time period, only $\Xi(1320)$ and $\Xi(1530)$ were certain to exist and were classified into the $[56, 0^+]$ ground state band. Several experiments also showed decent evidence for the existence of $\Xi(1820)$ and $\Xi(2030)$ though only the total spin of the $\Xi(1820)$ was able to be determined [18, 19]. Several other resonances were seen from the many experiments though their existence could never be distinguished from statistical fluctuations.

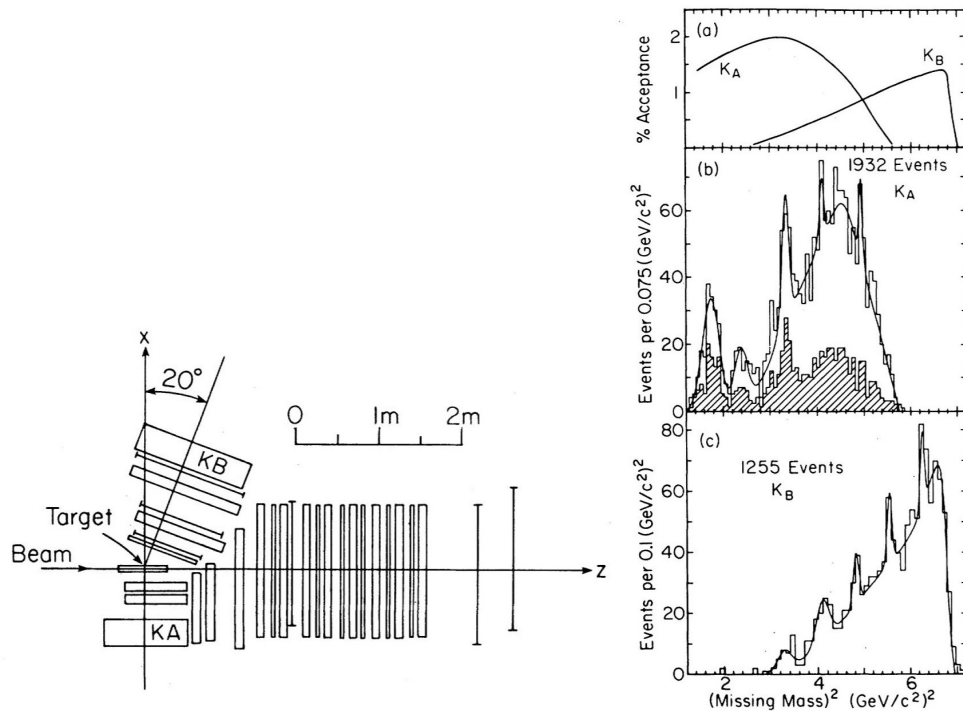


Figure 1.5: (left) Schematic of the MPS; (right) Results of the experiment: (from top to bottom) detector acceptances, missing mass squared detector A and B. Reproduced from [2].

MultiParticle Spectrometer. One such experiment was at the MultiParticle Spectrometer (MPS) at Brookhaven National Laboratory in the 1980s. This experiment studied the reaction $K^-p \rightarrow K^+(X^-)$ where (X) was the missing mass. The MPS consisted of two kaon detectors arranged as seen in figure 1.5, which were able to identify low momentum K^+ mesons as well as additional detectors downstream from the target to identify the decay product Λ from the Cascade baryon. The mass of the incident particle was calculated from the range through the detector and the momentum and then was cut upon to separate the kaons from the pions and protons. A Ξ

resonance was determined from the missing mass and was considered a signal if the cross section as a function of incident kaon momentum was consistent with that from the CERN bubble chamber experiment from the Amsterdam-CERN-Nijmegen-Oxford Collaboration [2]. The two detectors have different acceptances and thus the signal from each were analyzed separately. The resultant missing mass squared histograms for each are shown in figure 1.5 where the shaded region denotes the detection of a Lambda from the decay of the Cascade baryon. Many Cascade baryon resonances were seen in these spectra, as seen in the table 1.3.1.

Table 1.2: The current status of the Cascade resonances from the 2019 version of the PDG compared to the status in 1981 and the results from the MPS [1][2]

Current Particle	Current Status	Previous Mass	Previous Status	Mass from MPS (MeV)
$\Xi(1318)$	****	1320	****	1320 ± 6
$\Xi(1530)$	****	1530	****	1541 ± 12
$\Xi(1620)$	*	1630	**	
$\Xi(1690)$	***	1680	**	
$\Xi(1820)$	***	1820	***	1822 ± 6
$\Xi(1950)$	***	1940	**	
$\Xi(2030)$	***	2030	***	2022 ± 7
$\Xi(2120)$	*	2120	*	
$\Xi(2250)$	**	2250	*	2214 ± 5
$\Xi(2370)$	**	2370	**	2356 ± 10
$\Xi(2500)$	*	2500	**	2505 ± 10

1.3.2 Previous Experiments: Photoproduction

The CEBAF Large Acceptance Spectrometer (CLAS) collaboration operating the CLAS detector in Hall B at Jefferson Laboratory is interested in a large range of nuclear physics topics. The detector was designed such that there was high momentum resolution and geometric coverage for charged particles and no magnetic field around the target [20]. The detector consisted of several sub-detectors used to track particle paths and flight times, and a schematic of the detector can be seen in figure 1.6.

CLAS g11. One of the hadron spectroscopy experiments was that known as 'g11.' It was a photoproduction experiment conducted from May to July 2004 [7]. The experiment ran with a beam energy range of 1.60–3.85 GeV. The Cascade baryons were studied with an inclusive reaction

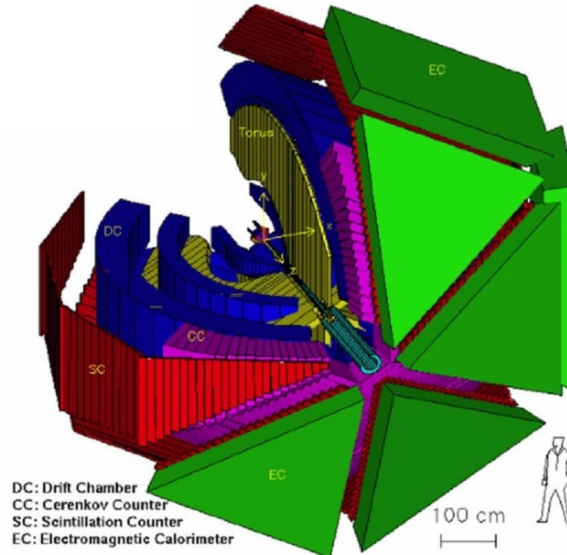


Figure 1.6: Schematic of the CLAS detector previously located in Hall B at Jefferson Lab [6].

$\gamma p \rightarrow K^+ K^+(X)$ for $\Xi^-(1320)$ and $\gamma p \rightarrow K^+ K^+ \pi^-(X)$ for $\Xi^-(1530)$ where X denotes a missing particle.

This experiment saw approximately 7,700 $\Xi^-(1320)$ s with a mass resolution of about 6.7 MeV, as shown in figure 1.7 [7]. From these events, the first photoproduction measurements of the $\Xi^-(1320)$ total production cross section were determined, as well as differential cross sections in terms of angular distributions. A t -channel production model was developed as an extension from the previous Kaon production experiments [21].

CLAS g12. Another spectroscopy experiment run by the CLAS collaboration was that of CLAS g12. This experiment ran from March to June 2008. The nominal beam energy and overall statistics for this run period were higher than that of g11.

Compared to the previous experiment, more events were seen for $\Xi^-(1320)$ with approximately 11,000 events [8]. The total cross section was also able to be extended to higher energies as the nominal beam energy was increased. The total cross section is shown in Figure ?? with only the inclusion of statistical errors. The systematic uncertainties contribution an additional 8.8% overall uncertainty to each point [8]. The production cross section appears to level off with increasing energy which will be discussed in chapter 6.

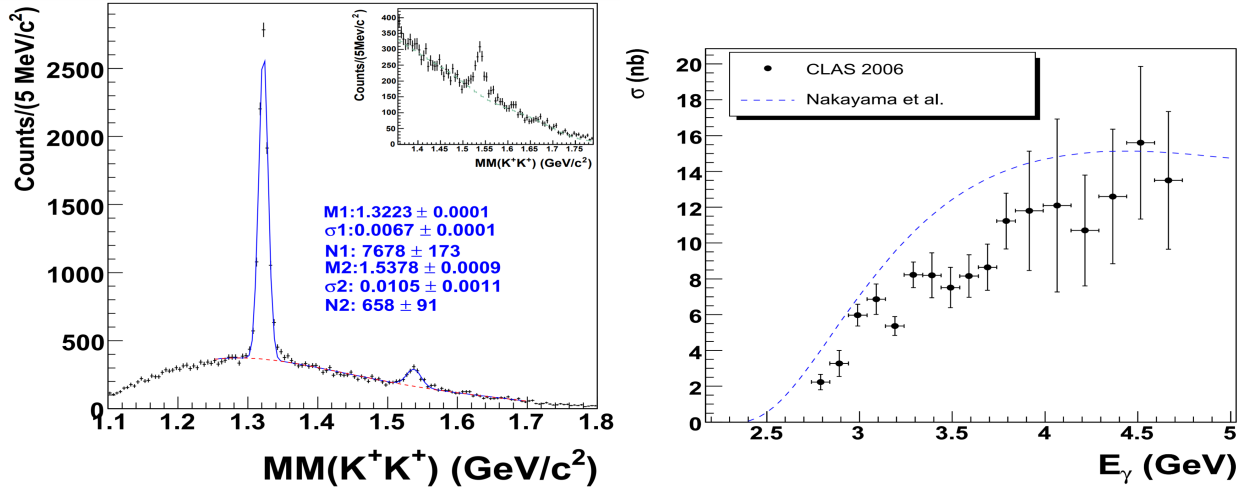


Figure 1.7: (left) Missing mass spectrum for $\gamma p \rightarrow K^+ K^+(X)$, which shows a clear signal for $\Xi^-(1320)$ and $\Xi^-(1530)$. (right) Total production cross section for $\gamma p \rightarrow K^+ K^+(X)$ for $\Xi^-(1320)$. Reproduced from [7].

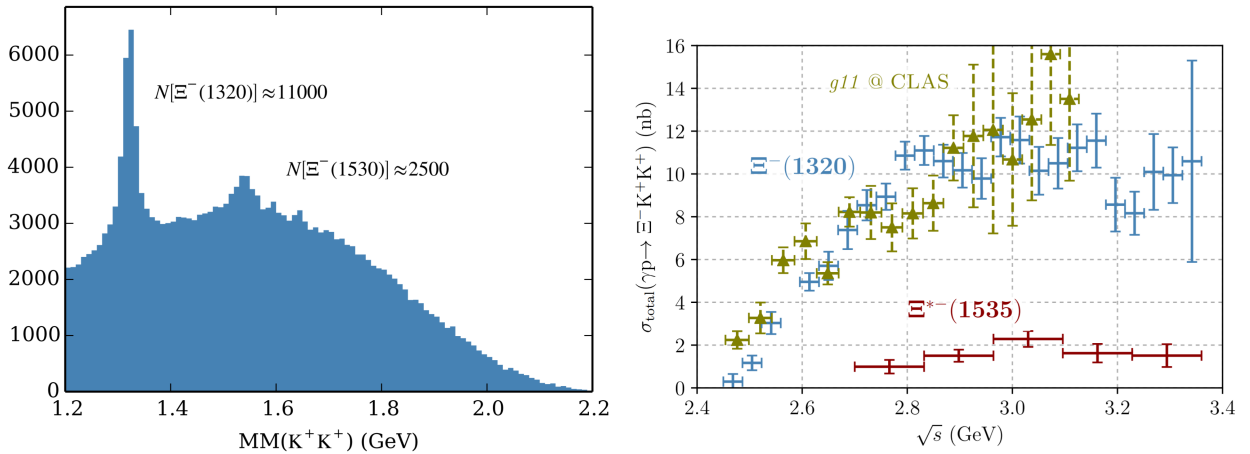


Figure 1.8: (left) Missing mass spectrum for $\gamma p \rightarrow K^+ K^+(X)$ for the CLAS g12 experiment (right) Total production cross section for CLAS g12 for $\gamma p \rightarrow K^+ K^+(X)$ for $\Xi^-(1320)$. Reprinted figures with permission from [8] Copyright 2018 by the American Physical Society.

CHAPTER 2

GLUEX COLLABORATION AT JEFFERSON LAB

GlueX is an hadron spectroscopy experiment based in Hall D at the US Department of Energy's Jefferson National Accelerator Facility (Jefferson Lab or JLab) in Newport News, Virginia. It was built as part of the 12 GeV upgrade of Jefferson Lab. The collaboration consists of approximately 150 members from 29 institutions across 9 countries [22]. Commissioning of the detector was completed in Spring 2016. Phase-I data taking took place over 3 run periods in Spring 2017, Spring 2018, and Fall 2018. It was recently complete with almost 300 billion physics events recorded. Phase-II data taking started in Spring 2020. This work will focus on the 3 data sets contributing to the total Phase-I data.

The two experiments at Jefferson Laboratory, CLAS and GlueX, are both spectroscopy experiments but were designed to prioritize different aspects. The CLAS detector consisted of six toroidal magnetic field coils, which resulted in charged particles to bend in arcs toward or away from the beam line. This prioritized momentum separation of the charged particles, which consequently resulted in limited acceptance. Therefore, it is advantageous for reactions to be studied inclusively in order to maximize statistics.

Alternatively, the primary goal of GlueX is to search for and map out the spectrum of exotic mesons. To be able to effectively map out the spectrum, the experiment needs to exclusively reconstruct a large variety of hadronic states with high efficiency and purity. GlueX is nearly hermetic with high efficiency for both charged and neutral particles. The main difference from the CLAS detector is the use of a solenoid to produce the magnetic field cause particles to travel helically within the GlueX detector. This results in higher uniform acceptance at the exchange of momentum separation. [23]

2.1 Continuous Electron Beam Accelerator Facility

The Continuous Electron Beam Accelerator Facility (CEBAF) is a 12 GeV electron accelerator at Jefferson Lab. It consists of two linear accelerators (linac(s)) and two recirculation arcs in order

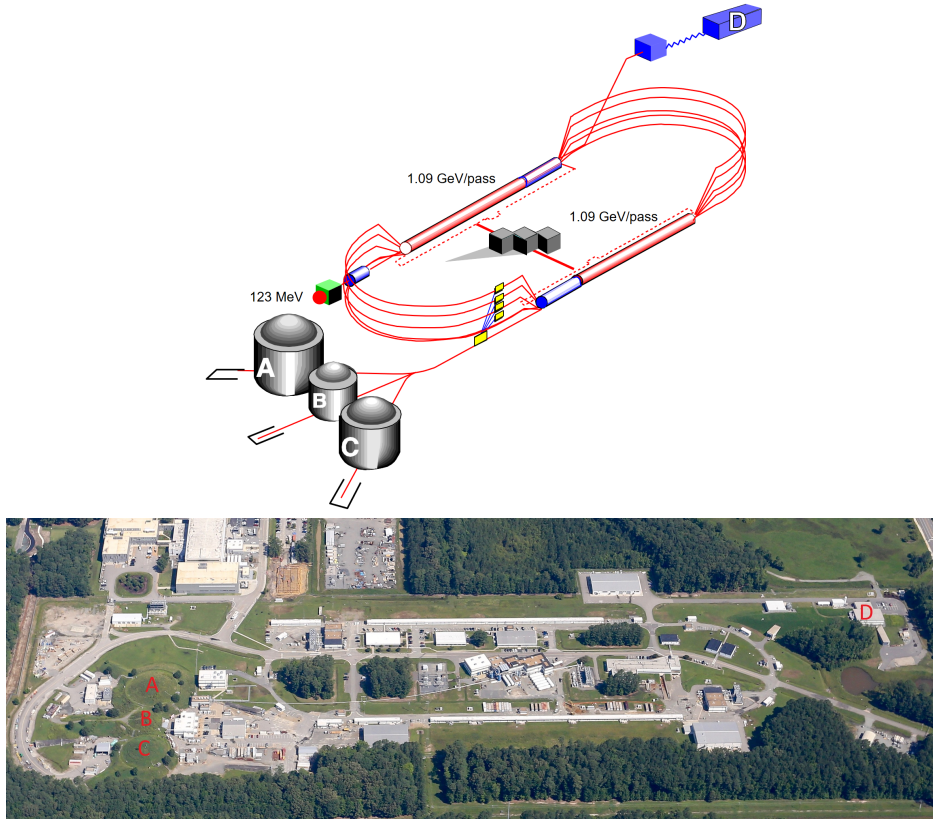


Figure 2.1: (Top) Schematic for the Continuous Electron Beam Accelerator Facility (CEBAF) at Jefferson Lab showing the 4 experimental halls. (Bottom) The aerial view of the accelerator with the individual experimental halls marked in red. Both are reproduced from [6]

to connect the linacs. The electrons start at the injector where they are inserted into the start of the north linear accelerator in four ns bunches. Each linear accelerator is primarily composed of 5 and 7-cell superconducting radiofrequency (RF) cavities stationed in cryomodules [24]. The superconducting RF cavities are used to accelerate the beam, achieving an acceleration of 1.09 GeV per passage through one of the linacs. At the end of each linac, there are a series of dipole magnets used to separate the RF bunches by energy as the magnetic field strength to curve the beam is dependent on the energy of the electrons. Each arc is composed of 5 individual beamlines for this purpose.

The connecting arcs are composed of dipole and quadrupole magnets. Dipole magnets steer the electron beam as it travels around the arc. The quadrupole magnets focus the beam in one

plane. Quadrupole magnets are arranged such that the magnets alternate between focusing and de-focusing to achieve an overall net focusing of the beam in both transverse planes. Prior to entering into the south linac, the electron beam encounters another RF separator, aptly named an RF combiner, to rejoin the individual beamlines back into one [24]. The electrons continue to travel around the accelerator up to 5 times for Halls A-C and up to 5.5 time for Hall D. This resulting design maximum energy for the halls is ~ 11 GeV for A-C and ~ 12 GeV for D.

Hall D houses the GlueX detector, seen in figure 2.1, and is located east of the end of the North linear accelerator. After 5.5 passes around the accelerator ring, the electrons are near the design energy of 12 GeV and are directed into Hall D.

2.2 The GlueX Beamline

As seen in figure 2.1, Hall D is located east of the end of the north linear accelerator. Hall D is comprised of 2 buildings, the tagger hall and the counting house. The beam initially travels to the tagger hall before traveling an additional 75m into the main spectrometer. The schematic of the beamline from accelerator to beam dump is shown in figure 2.2.

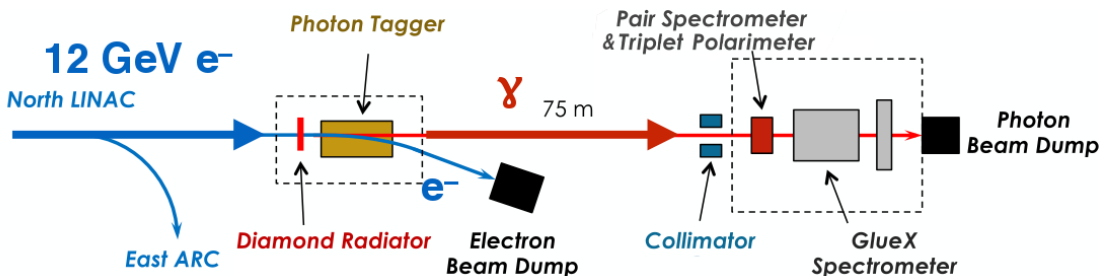


Figure 2.2: Schematic for the GlueX beamline. Reproduced from [?].

2.2.1 The Bremsstrahlung Technique and the Tagger Hall

Electrons that are up to 12 GeV in energy enter the tagger hall where they are incident on a thin diamond radiator in the case of polarized runs, or on an aluminum radiator in the case of amorphous runs. For polarized runs, the diamond radiator has 4 orientations that are considered. These orientations are 0° , 45° , 90° , and 135° with respect to their angle with the hall floor. Each set of orthogonal polarization orientations allow for measurements such as the beam asymmetry

and other polarization observables. The advantage of having two sets of orthogonal polarization directions is having a cross check for systematic studies.

Upon the electrons hitting the radiator, diamond or amorphous, the electrons undergo bremsstrahlung radiation producing a photon beam. The electron beam then pass through the tagging system consisting of a tagger hodoscope or a higher resolution tagger microscope in the energy region of the coherent peak. A dipole magnet is used to deflect the electrons into a beam dump and the Tagger 'tags' each photon as a specific energy as the electrons pass through an array of scintillators. Electrons that lost a small amount of energy due to bremsstrahlung in the radiator are deflected by a dipole magnet into the beam dump. Electrons that lost more than a quarter of their initial energy are directed to an array of scintillation counters [23]. This allows for the electrons energy to be determined and to allow one to determine the energy of the radiated photon via the difference of the electron energy.

The diamond radiator in particular is mounted onto a goniometer in the hall to allow for fine tuning of the angles at the which the diamond is oriented. The lattice of the diamond causes the resulting photon beam to be linearly polarized and coherent. The orientation of the diamond in the 4 orientations previously mentioned alter the direction of the linearly polarization. Fine tuning of the crystal plane adjusts the energy at which the coherent edge occurs as the position is a function of the angle between the beam and the normal to the crystalline plane of the diamond [23]. Nominal GlueX running results in a coherent edge in the photon beam spectrum to be located at ~ 9 GeV.

As the energy of the resulting photons increases, the trajectory occurs at a smaller polar angle from the beamline for the coherent portion of the photon beam. This is advantageous as it allows the lower energy photons to travel at larger angles which are easily blocked through the use of a collimator. The coherent portion of the beam spectrum at 12 GeV in energy has an emission angle of under $15 \mu\text{rad}$ while the incoherent portion spread is up to $43 \mu\text{rad}$ polar angle from the beamline [23]. The collimator is placed 75 m from the diamond radiator. The resulting nominal collimator aperture is thus 5 mm.

Triplet Polarimeter. After passing though the collimator, the photons approach the Triplet Polarimeter (TPOL) which is used to measure the degree of polarization of the photons. The polarization is measured via the process of triplet production. The TPOL has a thin Beryllium converter to trigger triplet photoproduction [25]. In triplet photoproduction, the photon interac-

tions with an electron in the converter, this electron then recoils from the Beryllium atom. The excess energy produces an electron-positron pair. The TPOL measures the recoil electron while the Pair Spectrometer (PS) measures the produced pair further down the beamline.

The degree of polarization is then calculated using the polarized cross section like that of a beam asymmetry measurement. When a photon beam has linear polarization, the production cross section σ gains a modification to the unpolarized cross section σ_0 , as in equation 2.1 where P_γ is the degree of polarization of the photon, Σ is the beam asymmetry, and ϕ is the azimuthal angle of the recoiled particle of interest.

$$\sigma = \sigma_0[1 - P_\gamma \Sigma \cos(2\phi)] \quad (2.1)$$

In the case of a beam asymmetry measurement, like those in [26, 27, 9], the degree of polarization is known and Σ is the value of interest. The opposite is the case here. The beam asymmetry can be calculated to first order in α from the QED tree-level diagrams allowing the degree of polarization to be fit [25].

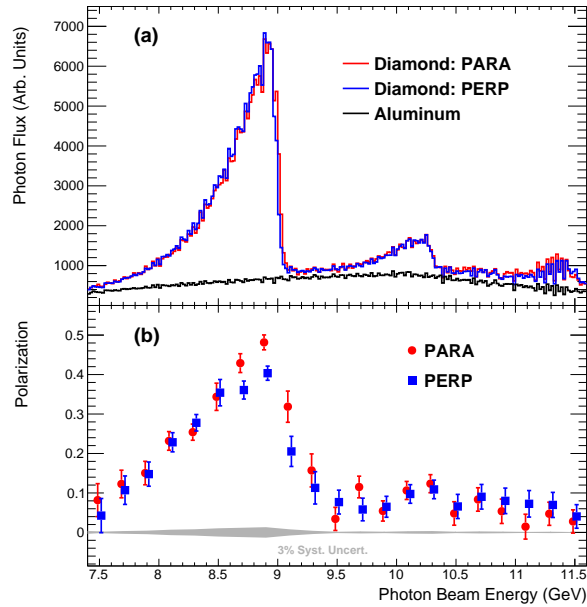


Figure 2.3: An example of the flux determined by the PS and the degree of polarization obtained from the TPOL. Reproduced from [9]

Pair Spectrometer. The pair spectrometer (PS), shown in figure 2.4 is used primarily to determine the beam flux within the coherent peak. The PS reconstructs the energy of a beam photon



Figure 2.4: An image of the pair spectrometer in the hall. The beam travels from left to right across the image.

by detecting the electron-positron pair produced by the photon in the TPOL. The determination of the photon beam flux may be used to calibrate the energy determined by the tagging system. The detectors cover a momentum range for the electrons and positrons that corresponds to photon energies between 6 and 12.4 GeV/ c [28]. An example of the resulting flux from the PS and the degree of polarization from the TPOL for the 2016 commissioning run period is shown in figure 2.6.

2.3 The GlueX Spectrometer

Shortly after the PS, the photon beam reaches the main detector setup, which consists of a start counter, solenoid magnet, two drift chambers, two calorimeters, and a time-of-flight spectrometer. The solenoid is a 2 T superconducting solenoid which produces the necessary field required for the desired hermiticity, as well as momentum and energy resolutions needed for tracking particles. It helps to reduce electromagnetic background due to its geometry by causing low energy electron-positron pairs to spiral near the beamline. The solenoid magnet houses the target, start counter, barrel calorimeter, and the central and forward drift chambers. The solenoid stands almost 4 m high and 4 m long [23].

2.3.1 Target and Start Counter

Target. The target cell is located within the solenoid and is filled with liquid hydrogen. The target is filled by condensing the hydrogen and cooling to an operating temperature of 20.1 K

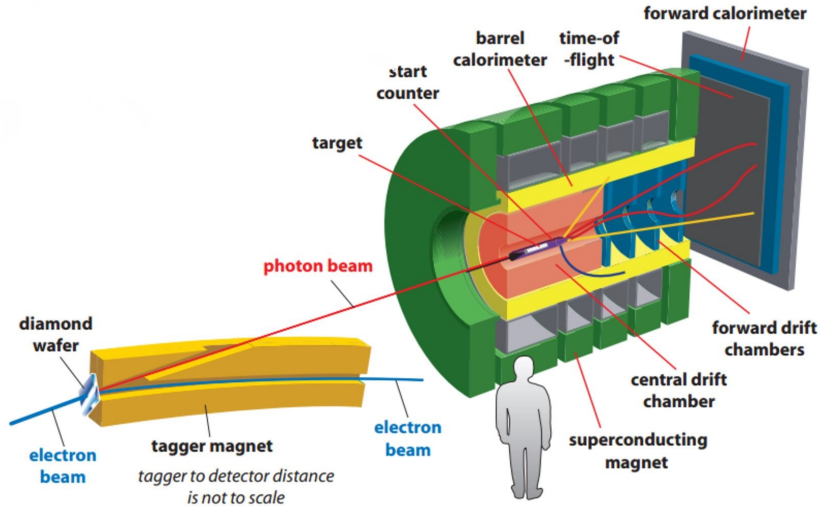


Figure 2.5: Schematic of the overall GlueX detector located in Hall D at Jefferson Lab. Reproduced from [10].

which reduces boiling within the target cell [23]. The density of which is approximately stable at $71.2 \pm 0.3 \text{ mg/cm}^3$ [23]. The target is located at 50 cm in z , where 0 is defined at the start of the solenoid, and is 30 cm long.

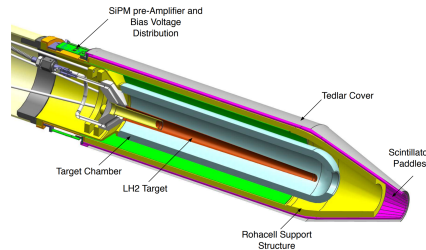


Figure 2.6: Schematic of the start counter detector and the target cell. Reproduced from [11].

Start Counter. The start counter (SC) is located immediately outside of the target cell. The primary purpose of this detector is to accurately associate the beam photons with the correct RF bunch. It has a cylindrical shape with a cone-shaped nose consisting of 30 narrow scintillator paddles [11]. The segmentation allows for operation up to a beam intensity of $10^8 \text{ } \gamma/\text{s}$. Beam bunches enter the target every 4 ns and thus the resolution of the SC must be sufficiently high to

accurately identify the corresponding bunch for each event. The start counter is integral in the design of the detector system.

2.3.2 Drift Chambers

The drift chambers are responsible for the tracking of charged particles, in which they provide position, timing, and energy deposition information. Both of the drift chambers are filled with their own mixture of argon and carbon dioxide which is monitored by shift personnel during periods of running. Charged particles passing through a drift chamber ionize the gas. The induced current is then measured by the electronics. The gas mixtures are optimized for position resolution in either detector.

Central Drift Chamber. The central drift chamber (CDC) is of cylindrical straw-tube design located in the upstream half of the solenoid and is the first layer around the target and start counter. It is composed of 28 layers of 1.5 m long, 1.6 cm diameter straws; a total of 3522 straws make up this detector [29]. Each straw contains an anode wire made from 20 μm diameter gold-plated tungsten [29]. The inner wall of each straw acts as a cathode to ensure uniformity in the electric field around the wire. The straw is used to add rigidity, support the tension in the wire, and prevent the wires from touching. The alignment of these straws is a major calibration effort that is taken every run period as seen in [29].

The motion of the charged particles in the magnetic field as well as the timing allow one to determine the momentum of the particle. The CDC provides the information needed to make timing cuts and cuts based on the amount of energy deposited while traveling through the detector. As shown in 3.2, the proton is clearly distinguishable from the mesons and leptons by energy deposition below 1 GeV in the CDC. The CDC provides polar angular coverage from 6° to 168° from the beamline.

As discussed briefly in section ??, the CDC experienced a degradation in the gas mixture during the Spring 2018 run period resulting in a loss in efficiency for this work.

Forward Drift Chamber. The forward drift chamber (FDC) is located in the downstream half of the solenoid and is used to track charged particles along the beam line. The FDC has a polar angular coverage from 1° to 10° from the beamline. The FDC handles a high volume of tracks as well as spiraling trajectories due to the nearness to the electromagnetic background surrounding

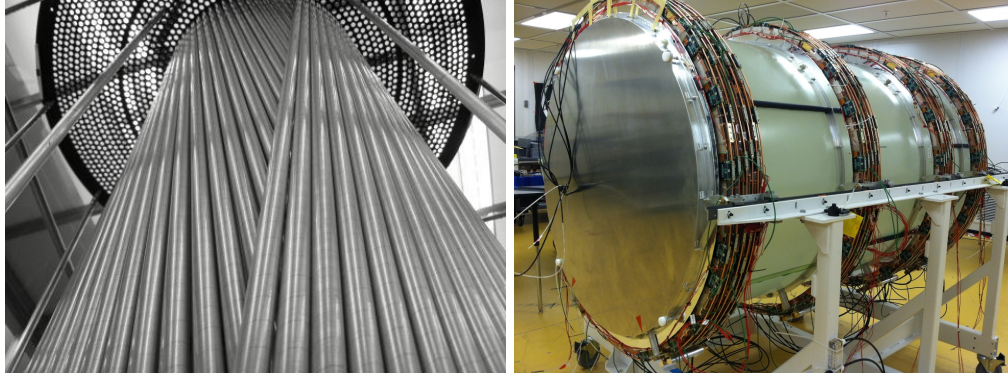


Figure 2.7: Image of the central drift chamber (left) and forward drift chamber (right).
Reproduced from [12].

the beamline. It is composed of Cathode Strip Chambers, which consist of two cathode planes divided into strips and placed at an angle with respect to wire planes [30]. The FDC consists of 4 identical disk shaped packages, each with 6 cells. A cell consists of two cathode strip planes with anode and field-shaping wires in between. Spatial and direction information is determined from the charge induced on the strips and timing information from the wires.

2.3.3 Calorimetry

The two calorimeters are used to detect neutral particles. Both measure the energies and positions of the showers from the photons or neutrons. Additionally, both of the calorimeters measure the timing of the hits for both neutral and charged particles.

Barrel Calorimeter. The barrel calorimeter (BCAL) is located just inside the solenoid and covers a range in polar angle of 11° to 126° from the beamline [31]. The BCAL determines the position and energies of photon- or neutron-induced electromagnetic showers as well as the flight time of all particles. The BCAL consists of 48 modules of scintillating fibers with trapezoidal cross section, forming a 3.9 m long cylinder that fills the solenoid [31]. Each module consists of approximately 15,000 fibers and sandwiched within 185 layers of 0.5 mm thick lead [23]. The BCAL, as later discussed in section 3.2, is the detector with the highest timing priority in determining a charged particles hypothesis.

Forward Calorimeter. The forward calorimeter (FCAL) is a lead-glass calorimeter located downstream of the main solenoid. It covers a polar angular region of 1° to 11° from the beamline

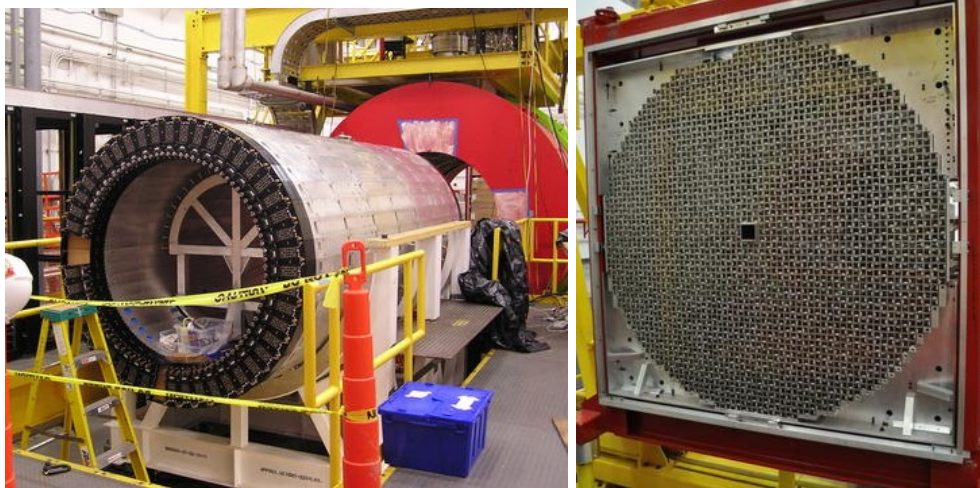


Figure 2.8: Image of the barrel calorimeter prior to it being placed into the solenoid (left) and forward calorimeter without the front cover to show the crystals (right). Reproduced from [12].

[23]. It consists of 2,800 4 cm square lead-glass modules, each containing a lead-glass block and a photomultiplier tube (PMT), arranged in a circular array [32]. The detector is located within its own dark room. As an electromagnetic shower enters the detector, Cherenkov light is produced. The light is then measured by a PMT and the amount detected is directly proportional to the energy deposited.

2.3.4 The Time-of-Flight Spectrometer

The time of flight spectrometer (TOF) is a planar detector located directly upstream of the of the FCAL and is used to determine flight time of charged particles. It is composed of two planes of scintillator paddles with PMTs on both ends of each paddle. Each plane consists of 38 full-length (252 cm) full-width (6 cm) paddles, 4 full-length half-width paddles, and 4 half-length full-width paddles along the beamline [10]. The half-width and half-length paddles are situated around the beamline, in order to lower the rates due to electromagnetic background, especially at high beam intensities. The TOF reads the time at which charged particles pass through it with a design accuracy up to 80 ps. In conjunction with the time from the accelerator (RF time) and its momentum, a particles flight time and path-length traveled are determined. The detector is accurate to sufficiently distinguish between charged pions and kaons up to 2.5 GeV/ c in momentum.

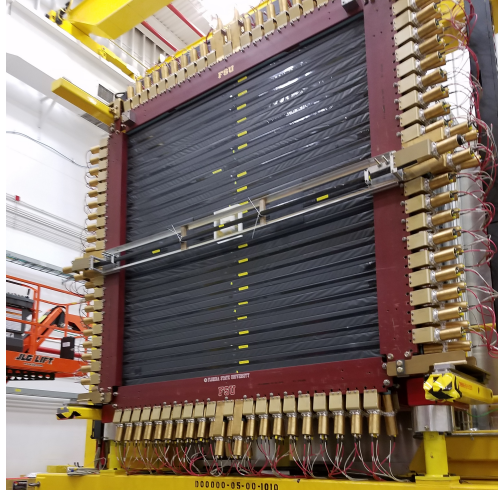


Figure 2.9: Image of the time of flight spectrometer in the hall prior to the upgrade but with the inclusion of the Lucite shielding.

The TOF additionally has a Lucite shield around the beam hole to help lower the interaction rates. This shielding was installed in December of 2015. The implementation of this structure in the detector simulation geometry is later discussed in section 2.3.4.

In the summer and fall of 2019, the TOF was upgraded to further reduce interaction rates in the central paddles. This is in anticipation of Phase-II running which will include higher beam intensities and began in Spring 2020. This upgrade increased the size of the beam hole from a 12 cm square to an 18 cm square. It also increased the segmentation of the paddles surrounding the beamline. The 4 half-length paddles per plane were increased to 8 half-length paddles per plane. Their widths were also decreased from 6 cm to 4.5 cm. The 4 half-width paddles remained immediately after the half-length paddles. The upgrade included the addition of 4 full-length 3/4-width paddles surrounding the half-width paddles before returning to the nominal full-length full-width paddles. Further discussion about implementing this new geometry into the simulation geometry can be found below in section 2.3.4.

Simulation Geometry Updates. As part of this work, a year was spent on-site at Jefferson Lab. The Time-of-Flight specific work performed while stationed at the lab includes the calibration of the Fall 2018 run period and two simulation geometry updates. These detector geometry updates are integral in producing Monte Carlo that is an accurate representation of data. The update

described in section 2.3.4 was also the primary step in validating the corresponding software update for the new geometry.

Geometry Update: Inclusion of Lucite Shielding. In December of 2015, a shield was added to the front of the Time-of-Flight spectrometer as shown in Figure 2.9. This addition was in order to reduce the high rates caused by increased beam intensities as consequently increased electromagnetic background around the beam hole. The shielding consisted of a face of 6 layers of Lucite added around the beam hole in the front of the Time-of-Flight spectrometer. These layers were held in place by an inner section of polyethylene that went through the two planes of the detector and continued out the back of the detector. Measurements were taken in the hall in November of 2018. The face of the shield is 25 cm by 25 cm and 5.7 cm thick. The polyethylene inner section is 13.3 cm long with an inner square hole with a side length of 9.5 cm.

The implementation of this shielding into the detector geometry required the addition of four new volumes, one for the face and three for the support structure. The support structure consists of the portion within the face, the portion within the planes of the Time-of-Flight, and the portion behind the detector. Figure 2.10 shows the cross section of the detector geometry before and after the implementation of the shielding.

Geometry Update: Detector Upgrade. During the summer and fall of 2019, the Time-of-Flight spectrometer underwent an extensive upgrade to increase the segmentation of the inner paddles to accommodate increasing beam intensity rates. This work contributed to that upgrade by placing the new geometry into the detector specification software package that is used by Geant4 [33] to simulate the detector. This new detector geometry was then used to test the upgrade to the reconstruction software prior to running with the new geometry.

The upgrade included increasing the size of the beam hole as well as increasing the segmentation near the center of the Time-of-Flight spectrometer. This involved adding two additional volumes to the geometry and modifying the remaining five volumes. The beam hole changes from a 12 cm square to an 18 cm square. Consequently, the central single-sided paddles decreased in length from 120 cm to 117 cm. These paddles also decreased in width from 6 cm to 4.5 cm and the number of them per side doubled. The half-width paddles (3 cm) stayed the same on either side of the single-sided paddles. Prior to the upgrade, the following paddles were the nominal 6 cm double-sided paddles. The upgrade included an additional 2 paddles on



Figure 2.10: The cross section of the Time-of-Flight spectrometer before and after the implementation of the Lucite shielding.

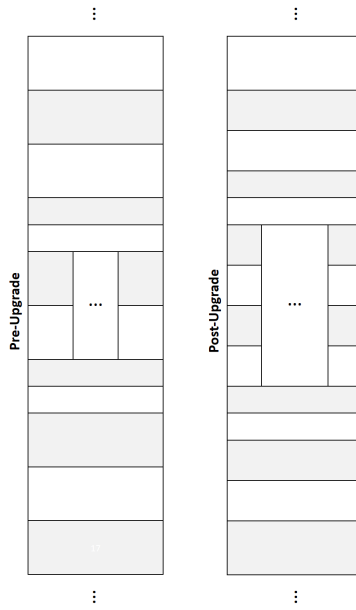


Figure 2.11: A diagram of the Time-of-Flight spectrometer demonstrating the increased segmentation and beam hole size.

each side of the half-width paddles which are 4.5 cm in width. These changes have been tested and implemented as the nominal geometry for the Spring 2020 run period and onwards.

2.3.5 Detection of Internally Reflected Cherenkov Detector

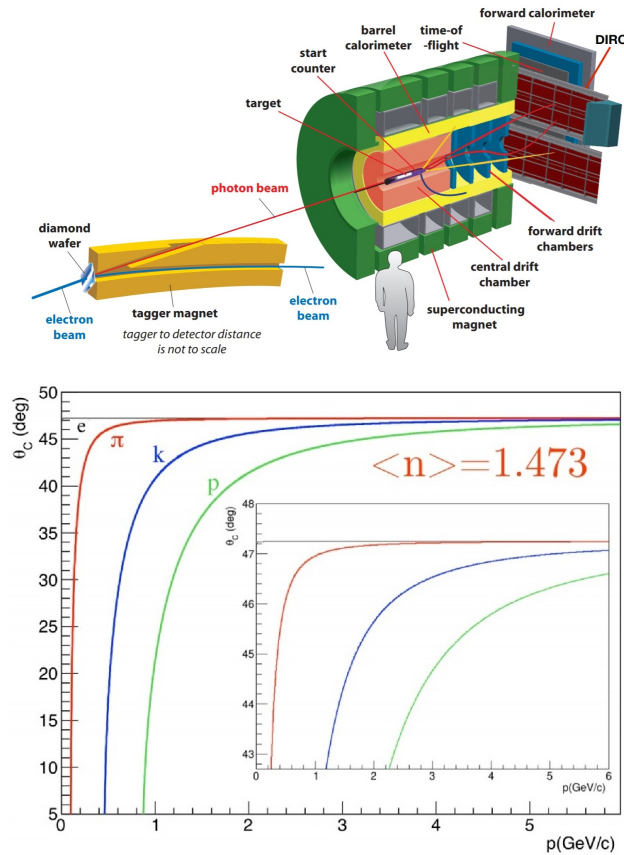


Figure 2.12: A schematic for the placement of the DIRC within the GlueX detector. [13]

The Detection of Internally Reflected Cherenkov (DIRC) detector will increase the number of topologies that are able to be studied, as well as reduce the background due to misidentification of particles. The DIRC will extend the momentum region in which kaons and pions can be distinguished to 4 GeV/c [13]. Installation of the DIRC took place in 2018, with commissioning occurring in early 2019. It is located between the TOF and the solenoid. The DIRC consists of 4 boxes, each containing 12 synthetic fused silica bars [13]. When a charged particle hits the DIRC, Cherenkov light is emitted at an angle known the Cherenkov angle. The cosine of this angle is

inversely proportional to the velocity of the particle and is greater than the critical angle for total internal reflection in the momentum range of interest. The quartz bars are used as radiators and light guides for the Cherenkov light and the Cherenkov angle is preserved through the lights path. The particles can be distinguished by their Cherenkov angle at a given momentum as seen in figure 2.12. This detector will play a large role in kaon identification in Phase-II GlueX, which started running in the spring of 2020.

CHAPTER 3

DATA SETS AND ANALYSIS FRAMEWORK

From the detectors, the raw data are collected and calibrated. This data is then constructed into tracks and showers and stored in the format of Reconstructed Event Storage (REST) files. At this stage, all hit level information is discarded. The process of going from raw data to REST data is computationally expensive and is only performed a limited number of times at the collaboration level, usually after substantial improvements to detector calibration. The REST data are saved to be later used to skim over for specific reactions in so-called 'analysis launches'. It is at that stage that particle classification is performed.

3.1 Data Sets

This analysis is based on Phase-I running of GlueX which consists of the three major run periods taken over 2 years. After successful commissioning in Spring 2016, the first physics data taking was in Spring 2017. It occurred from January 2017 to March 2017 and resulted in ~ 50 billion physics events or ~ 0.8 Pb of data. The next major run period was in Spring 2018 occurring from December 2017 to May 2018. Spring 2018 resulted in ~ 145 billion physics events or ~ 1.9 Pb of data, a substantial increase from Spring 2017 and the largest portion of the Phase-I data. The latest data set of Phase-I was the Fall 2018 run period from September 2018 to November 2018, resulting in ~ 78 billion physics events or about 1.1 Pb of data. This run period also included 4.5 days of running with the coherent edge at a lower energy and the Pair Spectrometer moved to a lower operating beam energy range, which allows for measurements directly comparable to previously measured quantities, primarily from the CLAS collaboration.

3.2 Analysis Framework

After the data have been reconstructed from detector hits to tracks and showers, an analysis launch for a particular reaction is performed. These skims include primary loose particle selection criteria to allow for a subset of the data to be considered for further study. The event selection is

performed by building all possible combinations for the desired reaction with at least the minimum number of required charged tracks. All detected tracks and showers are candidates for particles of the charge of interest. The combinations are then subjected to various selection criteria to eliminate hypotheses that are not consistent with the reaction of interest. The charge of a particle is determined by the movement in the magnetic field. This charge then allows for the hypotheses of nucleon, kaon, pion, and lepton. The fractional velocity β for these candidates is calculated using the path length and timing. This value clearly shows bands for each of the different particle hypotheses, as shown in figures 3.2. At low momentum, there is a clear separation of the different particle candidates. As momentum increases, each of the bands approach 1 or the speed of light. The additional horizontal bands are due to hypotheses associated with an incorrect beam bunch.

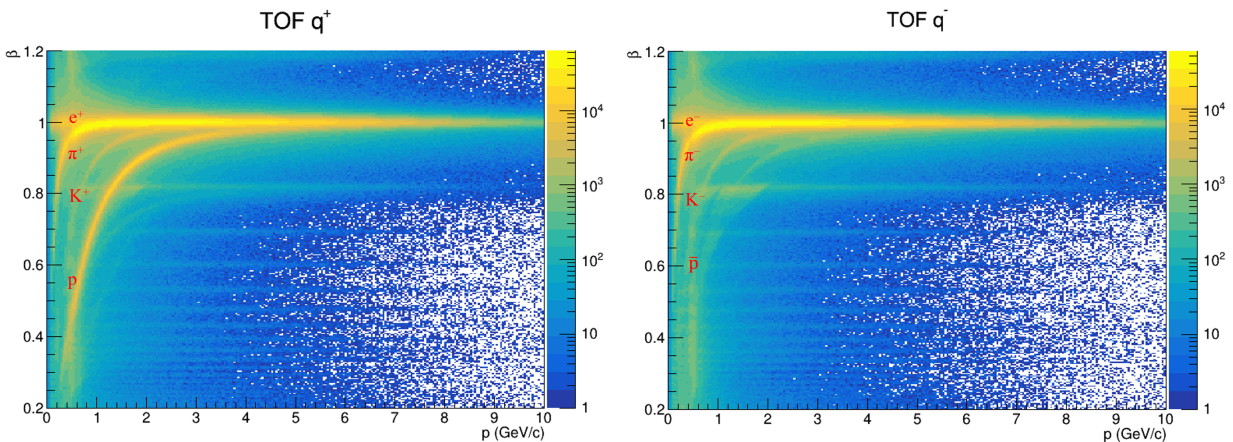


Figure 3.1: Example of a β plots for the Time-of-Flight spectrometer for positively charged candidates and negatively charged candidates. Taken from the monitoring histograms produced for run 51582 of the Fall 2018 run period

Additionally, for each particle hypothesis, a difference in timing is calculated. This difference is between the back propagated timing from the detector to the track vertex and the forward propagated time from the accelerator. Since the mass is assumed in the propagation from the detector, these distributions should be centered at zero ns for correct hypotheses. The difference between these times is used to determine the validity of the hypothesis. If it is inconsistent within a given range, depending on the analysis, the hypothesis is discarded from consideration. By using this method for each of the combination of hypotheses, a subset of data is considered for further

analysis. An example of the difference in timing versus momentum distributions for candidates of a K^+ in the Time-of-Flight spectrometer is shown in figure 3.2. The correct hypotheses are contained in the band at zero ns. The upper and lower bands are that of the protons and pions, respectively. The bands that do not asymptotically approach zero ns contain those whose candidates are associated with the incorrect beam bunch resulting in a shift by a factor of 4 ns, as discussed in section 3.2.1. It can be seen that with the TOF, pions and kaons are separable up to approximately 2 Gev in momentum. In practice, each track is only considered in the best detector with the best timing information available. The hierarchy for the detectors with the best timing information is BCAL>TOF>FCAL>SC. The timing is considered in this order due to the individual detector resolutions. The BCAL and TOF also cover different angular regions so the order between the first two is arbitrary. The timing requirements applied at the time of the analysis launch for the relevant particles are found in table 3.2.

Table 3.1: The timing requirements for each relevant particle hypothesis in the 4 detectors with timing information [3].

Hypothesis	BCAL (ns)	TOF (ns)	FCAL (ns)	SC (ns)
π^\pm	± 1.0	± 0.5	± 2.0	± 2.5
K^\pm	± 0.75	± 0.3	± 2.5	± 2.5
p	± 1.0	± 0.6	± 2.0	± 2.5

As charged particles travel through a medium, the particles interact with the electrons in the medium which results in ionization loss. Energy loss by ionization can be found using the Bethe formula, equation 3.1, which shows that the loss is inversely proportional to β squared [1]. In equation 3.1, the medium is expressed by the density ρ , atomic mass A , and atomic number Z through which the particle of charge q is traveling at velocity β [1]. The coefficient K is approximately $0.307 \text{ MeVg}^{-1}\text{cm}^2$ derived from fundamental values, W_{max} is the maximum energy transfer to an electron in a single collision, and I is the excitation energy of the medium [1].

$$-\langle \frac{dE}{dx} \rangle = \frac{Kq^2Z\rho}{A\beta^2} \left[\frac{1}{2} \ln \frac{2m_e c^2 \beta^2 \gamma^2 W_{max}}{I^2} - \beta^2 - \frac{\delta(\beta\gamma)}{2} \right] \quad (3.1)$$

The Bethe formula depends on the fractional velocity. If one looks at the ionization loss as a function of momentum, bands form for particles with different mass. In GlueX, the resolution is such that this value can be used to separate the proton from the lower mass particles using the

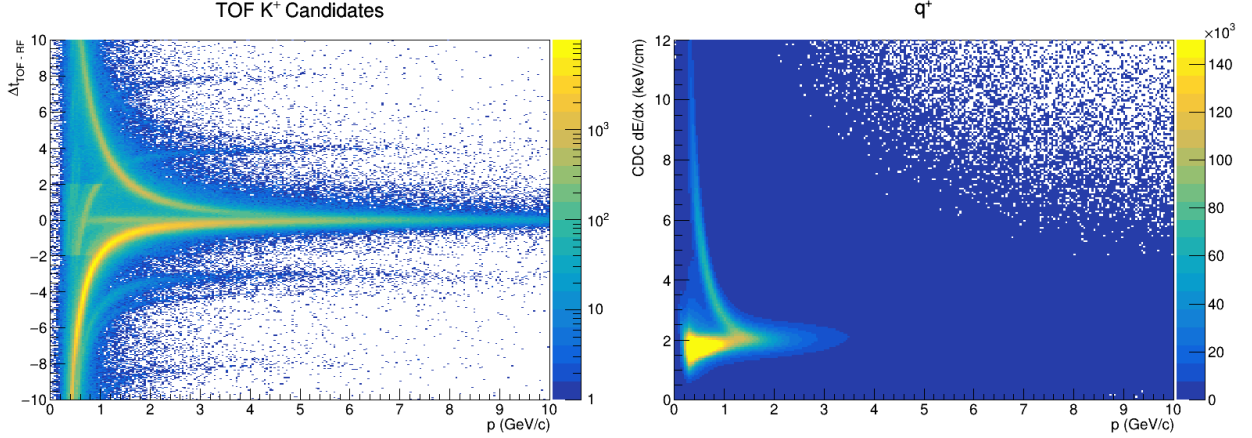


Figure 3.2: (left) Example of a Δt plot for the Time-of-Flight spectrometer for K^+ candidates and (right) of the energy deposition in the Central Drift Chamber. Both plots were taken from the monitoring histograms produced for run 51582 of the Fall 2018 run period.

Central Drift Chamber (CDC). An example of which is shown in figure 3.2. The large deposition at low momentum is that of the proton while the other particles are indistinguishable. This difference is apparent up to about 1 GeV in momentum. In the CDC, classifications are used to selection those hypotheses within the region of separation and retain all the candidates outside of that region. For protons or anti-protons, the energy deposition per unit length needs to be greater than [3]:

$$dE/dx > e^{-4p+2.25} + 1.0 \quad (3.2)$$

Meanwhile, all the mesons must be less than [3]:

$$dE/dx < e^{-7p+3.0} + 6.2 \quad (3.3)$$

Kaons are typically much less abundant than pions as shown by the relative intensities in figure 3.2. Therefore, channels containing kaons have additional constraints in order to have a more reasonable output file size. This additional constraints include the requirement that there is timing in at least one of the four timing detectors (BCAL/TOF/FCAL/SC) and that there is enough information to calculate dE/dx in the CDC. Other particles, such as pions and protons, are not required to satisfy both of these constraints.

Loose mass constraints may also be applied for decaying particles such as the mass of π^0 from the detection of two photons. These in general are sufficiently loose to not have a large effect on the requested channel. For example, the ground state $\Xi(1320)$ has a requirement that the invariant mass is between 1.1 GeV and 1.5 GeV [3]. Additionally, the Λ has the requirement to be within 1.0 GeV and 1.2 GeV [3].

3.2.1 Tagger Accidentals

Figure 3.2.1 shows an example of the beam bunch distribution for the Spring 2017 data set. This quantity is the difference in timing between the time measured in the tagger and the propagated RF time in the main spectrometer. The central peak is known as the prompt peak and represents the correct choice in RF bunch associated with the beam photon. The side peaks are known as out-of-time beam photons which show a four ns pattern matching that of the four ns timing between electron bunches. So called 'accidentals' are photons within the prompt peak that are incorrectly associated. Naively, the four ns structure continues underneath the prompt peak at the same scale as it occurs in the side peaks. The accidental beam photons can be caused by a variety of events including incorrect identification of the beam photon or hits in nearby counter at the same time as a correct photon.

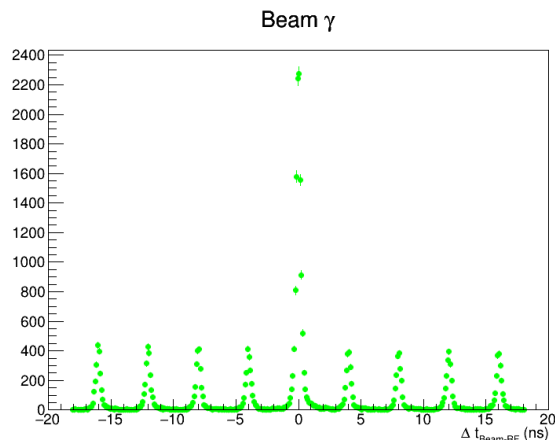


Figure 3.3: Example of the beam bunch distribution for the Spring 2017 data set.

All plots shown in this work are 'accidental subtracted.' This is a correction for the photons that have the same structure as the side peaks that are underneath the prompt peak. The correction

is performed by only considering events within the prompt peak and then subtracting the average number of events within the first peak on either side of the central peak.

Recently, collaborators discovered that the naive approach of the accidentals having the same structure as the side peaks is too simplistic of an assumption. In order for the side peaks to be used to approximate the prompt peak distribution, they need to be scaled by a small percentage of $\sim 5\%$ to accurately represent the background under the prompt peak. The value represents a systematic uncertainty in the incoming photon flux which becomes negligible with the inclusion of the scale factor. This small factor is dependent on the run number and run period as it was not constant. This likely stems from variations in the accelerator, such as but not limited to, effects in transmissions due to running multiple experiments concurrently. This factor is implemented by weighting the events in the side peaks prior to the subtraction of the average. All plots here forth include accidental subtraction with the use of the additional scaling factor.

3.2.2 Kinematic Fitting

One of the major tools used in spectroscopy is the use of kinematic fitting, which consists of applying a set constraints to a hypothesis. Kinematic fitting is the act of varying the measurements within their uncertainties such that the measurements are consistent with the external constraints on the system. The most basic of this is the requirement of energy and momentum conservation. The position and momentum measurements of each particle in the final state are adjusted to force the exact conservation of the both energy and momentum for the reaction. The resultant pulls, or the change divided by change, in uncertainties should result in a Gaussian distribution. If the changes are purely statistical, the Gaussian should be centered at zero difference. Additionally, if the uncertainties are correctly understood, the Gaussian should have a width of one, assuming no cross correlations between the measurements.

There are four fit types available in the GlueX analysis framework. The available requirements can be on the momentum 4-vectors and the vertices. The four options include: no fit, each of the individual options, and the combinations of momentum 4-vectors with vertex constraints. All fits requiring 4-momentum conservation also include the constraint on the mass of decaying particles unless otherwise requested to not be constrained. In general, the main fit used for analyses within GlueX is that which constrains the 4-momentum and the vertex positions.

Conservation of 4-momentum is straight forward with four equations, one for each quantity with zero unknowns for an exclusive reaction. For an inclusive reaction where one particle is missing from the reaction, the only difference is that the three components of the missing particle's momentum are unknown as well. In general, each additional mass constraint provides an additional equation with no extra unknowns. The vertex constraint requires that the set of particles all have tracks that intersect at the same point in space. This constraint results in two independent equations per particle at the vertex. The equations correspond to the bend plane of the tracks in magnetic field and in the non-bend plane [34, 35]. The location of the vertex contributes three unknowns. For example, if one considers the decay of a particle into two decay particles ($A \rightarrow BC$), there are four equations, two associated with both B and C , and three unknowns associated with the three components of the vertex position. The vertex constraint is particularly useful for channels in which a particle decays weakly. Weak decays occur on a time scale of the weak interaction (10^{-11} s) as opposed to the time scale of the strong interaction (10^{-23} s) [36]. The drastic change in the time scale results in a detectable distance traveled prior to decaying. The addition of the vertex constraint will thus have two vertices to constrain, the production vertex and the vertex of the weakly decaying particle.

As with any fit, a figure of merit is provided for each event that converges. In GlueX, the two figures used are the confidence level as well as the χ^2 for the fit. The χ^2 is typically more stable to use in terms of the uncertainties due to tracking within the detector. The χ^2 is typically normalized to the Number of Degrees of Freedom (NDF) within the fit, and will be referred to as χ^2/NDF for the rest of this work. Once normalized to the NDF, the idealized value from the fit is one. Events with a χ^2/NDF less than one are typically associated with statistical fluctuations within the fit. Events where the χ^2/NDF is much greater than one are a result of being inconsistent with the fit requirements. These events are removed from further analysis by selecting a maximum χ^2/NDF to consider.

CHAPTER 4

GROUND STATE CASCADE BARYONS $\Xi^-(1320)$ AT GLUEX

Cascade resonances are predicted to be produced through t -channel photoproduction of hyperon resonances [21]. The difficulty of studying Cascade baryons using photoproduction stems from the large amount of energy needed to produce strange quarks. For each strange quark in the final state, a kaon containing an anti-strange quark must be produced with rest mass of ~ 500 MeV. Therefore, in Ξ photoproduction, 1 GeV of energy is lost solely to the production of the kaons in the system. The increase in the energy of CEBAF to 12 GeV provides the necessary energy to produce high-mass Cascade baryons.

The diagrams in figure 4.1 show the current models used to describe the production of negatively-charged and neutral Cascade baryons. Through t -channel production, a kaon and an excited, singly-strange hyperon are produced [21]. This excited intermediate hyperon then decays into an additional kaon and a Cascade baryon. The kaon produced through the t -channel mechanism is predicted to be very forwarding-going and to have high momentum. This allows for the two kaons to be separated via their polar angle, the angle between the beam line and their trajectory. Figure 4.2 shows the simulations of the momentum vs polar angle distribution done for both the octet ground state $\Xi^-(1320)$ and an excited state $\Xi^-(1820)$ [14]. The three high intensity regions consist of kaons, kaons and protons, and pions from highest momentum to lowest. The red box indicates the region in which the TOF spectrometer was designed to be able to easily identify kaons from pions via momentum separation.

The baseline GlueX detector can only separate the kaons and pions up to a momentum of 2.5 GeV/ c and therefore, is not capable of directly identifying the high momentum t -channel produced kaon from a pion with the current separation, as its momentum is ~ 6 GeV for the ground state Cascade baryon. This kaon lowers in momentum as higher mass Cascade baryons excited states are considered. Even with the DIRC addition, it is unrealistic to expect a direct identification of this kaon for the ground state Ξ . Instead, the reaction is considered as whole for both the ground

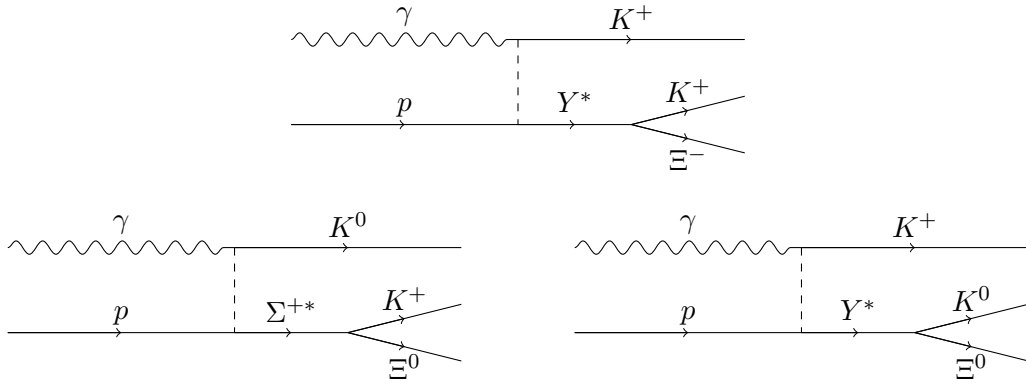


Figure 4.1: Feynman diagrams for photoproduction of the octet ground state Ξ baryons. The top diagram is for a negatively-charged $\Xi(1320)$ while the bottom diagrams are the two production mechanisms for $\Xi^0(1320)$.

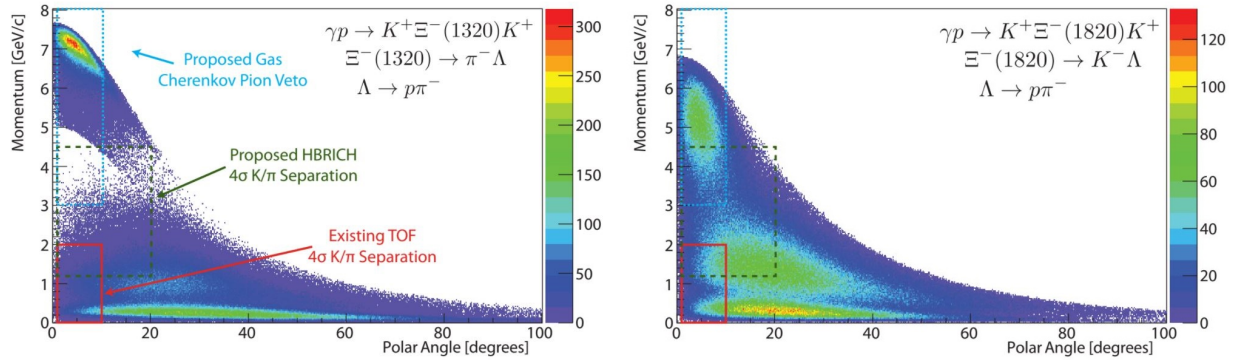
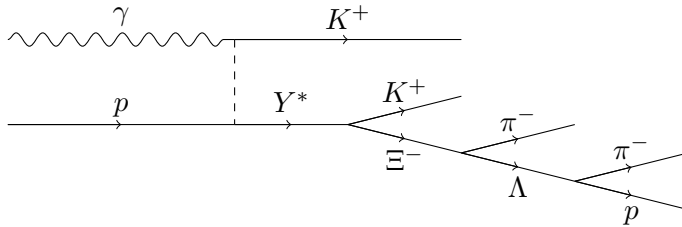


Figure 4.2: Simulations for momentum vs polar angular for all tracks where the red box denotes the kaon-pion separation currently possible in the TOF. The three high intensity regions consist of kaons, kaons and protons, and pions from highest momentum to lowest. Reproduced from [14].

state and excited Cascade baryons through the use of the kinematic fit as shown in section 4.1. The primary source of background in these reactions will be the misidentification of the high momentum kaons as pions. The DIRC addition will extend kaon identification to higher momentum, an aspect that will greatly enhance the likelihood of positively identifying the Cascade spectrum, especially the excited states.



The ground state negatively-charged Cascade baryons $\Xi^-(1320)$ are detected via an exclusive decay chain. The decays of $\Xi^- \rightarrow \Lambda\pi^-$, and $\Lambda \rightarrow p\pi^-$ are considered, resulting in a final state of $K^+K^+p\pi^-\pi^-$. These decays have branching ratios of 99.9% for the Ξ and 64% for the Λ [1]. The neutron decay of $\Lambda \rightarrow n\pi^0$ can also be considered but is not in the scope of this work. The neutron decay is much more challenging due to lower statistics because of the branching ratio as well as the difficulty of detecting neutrons. This analysis uses the three different run periods (Spring 2017, Spring 2018, and Fall 2018) from GlueX Phase-I data taking. The skimmed data file produced during the analysis launches for each run period used the reaction 1_14_11_11_23 (representing $\gamma p \rightarrow K^+K^+\Xi^-$) with tags *B4_M23*. These tags represent the inclusion of four accidental beam bunches on either side of the prompt peak as discussed in section ???. The Spring 2017 data set utilizes the third iteration of the reconstruction of the data and was produced in analysis launch version 20. The Spring 2018 data set uses the second iteration of the reconstruction and was produced using the same reaction filter in analysis launch version 3. Similarly, the Fall 2018 uses the second iteration of the reconstruction of the data from analysis launch version two. The standard GlueX analysis cuts apply to all sets of this reaction.

4.1 Event Selection: Kinematic Fitting

Kinematic fitting is the most important tool in this analysis and believed to be the main advantage of studying exclusive reactions. The form of kinematic fitting used in this analysis results in the requirement for 4-momentum conservation, Λ mass constraint, and vertex constraints. The latter requires that particle tracks originate from the same vertex. For the $\Xi^-(1320)$, three different vertices are constrained: $\gamma p \rightarrow K^+K^+\Xi^-$ (production vertex), $\Xi^- \rightarrow \Lambda\pi^-$, and $\Lambda \rightarrow p\pi^-$. Each event is required to converge and is given a confidence level and χ^2/NDF value based on how likely it is to be the desired reaction. The $\Lambda\pi^-$ invariant mass as a function of χ^2/NDF are shown

for each of the data sets in figure 4.3. These histograms show that events with a high χ^2/NDF are typically background as expected. All the χ^2/NDF distributions beyond 15 are flat with no structures in the invariant mass distributions. A χ^2/NDF cut of 3.5 is applied to kinematic fit results. The effect of this cut on the cross section is discussed later in section 6.6.2. A histogram showing the number of events appearing within the $\Xi^-(1320)$ mass range for each run period for data and Monte Carlo is also shown in figure 4.3. This histogram shows that the effect of χ^2/NDF is similar between data and Monte Carlo as well as that the level of background is consistent in data as the cut is loosened.

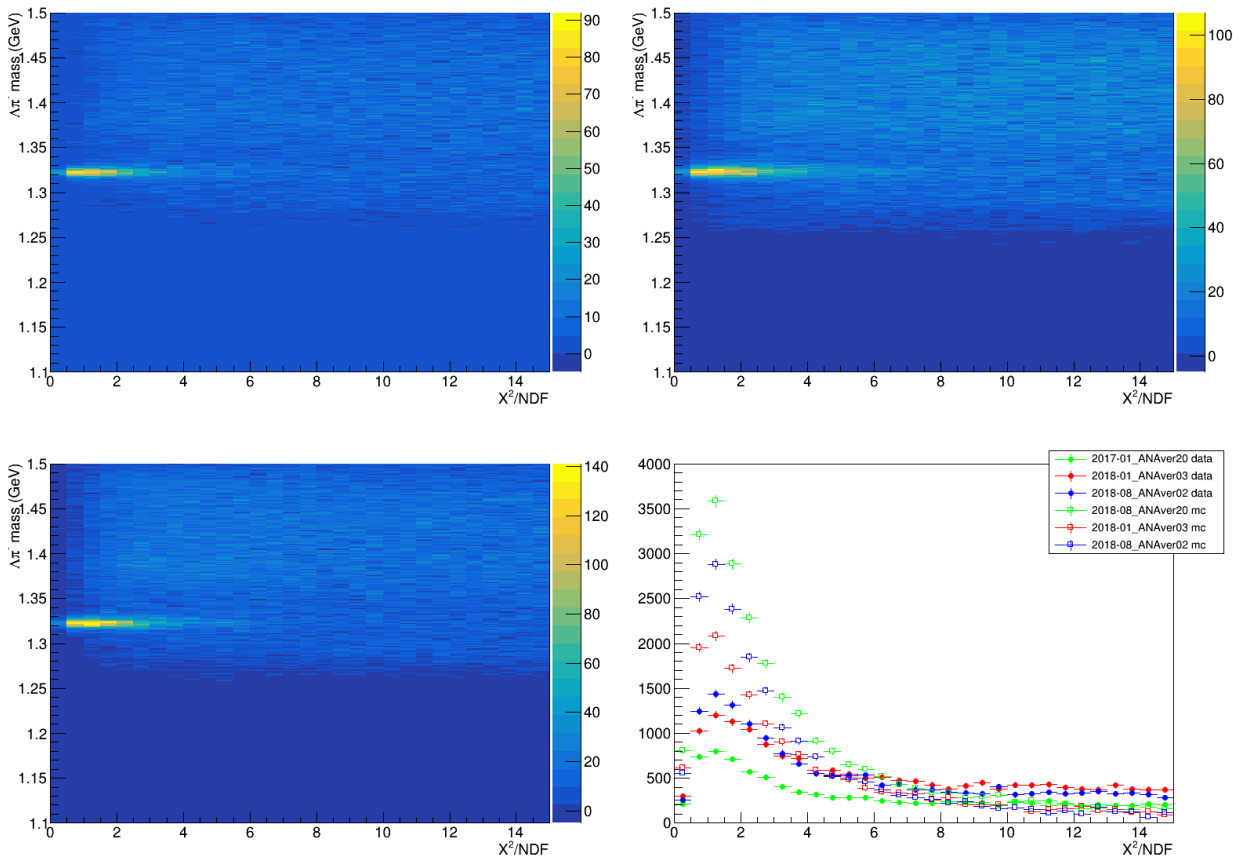


Figure 4.3: Invariant mass spectrum for $\Xi^-(1320) \rightarrow \Lambda\pi^-$ versus the χ^2/NDF from the kinematic fit in the Spring 2017 data set (top left), Spring 2018 (top right), Fall 2018 (bottom left). The yields in the slice of $\Lambda\pi^-$ mass containing $\Xi^-(1320)$ as a function of the χ^2/NDF for data and Monte Carlo. All distributions are flat beyond χ^2/NDF of 15. (bottom right).

4.2 Events After Selection

The signature for the octet ground state $\Xi^-(1320)$ can be observed in the data through the above reaction where the detected final state particles are $K^+K^+p\pi^-\pi^-$. The $\Lambda\pi^-$ invariant mass distributions from data are shown in figures 4.4. Included are the distributions using the measured 4-momentum, as well as the 4-momentum that is output after the kinematic fit. The kinematic fit improves the overall resolution from ~ 7 MeV to ~ 4 MeV. This work was used as the example for the detector resolution in the overall GlueX Spectrometer publication [23]. The background for all the distributions is relatively flat. The small fluctuation at approximately 1.38 GeV is due to a $\Sigma^-(1385)$ resulting from a mis-identification of an initial kaon for the final state of $\gamma p \rightarrow K^+\pi^+\Sigma^{*-} \rightarrow K^+\pi^+p\pi^-\pi^-$. The dip in the kinematically fit spectrum at 1.5 GeV is an artifact of the loose mass constraint on Ξ during the analysis launch for the reaction.

The kinematically fit spectrum is fit in order to extract the yields for $\Xi^-(1320)$. The Cascade baryon decays weakly resulting in a much longer time scale than a strongly decaying particle. Since the natural width of a resonance is inversely proportional to the lifetime, the natural width for the Cascade baryon is negligible in comparison to the detector resolution with an order of much less than an eV for the natural width and MeV for the resolution. Therefore, it is safe to assume that the entirety of the width of the distribution can be accounted for by the resolution of the detector. The signal is thus represented by a gaussian distribution. The background is modeled by a second order Chebyshev polynomial of the first kind. The primary reason for the choice in model is due to the stability of the fit over a normal polynomial due to reduced correlations between the coefficients [37]. There is a yield of 3081 ± 78 events from the Spring 2017 data, 4755 ± 100 from the Spring 2018 data, 5291 ± 84 from the nominal energy Fall 2018 data, and 314 ± 23 for the low-energy Fall 2018 data.

The kinematics for these events were as anticipated from the original GlueX proposals, shown in figure 4.2. The momentum vs polar angle distributions for each of the three particle types are shown in figure 4.5. There are two kaons with vastly differing kinematics, one at high momentum and low polar angle and the other with low momentum and high polar angle. Though the high momentum kaon is lower in momentum than that predicted by the proposal, it is still outside of the reach of direct kaon identification using the timing in the detectors. At that momentum it is indistinguishable from a pion at the same momentum. When the reaction is considered as a whole

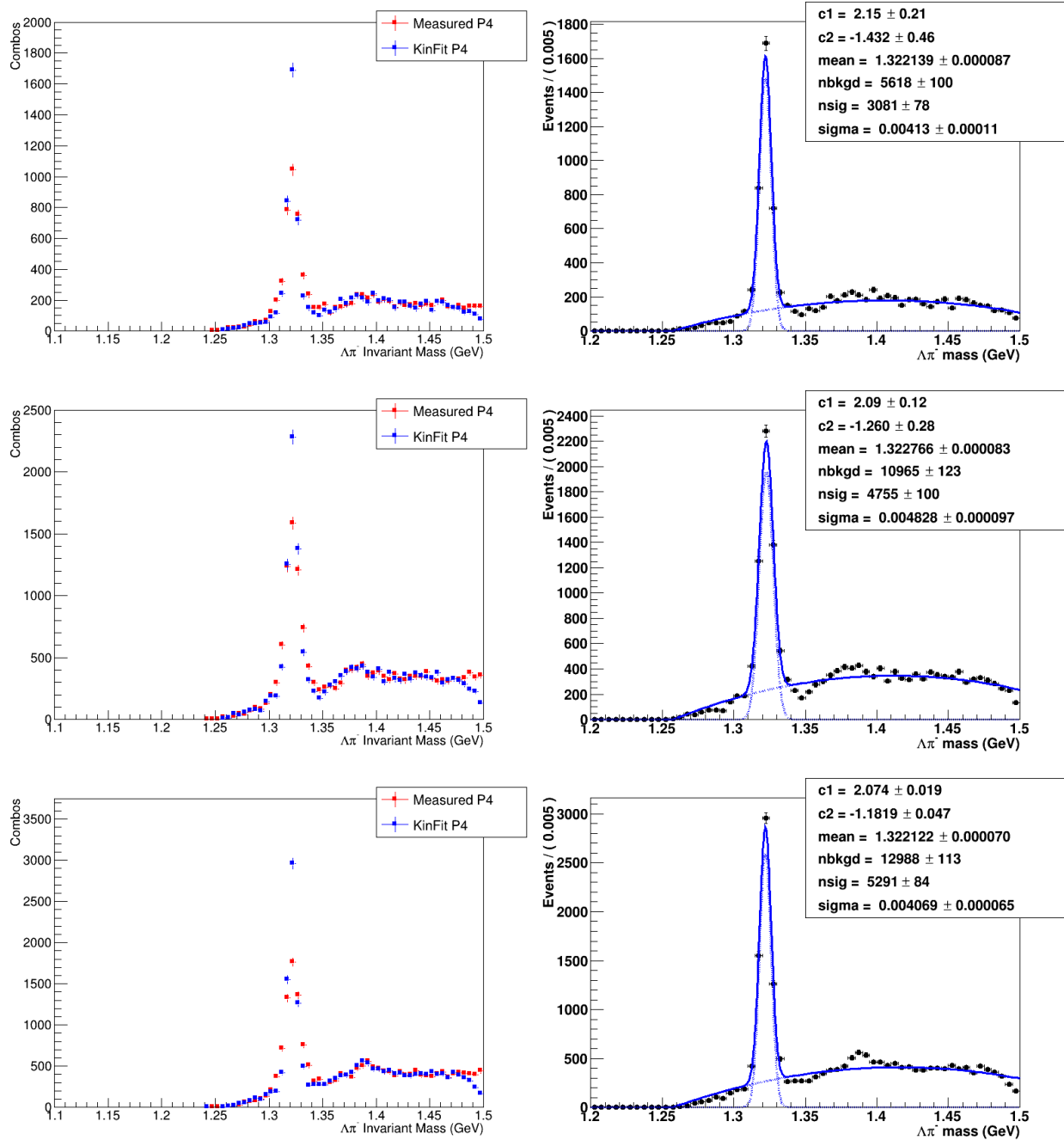


Figure 4.4: Invariant mass spectrum for $\Xi^-(1320) \rightarrow \Lambda\pi^-$ in the Spring 2017 data set (top), Spring 2018 (middle), and Fall 2018 (bottom). The left column shows the $\Lambda\pi^-$ invariant mass using the measured and kinematically fit 4-momenta while the right shows the overall fit of the data.

with the constraints previously mentioned, the invariant mass distribution still shows a relatively clean peak for the Ξ^- . Therefore, while the kaon is outside of the direct identification range of GlueX, it is still able to be identified indirectly. Alternatively, the second kaon from the decay of the intermediate hyperon is much lower momentum, it is clearly within the momentum range in which it is distinguishable from a pion at the same momentum. It is also the only particle at very large polar angles and is therefore largely detected by the BCAL. The proton and the two pions have similar kinematics. Both are low momentum and low polar angle. Though the low momentum kaon, the proton, and the pions are well within the region of momentum separation, there is a concern due to their proximity to the lower threshold of measurable momentum. This concern will be discussed in further detail in section 6.6.1.

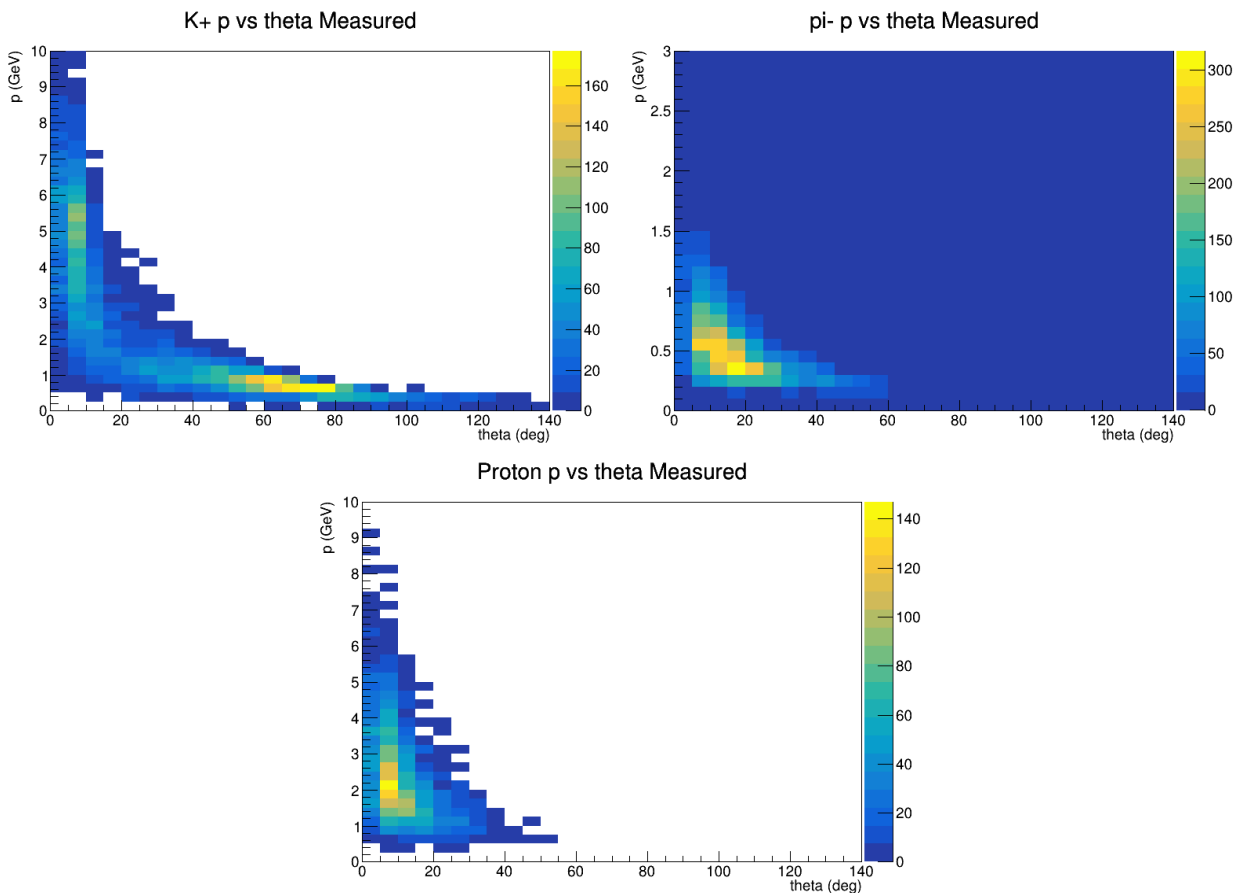


Figure 4.5: Measured momentum vs polar angle distributions for events within the $\Xi^-(1320)$ mass peak for the Spring 2017 run period. The distributions are for the two kaons (top left), two pions (top right), and the proton (bottom).

Part of the kinematic fit was the constraint on the vertex positions for the production vertex, the Cascade baryon decay vertex, and the Lambda baryon decay vertex. Both Ξ and Λ have detached vertices resulting in a measurable distance traveled in the detector before decaying. The mean lifetime for Ξ is 163.9 ps and for Λ is 263.2 ps [1]. This results in approximate distances traveled before decay ($c\tau$) of 5 cm for Ξ and 8 cm for Λ . Figure 4.6 shows the distributions for the vertex positions for each run period. It can clearly be seen that the vertex of Ξ and Λ move a measurable distance from the production vertex. The production vertex aligns with the target location which is at a z-position of 50-80 cm in the GlueX coordinate system.

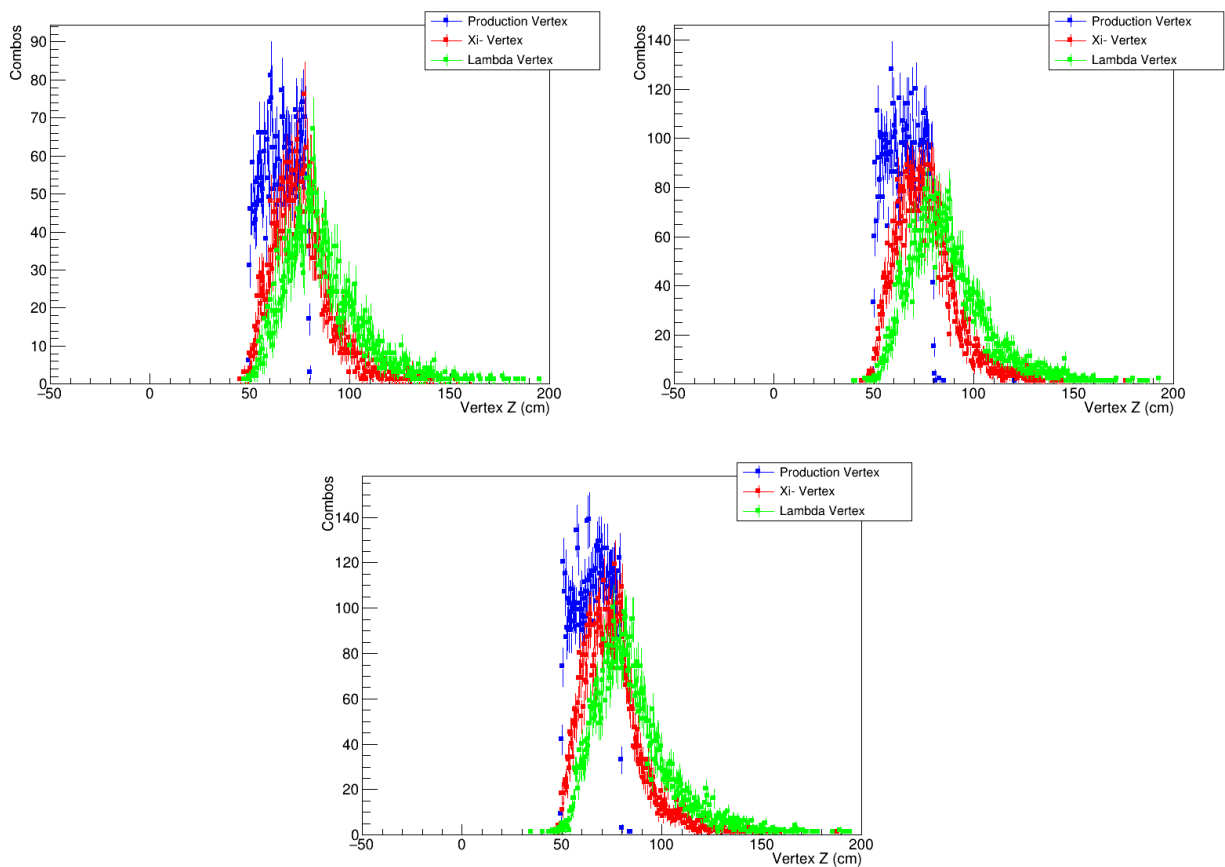


Figure 4.6: Vertex locations in the GlueX coordinate system for the production vertex, the decay vertex of Ξ , and the decay vertex of Λ for Spring 2017 (top left), Spring 2018 (top right), and Fall 2018 (bottom).

In the proposed production mechanism, there is an intermediate hyperon produced which subsequently decays into a low momentum kaon and a Cascade baryon. Since this intermediate hyperon decays strongly, there is no separation in the vertices to distinguish between the kaons in that manner. The kaons appear in two different kinematics regions of phase space which allows one to separate them via their momentum or polar angle. This work proposes separating them by polar angle and will be discussed later in the Monte Carlo studies shown in chapter 5. The momentum transfer $-t$ can be defined in this reaction as shown in equation 4.1.

$$t = (p_\gamma - p_{K+t})^2 \quad (4.1)$$

The distribution for each of the run periods is shown in figure 4.7. The value known as the t -slope is the slope of the exponential decay. Each distribution has a resulting t -slope of $\sim 1.4 \text{ GeV}^{-2}$.

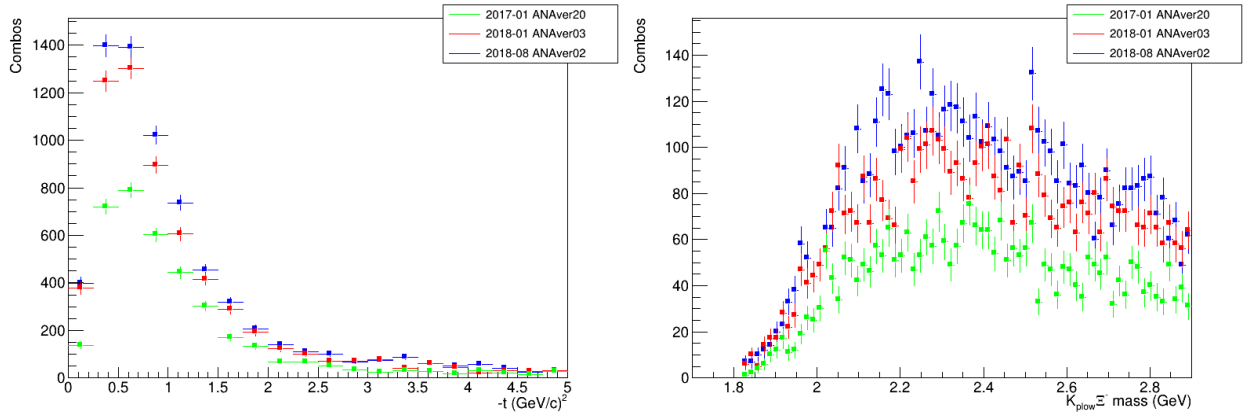


Figure 4.7: (left) The $-t$ distributions for each of the different run periods.(right) The invariant mass of the intermediate hyperon formed from the low momentum kaon and Ξ .

In conjunction with the $-t$ distribution, which uses the high momentum kaon, the low momentum kaon can be combined with the Ξ to form the intermediate hyperon. It can be seen in figure 4.7 that there are no peaks in mass spectrum. This is likely due to the fact that there are many hyperons that contribute. It would require an amplitude analysis to separate out the contributions to the intermediate hyperon.

CHAPTER 5

MONTE CARLO EVENT SIMULATION FOR $\Xi^-(1320)$

Monte Carlo produced at GlueX typically utilizes MCwrapper, which is a set of scripts to standardize the production of Monte Carlo for easy comparison between analysers [38]. The first step in Monte Carlo production is the generation of 4-vectors associated with the particles of interest. The amount of input information used to produce these 4-vectors can vary depending on the known information, from using isobar decays of particles to using amplitudes to impact the kinematic distributions. These produced 4-vectors are then passed through Geant4, which is a software used to simulate detector response [33]. Geant4 can also handle more complicated decays such as detached vertices by using the PDG value of the mean lifetime of a particle [33]. In order to make the Monte Carlo events look more like data, the hits in the detector are then smeared. These data are subsequently treated as actual data are. They are reconstructed and skimmed over in the same way as section 3.2.

5.1 Monte Carlo Generation

This work creates Monte Carlo using the genr8 generator [39] for the reaction $\gamma p \rightarrow K^+ Y^* \rightarrow K^+ K^+ \Xi^-(1320)$ using the MCwrapper [38] robot for the Open Science Grid. The particles are allowed to decay in Geant4 [33], which allows the detached vertices to be handled correctly and for the branching ratios to be built into the Monte Carlo production. Beam properties to produce the beam spectrum to match data are taken from values stored in the Calibration Constants DataBase (CCDB) from the PS.

Initial Monte Carlo sets showed a beam current dependence on the efficiency as shown in figures 5.1. In the Spring 2017 run period, there were two distinct beam current intensities. The low intensity period occurred between run numbers 30274 and 30788. After run 30788, the beam current was increased. The efficiency has a sharp drop for the run number corresponding to the switch to high beam intensities. In the Spring 2018 run period, there was also an issue with the gas

inside the Central Drift Chamber (CDC). As seen in figure 5.1, as the CDC gas mixture degraded, the efficiency for detecting Ξ^- also dropped.

The Monte Carlo events used for this measurement include the full run ranges of each run period. This scales the number of events per run to be proportional to the number of events in the data. This should accurately account for the beam current dependence. The software used is the same as that associated with the respective reconstruction and analysis launches. Random triggers are also included for each Monte Carlo set.

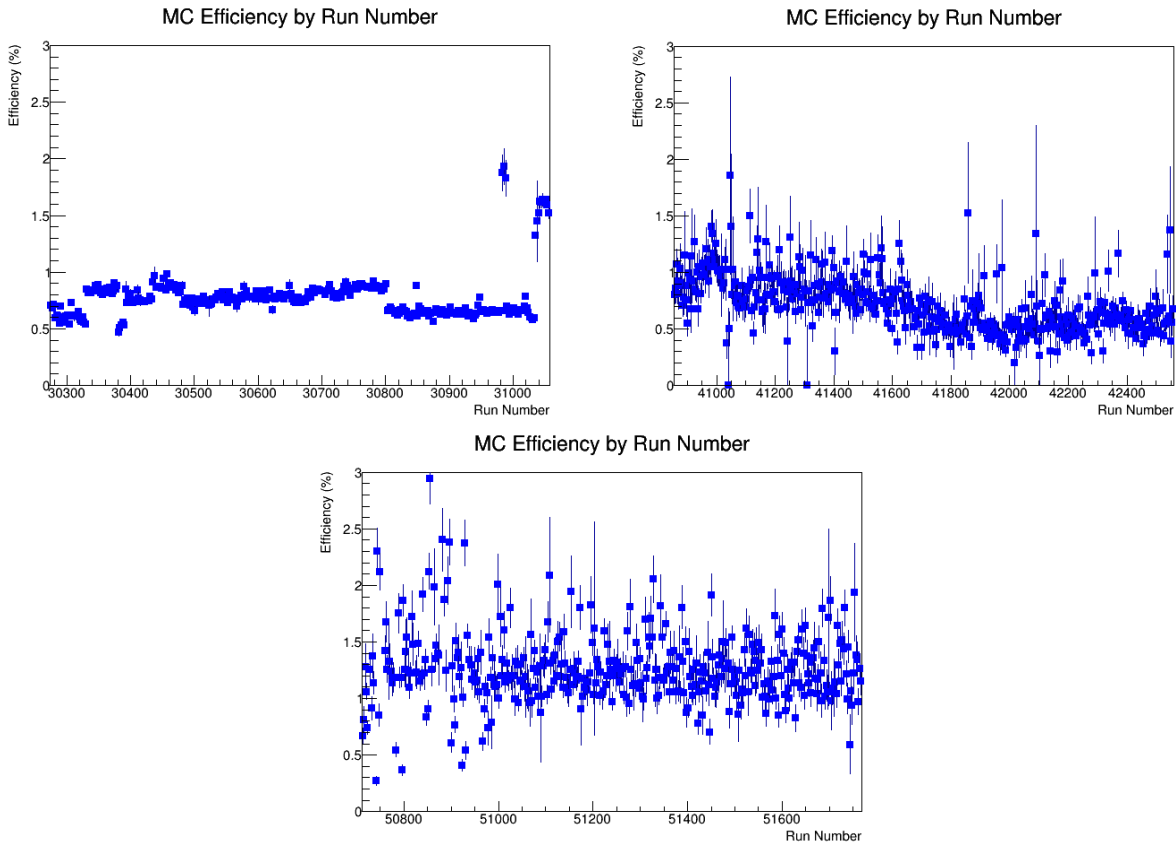


Figure 5.1: Efficiency by run number for each of the different run periods: Spring 2017 (top left), Spring 2018 (top right), and Fall 2018 (bottom)

5.2 Monte Carlo/Data Matching

The input parameters for the generator include the mass and width of every particle and the t -slope of the reaction. The values for the mass and width for the known particles are taken from

the PDG. This leaves three free parameters for the generator in order to match to data. These include the mass and width of the intermediate hyperon and the t -slope for the reaction. It was found that a sufficiently large mass of the intermediate hyperon greatly constrains the channel.

As mentioned in chapter 4, the two kaons are both produced at the production vertex which leaves ambiguity in the determination of the momentum transfer t . In Monte Carlo, it is known which kaon is which due to the production of the intermediate hyperon being built into the reaction. The two proposed ways of identifying the initial kaon were via momentum or polar angle separation with the decay kaon. The two distributions for the momentum and the polar angle of the decay kaon versus the initial kaon are shown in figure 5.2. In both of these distributions the decay kaon is on the y -axis and the t -channel produced kaon is on the x -axis. The red curve in both histograms represents the possible selection criteria by either momentum or polar angle. It can be seen that the selection by polar angle is correct more frequently, but by a marginal amount (99.3% of the time vs 97.3%).

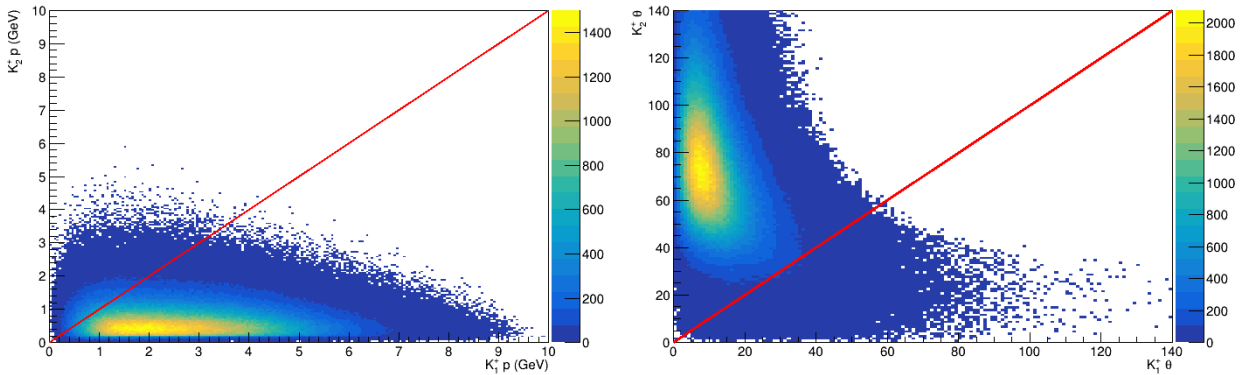


Figure 5.2: The comparison of the momentum (left) and polar angle (right) for the two kaons in Monte Carlo. K_2 denotes the kaon from the decay of the intermediate hyperon and K_1 denotes the initial kaon produced at the production vertex.

A large number of tests were run for varying values for the three free parameters. Each test varied the t -slope, intermediate mass, or intermediate width. The Monte Carlo is then treated the same as data, including the determination of which kaon is used for the calculation of the momentum transfer. For a subset of these tests, the t distribution is scaled to the same intensity as data and plotted in figure 5.3. In each plot, the chosen t -slope values (0.0, 0.7, 1.4, 2.1, 2.8, 3.5 GeV^{-2})

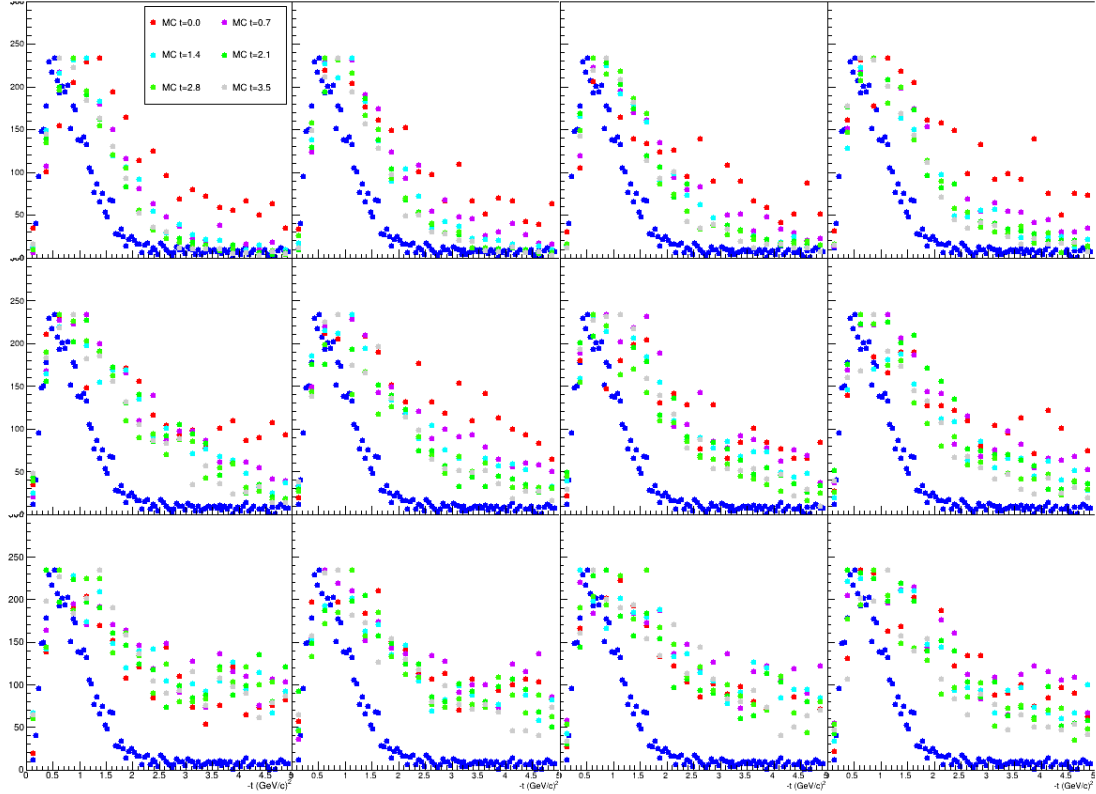


Figure 5.3: The distributions of $-t$ for Fall 2018 (blue) and varying input parameter tests. The colors represent different input t -slopes, across a row increases the width of the intermediate hyperon (0.4, 0.6, 0.8, 1.0 GeV), and down a column increases the mass (2.0, 2.4, 2.8 GeV).

are shown for a single value of intermediate mass and width. Across a row, the intermediate hyperon width increases (0.4, 0.6, 0.8, 1.0 GeV) and the intermediate hyperon mass increases down a column with the values (2.0, 2.4, 2.8 GeV). The chosen values for the input parameters is a t -slope of 1.4 GeV^{-2} , and an intermediate of mass 2.0 GeV and width 0.4 GeV. This corresponds to the cyan distribution in the top left plot of 5.3.

The resulting high statistics sample of the chosen parameter set is shown in figure 5.4. The momentum transfer distributions agree reasonably well with the data, particularly the Spring 2017 sets. This is improved matching from what initial sets gave. The t distributions could be improved with further adjustment of the input parameters. While the t distribution is useful to compare as an overall summary of the reaction, the kinematics of individual particles are the most important

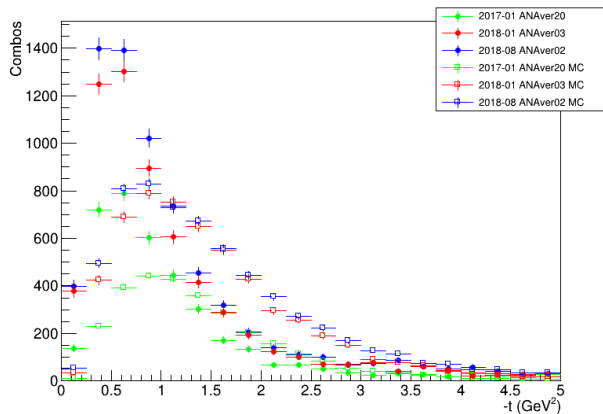


Figure 5.4: The distributions of $-t$ for each of the data sets with the chosen input parameters for generation of t -slope = 1.4 GeV^{-2} , and an intermediate of mass 2.0 GeV and width 0.4 GeV .

variables to match between data and Monte Carlo. The kinematics resulting from this choice of parameters can be found in figures 5.5. In each of these histograms, the number of entries in Monte Carlo is normalized to the number of events in data. It can be seen that the Monte Carlo agrees within reason with the data, particularly with the kaons. The protons vary significantly in their momentum distributions between data and Monte Carlo. The kinematics of the proton are a consequence of the earlier steps in the reaction and are not directly affected by the input parameters. The distributions could still be improved. The effect of the input parameters on the proton kinematics is being investigated, particularly in ranges of momentum transfer t . Future work could improve on the Monte Carlo by comparing the kinematics of all the particles as a function of the momentum transfer $-t$.

There is a known problem in Monte Carlo, that is being investigated, that may result in the loss of the low momentum protons. It is the inclusion of the CUTS card in Geant4 which affects how particles deposit their rest mass in the sub-detectors. If this is indeed the issue, the efficiency found in chapter 6 would increase with the return of the low momentum protons.

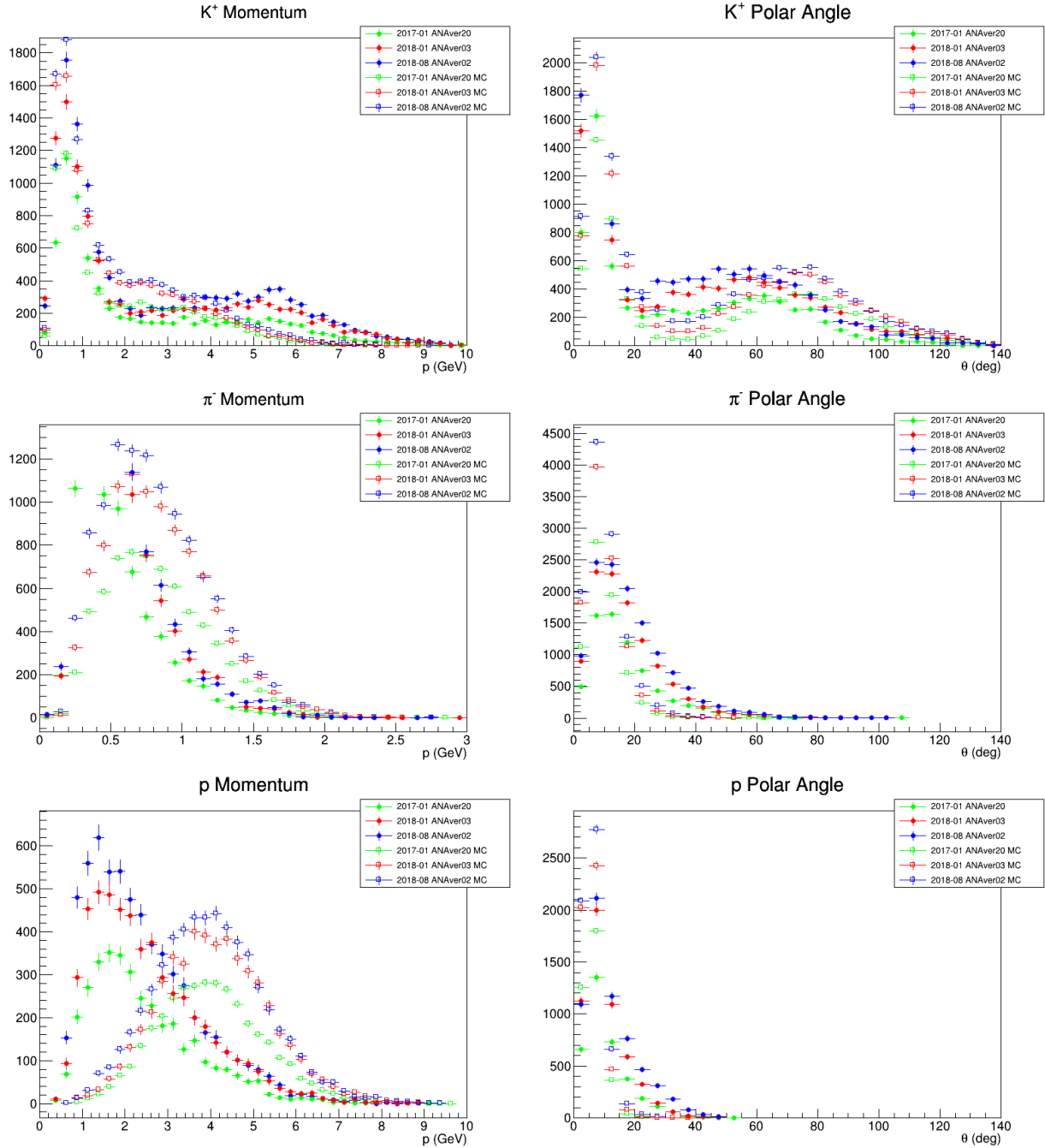


Figure 5.5: Kinematic comparison between data and Monte Carlo. The left histograms show the momentum distributions while the right column show polar angle distributions. The top row is for kaons, middle is pions, and bottom row is the proton.

CHAPTER 6

CROSS SECTION OF $\Xi^-(1320)$

A production cross section is a physics observable which describes the probability of the production occurring. The cross section is such that it is normalized to the incoming beam flux as well as the number of target particles. This allows for cross sections between experiments that consider the same production mechanism to be comparable. It is commonly quoted in the units of barns which have the dimension of area. It can be considered the effective area of the target particle seen from the perspective of the beam particle or photon in this case [36]. Cross sections are used to understand detector performance on an absolute scale. Differential cross sections are cross sections considering its dependence on a reaction variable such as beam energy, momentum transfer, or kinematic variables. The study of differential cross sections improves the understanding of the production mechanism by understanding the dependencies on such variables. The cross section is calculated by dividing the rate by the incident beam flux.

More specifically, the cross section for photoproduction of $\Xi^-(1320)$ is calculated using:

$$\sigma = \frac{N}{TargetFactor * Flux * BR_{\Xi} * BR_{\Lambda} * \epsilon} \quad (6.1)$$

The target factor represents the number of target particles per cross sectional area. This value is calculated by for a target of length L and density ρ by [36]:

$$TargetFactor[atoms/m^2] = \frac{N_A[atoms/mol] * L[m] * \rho[kg/m^3]}{A[kg/mol]} \quad (6.2)$$

where N_A is Avogadro's number, and A is the molar mass. For GlueX, this factor is $1.22 b^{-1}$ ($1.22 * 10^{-28} m^{-2}$) for a 29 cm long liquid hydrogen target cell. The number of signal events N is obtained from the fit of the data. The efficiency, ϵ , is the probability that the particles are detected if produced. This efficiency may be factored into several contributions. For instance, the incoming beam photon flux used in equation 6.1 is the tagged flux from the Pair Spectrometer (PS). Only the tagged flux needs to be considered as the efficiency of the PS is factored from the overall efficiency. Therefore, the efficiency of the PS tagging the flux is canceled from the overall

equation. For this analysis, the branching ratios were built into the efficiency as well. Monte Carlo is produced such that all decay modes are possible but only those with the final state of interest are detected. Generally, the Monte Carlo is the number of events detected divided by the number of events generated. Values for the efficiency quoted in the remainder of the document include the branching ratios such that $\epsilon' = \epsilon * BR(\Xi) * BR(\Lambda)$.

6.1 Fitting of Data

The yield is taken from the fit of the data using a Gaussian to model the peak and a second-order ChebyChev polynomial of the first kind to model the background. The yields for both the signal and background are free parameters within the fit. The yields have the accidental beam photons subtracted, as discussed in section 3.2.1, using 1 beam bunch on each side of the prompt signal peak and weighting them by -0.5 and the scaling factor associated with the corresponding run that the event occurred in. The overall fits from the full beam energy range were shown in figures 4.4 previously. The resulting yields as a function of beam energy for each of the data sets are shown in figure 6.1.

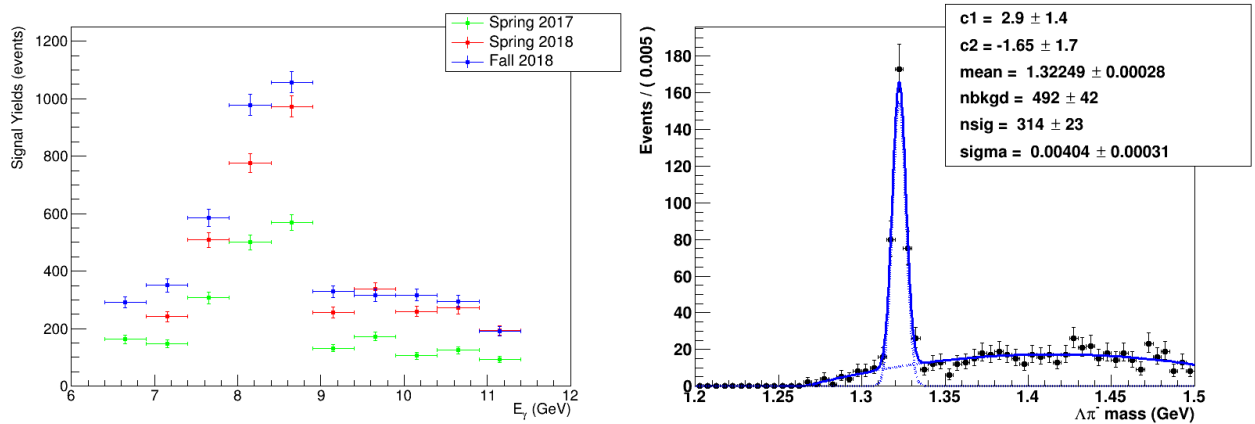


Figure 6.1: (left) The signal yields for Spring 2017 (green), Spring 2018 (red), and Fall 2018 nominal energy range (blue) resulting from the fits to each bin. (right) The fit for the low energy data from the Fall 2018 run period.

As previously mentioned, there was a short time during the Fall 2018 run in which the coherent edge of the beam energy spectrum was moved to approximately three to six GeV. This was achieved by moving the Pair Spectrometer operating energy down and orienting the diamond to have the

coherent edge within the beam energy region measured with CLAS. As discussed in section 2.2.1, the angle between the electron beam and the diamond’s crystalline plane controls the energy at which most of the beam photons are produced. The resulting fit for that low energy data is shown in figure 6.1. As it was a short run, the yields are limited but it should allow for some overlap in the previous total cross section measurements performed by CLAS, which had beam energies up to 5.4 GeV [8]. The effect of binning of the $\Lambda\pi^-$ invariant mass as well as the order of the function are both shown later in section 6.6.4.

6.2 Monte Carlo Efficiency

The efficiency used is that of the $\Xi^-(1320)$ and requiring that it is within the acceptance of the detector and is reconstructed. All decay modes are produced and then only the decays of $\Xi^- \rightarrow \Lambda\pi^- \rightarrow (p\pi^-)\pi^-$ are analyzed. The resulting quoted efficiency is thus more accurately defined as $\epsilon' = \epsilon * BR(\Xi^- \rightarrow \Lambda\pi^-) * BR(\Lambda \rightarrow p\pi^-)$ as previously stated. Because of this, the cross section does not need to account for the branching ratio as it cancels out with with the branching ratios from the efficiency calculation in equation 6.1. The efficiency as a function of beam energy that is used for the cross section measurement is shown in figure 6.2. The efficiency for each run period is not consistent because the Monte Carlo models the data from the specific run periods.

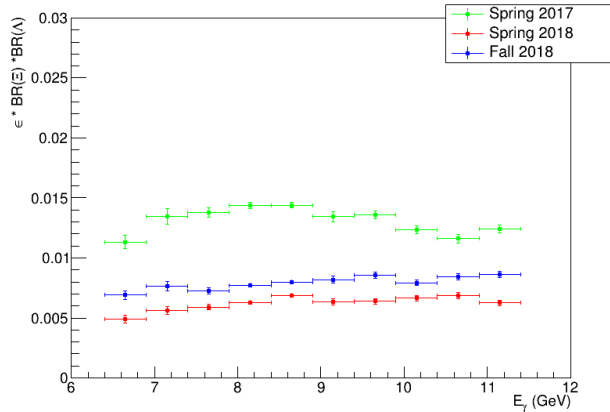


Figure 6.2: The Monte Carlo efficiency for Spring 2017 (green), Spring 2018 (red), and Fall 2018 nominal energy range (blue) found by dividing the yields in Monte Carlo by the amount of events generated.

6.3 Flux

The incoming photon flux values are obtained from the script in `hd_utilities` which accesses the values from CCDB for the PS. The flux is determined using the query for runs that are considered production and are approved physics runs to be analyzed. The run ranges of the different run periods are 30274-31057 for Spring 2017, 40856-42577 for Spring 2018, 50677-51768 for Fall 2018, and 51384-51457 for Fall 2018 low energy.

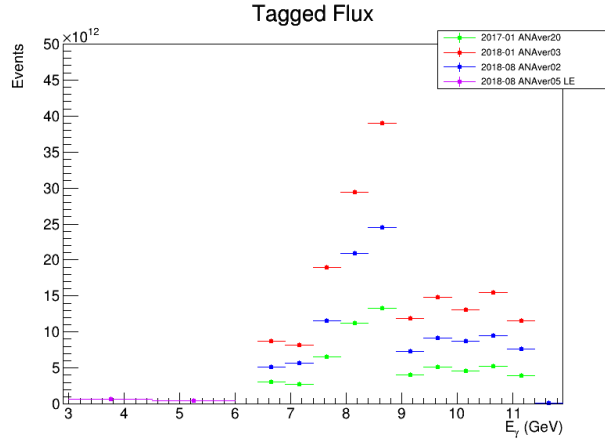


Figure 6.3: The incoming beam flux as a function of beam energy for Spring 2017 (green), Spring 2018 (red), Fall 2018 nominal energy range (blue), and Fall 2018 low energy range (violet).

The number of runs used in the flux values were compared to that used in the data. The Spring 2017 flux and data run numbers agreed exactly where both sets included 347 runs. The Spring 2018 flux values included 543 runs while data included 548 runs. The flux values were not included for runs 41007, 41173, 41207, 41221, and 42182. These run numbers were removed from the data trees. The Fall 2018 data set had a similar issue in which the flux values included 496 runs and data 450 runs. In this case, run 51172 was not included for the flux values but was for data. Additionally, run numbers in the range 51384 to 51457 (low energy runs) were included in the flux calculation but aren't included in this analysis. The overlap of 449 runs was used for the Fall 2018 run period. The resulting histogram containing each data set are shown in figure 6.3.

6.4 Total Production Cross Section Results

The final results combine each of the pieces and their uncertainties shown in equation 6.1 The final results are compared with the CLAS g12 results which were extracted from the image in the paper using Engauge Digitizer [40] and then converted to being a function of beam energy instead of as a function of \sqrt{s} . The two CLAS results shown in section 1.3.2 demonstrate a total cross section for $\gamma p \rightarrow K^+ K^+ \Xi^-$ that rises from threshold and then appears to level off with increasing beam energy. Based solely on these results and the theoretical model from Nakayama [41], one could expect that there is a continued plateau with increasing beam energy. This analysis currently shows a much sharper drop in cross section in the GlueX energy regime as seen in figure 6.4. Due to the mismatch for the lower energy data and the apparent kinematic holes in the Monte Carlo, it is likely that the overall normalization is off by a factor close to 1.5 which is discussed further in section 6.6. This would result in a less sharp drop in the cross section at increasing energies.

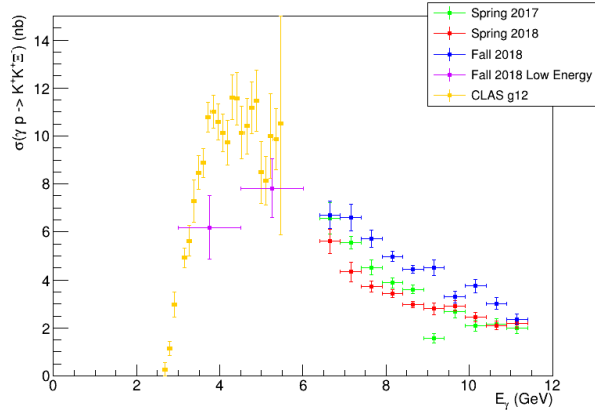


Figure 6.4: The total production cross section for $\gamma p \rightarrow K^+ K^+ \Xi^-$ as a function of beam energy for Spring 2017 (green), Spring 2018 (red), Fall 2018 nominal energy range (blue), and Fall 2018 low energy range (violet).

The two spring data sets match quite well for most of the beam energies. The discrepancy in the Fall 2018 data set at the coherent edge (~ 9 GeV) is likely due to statistical fluctuations and bin migration. The transition from one bin to the next has a significant drop in statistics for all components of the cross section. The Fall 2018 data is arguably the best data set of the Phase-I

GlueX running in terms of statistics and stability of the beam. It is also the least understood data set as it has been the least studied by the collaboration as a whole.

6.5 Differential Cross Section

The total cross section measurement was extended to the differential cross section as a function of the momentum transfer $-t$. The differential cross section for $\Xi^-(1320)$ was calculated using:

$$\frac{d\sigma}{dt} = \frac{N}{\text{TargetThickness} * \text{Flux} * \epsilon' * \Delta t} \quad (6.3)$$

The differential cross section was calculated in two fashions, binned in and integrated over beam energy. Both are shown here. The component pieces for the differential cross section as a function of $-t$ are shown in figure 6.5. The differential cross section should scale proportional to the factor e^{-bt} where b is the t -slope. It can be seen that the lowest bins in t in the differential cross section do not represent an exponential. This is likely due to the minimum threshold for the momentum that is reconstructed in the detector. This is also demonstrated by the Monte Carlo efficiency as it approaches zero as t approaches zero GeV^2 . A model is needed to accurately extrapolate over this region of the differential cross section. This would also increase the values for the total cross section.

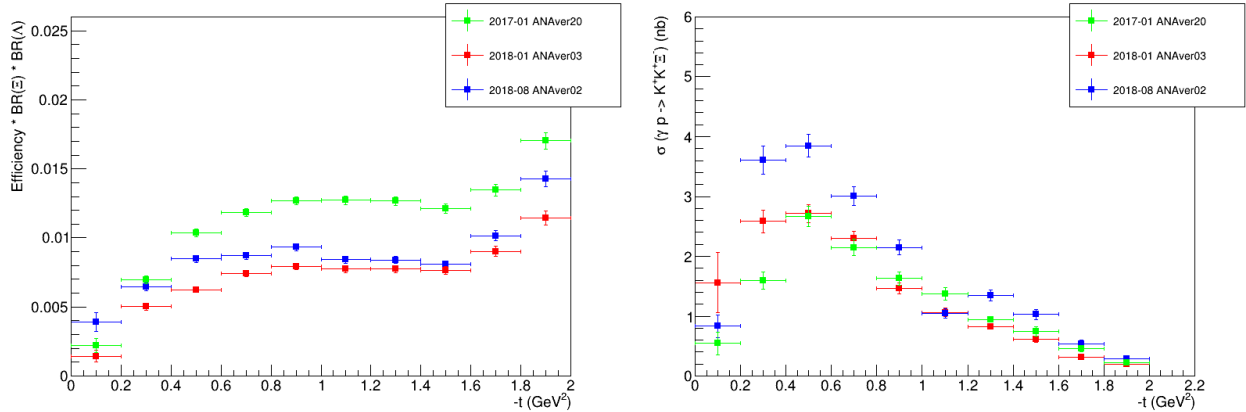


Figure 6.5: The efficiency and differential production cross section for $\gamma p \rightarrow K^+ K^+ \Xi^-$ as a function of momentum transfer to the kaon for Spring 2017 (green), Spring 2018 (red), and Fall 2018 nominal energy range (blue).

This can continue to be extended to a differential cross section in terms of momentum transfer as well as being binned in beam energy like the total production cross section. Typically, this differential cross section is shown on a log scale as it is expected to follow an exponential decay distribution. The distributions shown in figure 6.6 agree decently well in terms of order of magnitude and shape especially in the beam energy range of the coherent peak as that has the largest statistics. If one only considers the data points in which there are decent statistics such as the central region of $-t$ for any given histogram, the differential cross sections have a linear tendency in a log scale as expected. There are quite a few points in which the statistics, or another factor, is poor such as the lowest $-t$ bin which has both poor efficiency and low statistics. It is also notable that the high $-t$ bins which have low statistics and overall cross section.

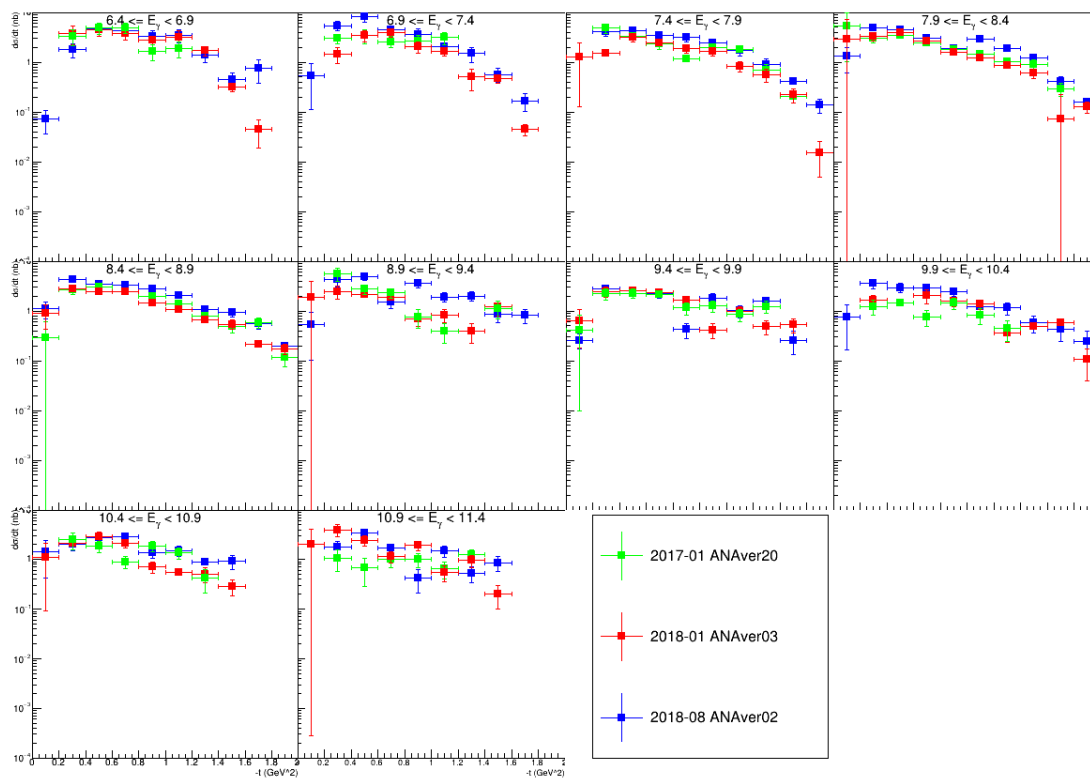


Figure 6.6: The differential production cross section on a log scale for $\gamma p \rightarrow K^+ K^+ \Xi^-$ as a function of momentum transfer to the kaon and beam energy for Spring 2017 (green), Spring 2018 (red), and Fall 2018 nominal energy range (blue).

If instead the differential cross section is considered on a linear scale, the distributions should

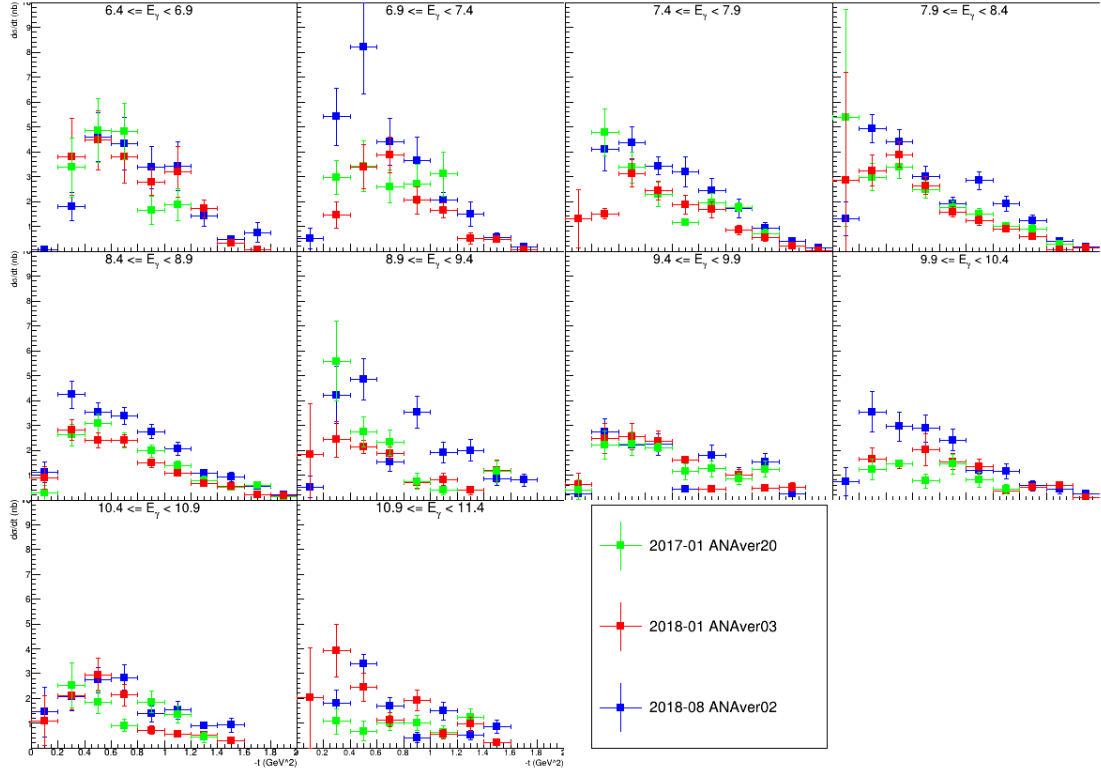


Figure 6.7: The differential production cross section on a linear scale for $\gamma p \rightarrow K^+ K^+ \Xi^-$ as a function of momentum transfer to the kaon and beam energy for Spring 2017 (green), Spring 2018 (red), and Fall 2018 nominal energy range (blue).

follow an exponential decay distribution. This will more easily allow the comparison between the data sets. Similar to the conclusions to the log scale differential cross sections, the data sets agree fairly well when there are sufficiently high statistics. Much like the total cross section, the two spring data sets agree within reason within statistics while the Fall 2018 data set appears to be higher for most kinematic regions. The lowest data point in terms of t for all histograms is still problematic with low statistics and poor efficiency.

6.6 Systematic Errors and Studies

With the measurement of a cross section, there are many notable checks and studies to be completed. This is not an exhaustive list but includes some of the notable results. There are choices that have a direct impact in the result of the cross section that must be studied to make

sure there is no inherent bias. These include choices such as the fit functions used to extract yields, any cuts on the data or Monte Carlo, and binning of the data. One also should perform systematic checks such as splitting the data in subsets as the choice in subset should not have an effect on the production cross section. These subsets can be determined in many ways. The cross section has already been shown in terms of run periods which have passage of time between them. Many factors could play a role in the differences, be it from the accelerator, the individual detectors, or changes in the reconstruction code or calibration improvements. Other subsets such as by radiator orientation should see less of an effect within a run period as the radiator is changed several times a day during data taking. Similarly, systematic checks of the kinematic distributions, the stability of the detector resolution, and mass from the fits are important to verify. These don't contribute to the systematic uncertainties of the measurement, but instead can point to potential problems that need to be fixed.

6.6.1 Phase Space Coverage

The first systematic check is that of phase space coverage. The total production cross section seems to be lower than expected by approximately a factor of 2. There is the potential for holes in phase space. One reference frame to consider is the Gottfried-Jackson frame. This frame is in the rest frame of a particle interest with the z -axis being aligned with the beam axis in the intermediate hyperon rest frame. The y -axis is chosen such that it is orthogonal to the production plane formed by the beam photon and the intermediate hyperon. If one considers the intermediate hyperon rest frame, it is expected that the kaon from the decay and the Ξ baryon are evenly distributed across the phase space. The kaon and Cascade baryon should travel back-to-back of each other. Figure 6.8 shows the definition of the frame in question.

Since the Ξ and the kaon from the decay of the intermediate hyperon are back-to-back, one can evaluate any holes in phase space by considering the kinematics of the kaon. This kaon should be evenly distributed across both ϕ and θ in this frame as the decay of the intermediate hyperon should be isotropic or at the very least symmetric. As seen in figure ??, this is not the case. The kaon tends to greatly prefer the backwards direction in polar angle. This is entirely unexpected, but it occurs in both data and Monte Carlo. There is a hole that covers approximately half of the phase space as the kaon doesn't occur in the forward direction. Presumably, the generated Monte Carlo should have the desired behavior if the problem arises within the analysis framework chain.

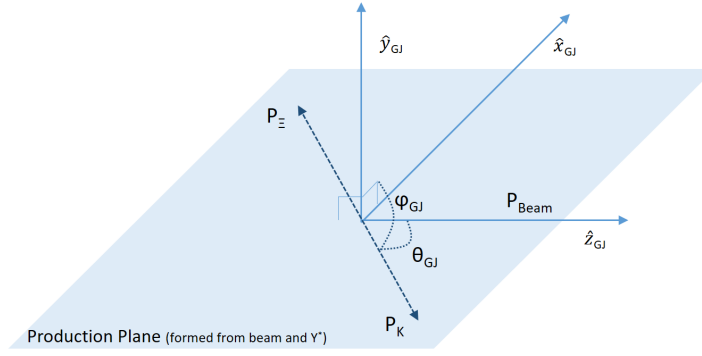


Figure 6.8: Depiction of the Gottfried-Jackson reference frame in which the intermediate hyperon is at rest and the z -axis is along the beam direction.

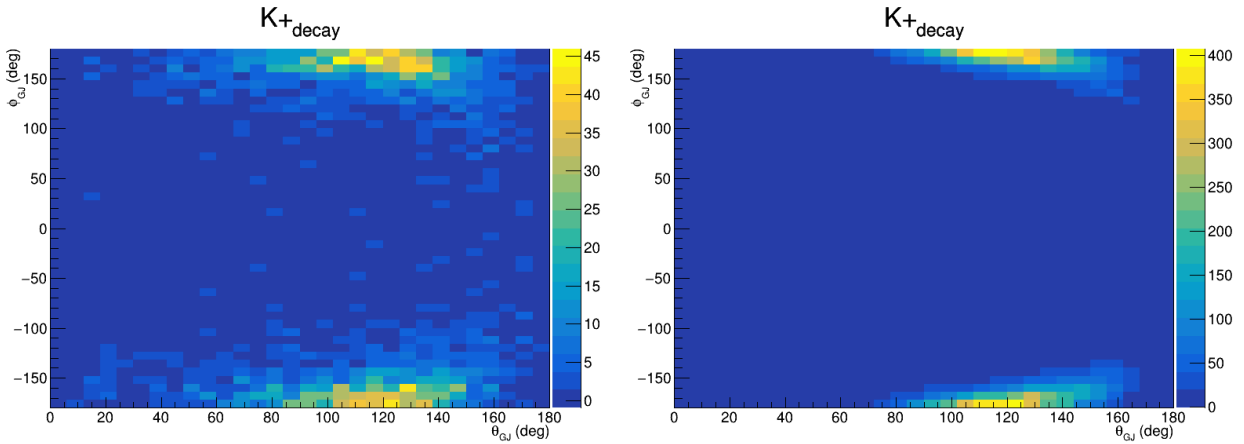


Figure 6.9: Polar angle vs azimuthal angle for the decay kaon in the Gottfried-Jackson rest frame of the intermediate hyperon for data (left) and Monte Carlo (right) for the Spring 2017 data set.

Figure 6.10 shows the generated Monte Carlo. Two problems of interest rise from these three plots. Firstly, the generated (or "thrown") Monte Carlo does not have the desired behavior. It is not symmetric nor isotropic in nature. The only requirement to be included in this plot is that there be a beam photon that occurs within a tagger counter. Naively it could be expected that the distribution is biased towards the backward direction by the selection of which is the t -channel kaon or the decay channel. As previously shown in figure 5.2, this is unlikely the case since the correct kaon is most commonly chosen as the decay kaon.

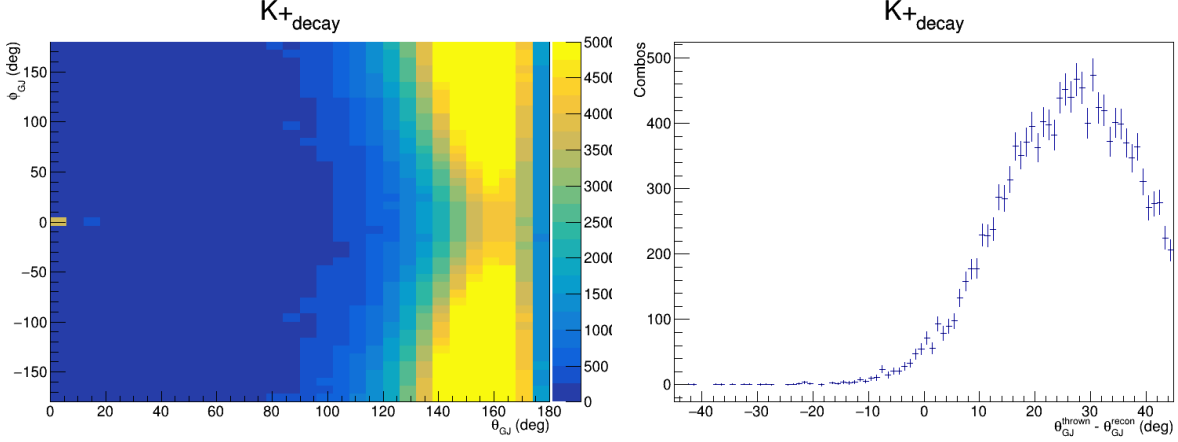


Figure 6.10: Polar angle vs azimuthal angle for the decay kaon in the Gottfried-Jackson rest frame of the intermediate hyperon for generated Monte Carlo (left) and the difference in the reconstructed and thrown polar angles (right) for the Spring 2017 data set.

The second issue is that the maximum in both the generated and reconstructed Monte Carlo occur at very different polar angles. This could be due to a problem in the reconstruction of the data or that the majority of the generated Monte Carlo is lost in that kinematic region. Figure 6.10 shows that in the process of the analysis, the polar angle of the decay kaon is shifted by an average of 30° . This points to the possibility of an issue with kaons at large polar angles. In the collaboration as a whole, kaons at large polar angles are just starting to be studied as a result of the very recent paper on $\gamma p \rightarrow K^+ \Sigma^0$ [27]. Improvements in track reconstruction are being implemented as work continues to progress. It is likely that these improvements help this reaction as well.

6.6.2 Effect of χ^2/NDF Cut

Because the selection criteria on the χ^2/NDF has the largest impact on this channel, it is necessary to consider the effects of this selection criteria on the overall cross section measurement. The expected distribution for cross section versus χ^2/NDF is expected to be flat. This distribution is considered for a single beam energy range in with high statistics, particularly 8.4 to 8.9 GeV. For calculating the cross section, the only values that change as a function of χ^2/NDF is the number of signal events and the number of Monte Carlo events. Therefore, this study will show if the

handling of data and Monte Carlo by the kinematic fit is similar. As can be seen in figure 6.11, the distributions are mostly flat as the χ^2/NDF selection criteria is loosened or tightened.

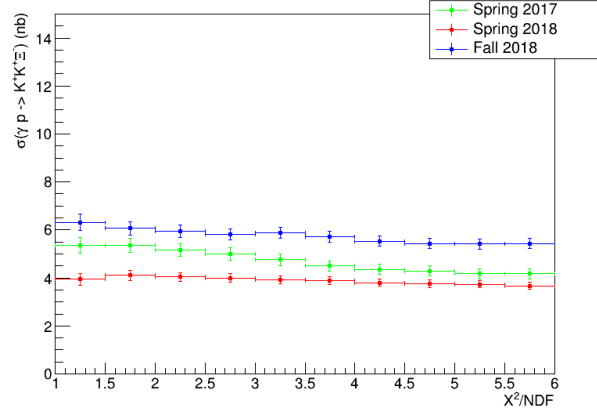


Figure 6.11: The total production cross section for $\gamma p \rightarrow K^+ K^+ \Xi^-$ as a function of χ^2/NDF for the kinematic fit for Spring 2017 (green), Spring 2018 (red), and Fall 2018 nominal energy range (blue).

6.6.3 Signal Resolution and Stability

Since each energy range in the total cross section has the yields exacted through a fitting procedure, one can verify the stability of the fit by looking at the parameters in the same ranges. The mass of $\Xi^-(1320)$ is a parameter in the fit. The accepted mass for this state is 1.32171 GeV [1]. For the overall fit with full statistics, the obtained values are 1.3221 GeV for Spring 2017, 1.3228 GeV for Spring 2018, and 1.3221 GeV for Fall 2018. Since $\Xi^-(1320)$ decays weakly, the resulting width is the detector resolution. The overall fit to the data shows that the detector resolution was between 4 and 5 MeV for each of the data sets.

Figure 6.12 shows the resulting mass and width for all the fits used in the total cross section measurement. The figure for the mass also includes a line to represent the known mass for $\Xi^-(1320)$. The mass in each of the energy ranges is flat but systematically higher than the known mass by approximately 0.5 MeV. The widths or detector resolution varies more drastically as a function of beam energy, ranging from 3 to 6 MeV in any given energy range.

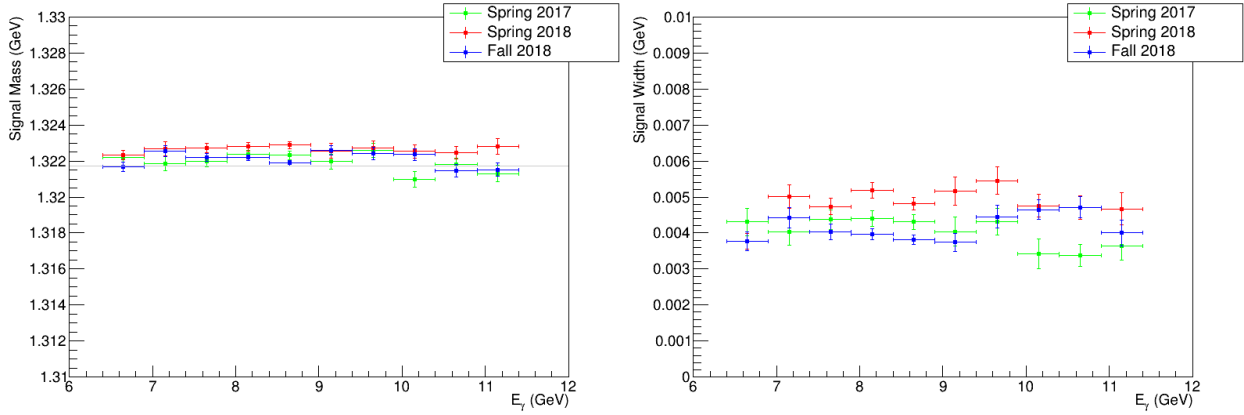


Figure 6.12: The mass (left) and width (right) for $\Xi^- (1320)$ for $\gamma p \rightarrow K^+ K^+ \Xi^-$ as a function of beam energy for Spring 2017 (green), Spring 2018 (red), and Fall 2018 nominal energy range (blue).

6.6.4 Effect of Binning and Fit Functions

The choice of how the total cross section is displayed should have little effect on the resulting values. The two main choices regarding the beam energy ranges include the width of the range and the starting points. The width of the ranges was allowed to vary from the nominal 500 MeV to 333 and 250 MeV. The starting point beam energy varied from the nominal 6.4 GeV to 6.3 and 6.5 GeV. The resulting effect of these choices is shown in figure 6.13.

The general trend between all the options is consistent. When considering the width of the ranges, there are data points in each set that are outliers. This is likely due to statistics especially for the smaller ranges. With regards to the starting point energy, the lower threshold for the flux measurement is approximately 6.3 GeV. It is expected that the lowest cross section point is an outlier as the flux measurement is poor and the uncertainty for the flux is also poorly measured. It appears that 6.5 is the more stable starting point energy. This is a logical conclusion as the coherent edge of the beam spectrum is located at 9.0 GeV which coincides with the beam energy ranges.

6.6.5 Miscellaneous Studies

A handful of additional studies have occurred that are not a systematic uncertainty but still worth mentioning. These include certain checks on the analysis as well as various changes minor

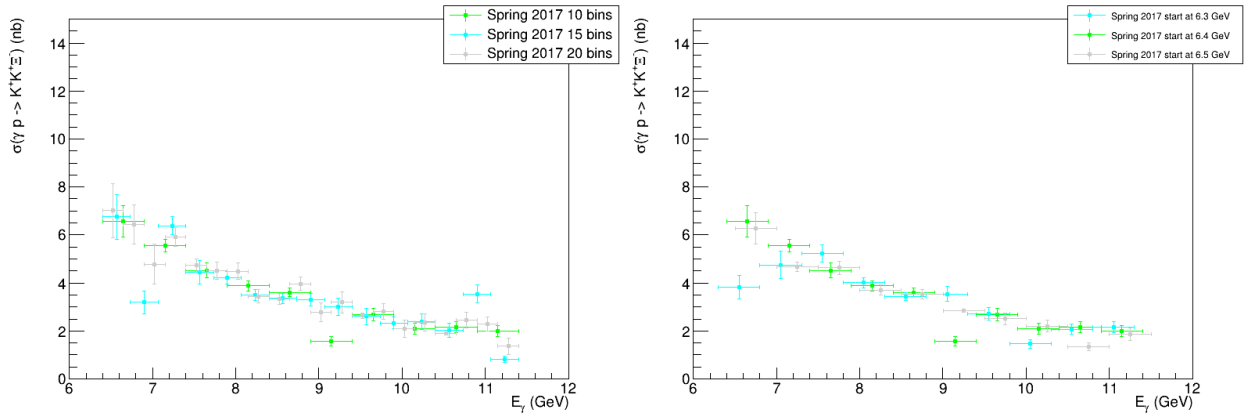


Figure 6.13: The total production cross section for $\gamma p \rightarrow K^+ K^+ \Xi^-$ as a function of beam energy for Spring 2017 with variations in energy range width (left) and energy range start values (right).

changes in the cross section calculation. Some of these studies include the effect on the cross section due to including the scale factor in the accidental subtraction, to using the thrown beam photon when determining the efficiency, and the effect of uniqueness tracking.

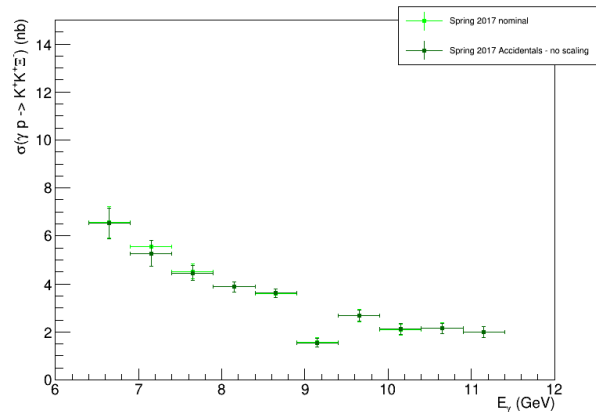


Figure 6.14: The total production cross section for $\gamma p \rightarrow K^+ K^+ \Xi^-$ as a function of incoming beam energy for the Spring 2017 data set with (light green) and without (dark green) the scaling factor included in the accidental subtraction.

Scaled Accidentals. Previously discussed in section 3.2.1, the accidental beam photons under the prompt peak is typically 5% higher than the average of the side peaks. Inclusion of the

scaling factor to increase the number of accidental beam photons is thought to make the systematic uncertainty on the flux determination negligible. As the scaling factor is small, one would anticipate that the effect on the overall cross section is small as well. This effect on the Spring 2017 data set is shown in figure 6.14, where the closed points represent the nominal measurement of the scaling factor included and the open points represent not including the scaling factor in the accidental subtraction.

Choice of Beam Photon for Binning. The incoming beam photon is used to determine the how each of the components of the cross section is binned. For the signal in data and the incoming photon flux, the determination of which energy range to be placed in is trivial. For Monte Carlo, the decision is not trivial. Each Monte Carlo event has two beam photon energies associated with it, the one given during generation and the one after reconstructing the Monte Carlo like data. The efficiency calculation is determined by dividing the number of reconstructed events by the number of generated events. The generated events only have the generated beam energy. The choice is then whether the reconstructed Monte Carlo is associated with the generated beam energy as in equation 6.4a or the reconstructed beam energy as in equation 6.4b.

$$\epsilon(E_\gamma) = \frac{N_{recon}(E_{\gamma thrown})}{N_{gen}(E_{\gamma thrown})} \quad (6.4a)$$

$$= \frac{N_{recon}(E_{\gamma recon})}{N_{gen}(E_{\gamma thrown})} \quad (6.4b)$$

By using the generated beam energy (6.4a), the efficiency is strictly for a particular beam energy. A complication that this causes is that of bin migration. Since the cross section is given for a particle beam energy range, events that are generated in one range and then reconstructed in another shift the efficiency.

For example, one of the cross section points has a range from 8.4 to 8.9 GeV in beam energy. If a beam photon is generated at 8.899 GeV in energy and then reconstructed at 8.901 GeV in energy and the efficiency is determined With equation 6.4a. The efficiency is straightforward as both the numerator and the denominator occur within the same energy range. The Monte Carlo is then no longer treated just like data since it is possible that the beam photons in data can have a similar shift. For equation 6.4b, the efficiency is no longer as trivial. The efficiency for the energy range in question lowers due to the event being included in the denominator, but not the numerator. The efficiency in the adjacent energy range also increases for the opposite reason. In this case, the

reconstructed Monte Carlo is treated much the same as data. It could be argued that either option is the more correct way to handle the efficiency determination.

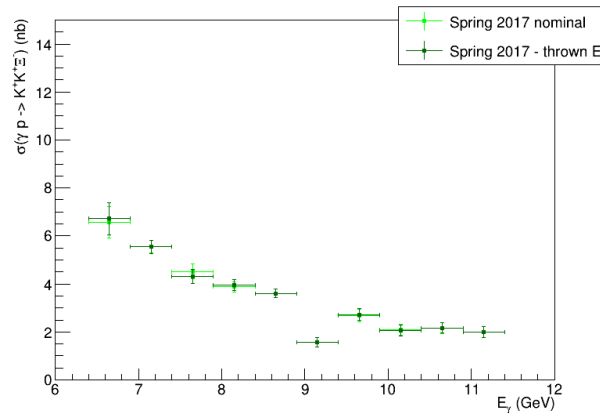


Figure 6.15: The total production cross section for $\gamma p \rightarrow K^+K^+\Xi^-$ as a function of incoming beam energy for the Spring 2017 data set using the generated beam energy (dark green) and reconstructed beam energy (light green) in the determination of the efficiency.

Figure 6.15 shows that this choice had minimal effect for the total cross section in this analysis. This is likely because of the fact that there are so few energy bins resulting in large ranges for each data point. There would be more of an effect for a channel with high statistics and thus finer energy binning.

Uniqueness Tracking. Uniqueness tracking is the handling of multiple combinations per event. If more than one hypotheses fits all the selection criteria required for a reaction, all are considered. The general approach is to only require that the particles needed for a measurement be required to be unique.

For example, consider a reaction with less final state particles such as $\gamma p \rightarrow p\phi \rightarrow pK^+K^-$. The beam photon along with the three final state particles may all be required to be unique. If only the ϕ invariant mass is of interest, multiple hypotheses for the proton do not necessarily need to be considered. Requiring the proton to be unique would falsely boost the statistics as the K^+K^- invariant mass for that event would be added to the histogram twice. In the case of multiple hypotheses for one of the kaons though, both should be considered and added to the histogram as the resultant KK invariant mass may not be the same between the hypotheses. In the case of more

complicated measurements than a straightforward invariant mass, the decision of which particles must be unique is nontrivial.

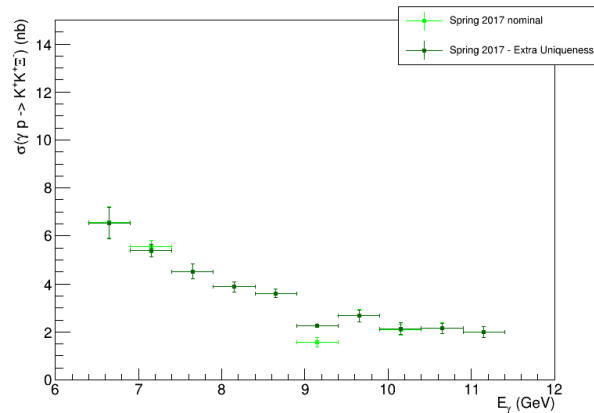


Figure 6.16: The total production cross section for $\gamma p \rightarrow K^+K^+\Xi^-$ as a function of incoming beam energy for the Spring 2017 data set using the nominal uniqueness tracking and tracking all particles.

In the case of the total cross section for $\Xi^-(1320)$, the nominal uniqueness tracking includes that of the beam photon, the t -channel produced kaon, the proton, and the two pions. Note, that the kaon from the decay of the intermediate hyperon is not normally tracked in this analysis. All the other particles are directly needed for the cross section measurement and the decay kaon is a bystander. The beam photon is needed both for the determining the beam energy as well as its timing information for accidental subtraction. The proton and the two pions definitely need to be tracked as they are used in determining the Ξ invariant mass. The t -channel produced kaon is needed for determining the momentum transfer t when each data point is split further for the differential cross section. Figure 6.16 shows the effect of including that additional kaon in the uniqueness tracking. Overall, the effect is small except for the energy bin directly after the coherent edge of the beam energy spectrum.

CHAPTER 7

SEARCH FOR EXCITED STATES

Previously in photoproduction, the only detected Cascade baryon resonances were the octet ground state $\Xi^-(1320)$ and the decuplet ground state $\Xi^-(1530)$, as shown in section 1.3.2. The first excitation band is comprised of the ground state particles with one unit of orbital angular momentum. For the Cascade baryons, the first excitation band is predicted to have seven states, two associated with the decuplet and five with the two octets.

The decuplet has intrinsic spin $S = 1/2$ and the octets have intrinsic spin of $1/2$ and $3/2$. When combined with one unit of orbital angular momentum $L = 1$, the resulting states have spin J and parity P of $J = S \otimes L$ and $P = (-1)^L$. For the decuplet, this results in the states with J^P of $3/2^-$, and $1/2^-$. For the octets, the expected states are: $5/2^-$, $3/2^-$, $3/2^-$, $1/2^-$, and $1/2^-$. Experimentally, all seven of these states are expected to be at or below 2 GeV in mass. There are currently five states known to varying degrees of certainty that possibly fit into this excitation band. These states and their evidence classification are: $\Xi(1620)$ (*), $\Xi(1690)$ (***) , $\Xi(1820)$ (***) , $\Xi(1950)$ (***) , and $\Xi(2030)$ (***) [1]. The state $\Xi(1820)$ has a $J^P = 3/2^-$ and the state $\Xi(2030)$ has $J = 5/2$ [1]. Of these remaining states, not much is experimentally known about their spin and parity. Assuming these five states are indeed in the first excitation band, there are at least two additional states that are completely unknown.

7.1 Channel Motivation for the Decay $\Xi^{-*} \rightarrow K^- \Lambda$

The two major decay modes for the lower mass excited states are $\Xi^* \rightarrow \Xi\pi$ and $\Xi^* \rightarrow KY$. There are also decay channels with smaller branching ratios to $\Xi^* \rightarrow \Xi\pi\pi$ via two-body through $\Xi(1530)$ or three-body decay and $\Xi^* \rightarrow KY\pi$ but these tend to be from excited states with mass higher than 2 GeV.

One can consider the spatial coordinates for the 3 quarks as two relative coordinates, one between a pair of quarks and the other between the third quark and the center of mass of the

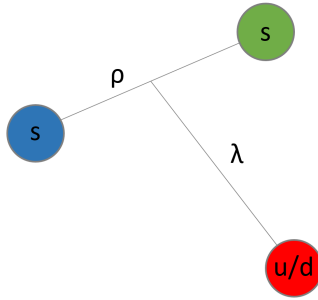


Figure 7.1: A depiction of the quark placement for a Cascade baryon.

pair [42]. For the ground state, the spatial component of the baryon wave-function needs to be symmetric. For a baryon with only light quarks (Nucleons and Deltas), it is trivial to symmetrize. When strange quarks are added in the case of Cascade baryons, the strange quarks must be the two quarks of the pair in order to maintain the desired symmetry due to the difference in mass of the quarks, as depicted in figure 7.1.

When a unit of orbital of angular momentum is added to a baryon, there are two options for where the excitation can occur: within the pair or between the pair and the third quark. In the case of all light quarks, the excitation in either place is equivalent. For the Cascade baryons, the excitation within the pair results in the lowest energy state. If the system is considered as two 3D harmonic oscillators, the reduced mass of the pair is greater than the reduced mass of the third quark with the pair. The excitation energy is proportional to the frequency $w = \sqrt{k/\mu}$. Therefore, assuming that the confinement potential is flavor independent (or k is the same in both cases), the excitation energy is lower for the pair.

When the excitation is between the pair of strange quarks, the decay to $\Xi\pi$ is suppressed resulting in the prominent decay to KY [42]. For each multiplet, the lowest mass excitation should decouple from $\Xi\pi$ and be seen in the decay to KY . Another benefit of the $\Xi\pi$ suppression is that the resulting excited states should be much more narrow than the heavier excited Cascade baryon states and than the analogous light quark baryons. The preferential decays can be understood by considering the quark content movement, which is shown in the quark line drawings in Figure 7.1.

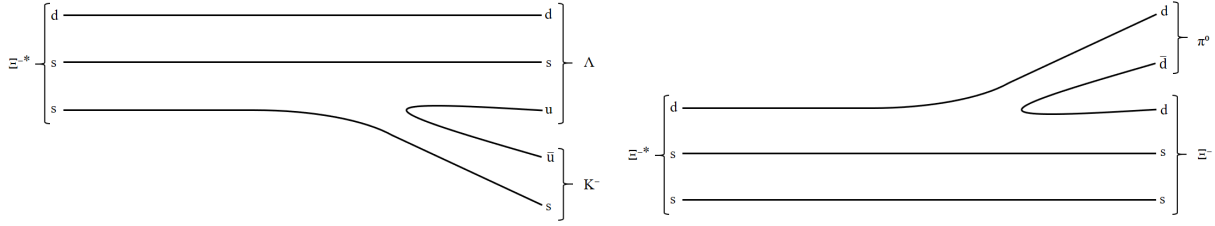


Figure 7.2: The quark line drawings for examples of the two major decays of an excited Cascade baryon within the first excitation band. If the excitation is between the strange quark pair, as with the lowest mass excitation, the state preferentially decays to KY or $K\Lambda$ as shown in the figure.

For $\Xi^{-*} \rightarrow KY$, there are a few full decay chains to consider. These include the primary decays to $K^{-}\Lambda$, $K^{-}\Sigma^0$, and $K^0\Sigma^{-}$. The secondary decays include $\Lambda \rightarrow p\pi^{-}$, $\Lambda \rightarrow n\pi^0$, $\Sigma^0 \rightarrow \Lambda\gamma$, $\Sigma^0 \rightarrow \Lambda\gamma\gamma$, $\Sigma^{-} \rightarrow n\pi^{-}$, additional decays of the K^0 , and subsequent decays of particles until reaching a 'stable' final state.

The most straight forward channel to look at with the GlueX detector is photoproduction of $K^+K^+\Xi^{-*}$ where $\Xi^{-*} \rightarrow K^{-}\Lambda$ and $\Lambda \rightarrow p\pi^{-}$. The reaction has the final state of $K^+K^+K^{-}\pi^{-}p$. Of the KY decays, this channel ends with the fewest final state particles and entirely consists of charged final state particles. There are several excited states that have a non-zero branching ratio for this decay mode. These states and their branching ratios include: $\Xi^{-}(1690)$ (seen), $\Xi^{-}(1820)$ (large), $\Xi^{-}(1950)$ (seen), $\Xi^{-}(2030)$ (~ 0.2), and $\Xi^{-}(2120)$ (seen) [1].

7.2 Event Selection

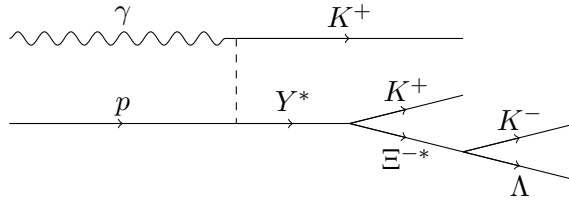


Figure 7.3: Feynman diagram for the reaction $\gamma p \rightarrow K^+K^+\Xi^{-*} \rightarrow K^+K^+K^-\Lambda$.

An initial look into this channel consisted of event selection to maximize purity. The requirements for the kinematic fit include: 4-momentum conservation, Λ mass constraint, and vertex constraints for the production reaction $\gamma p \rightarrow K^+ K^+ K^- \Lambda$, and the decay $\Lambda \rightarrow p \pi^-$. The event selection was performed using stringent particle identification timing, stringent χ^2/NDF of the kinematic fit, and a ϕ meson invariant mass veto. The change in timing requirements include being within 0.4ns for the kaons in the barrel calorimeter, 0.2ns for the kaons in the time-of-flight spectrometer, 0.8ns for the protons in the barrel calorimeter, and 0.5ns for protons in the time-of-flight spectrometer. The requirement for the kinematic fit is that the quality of the fit is within 2 for the χ^2/NDF .

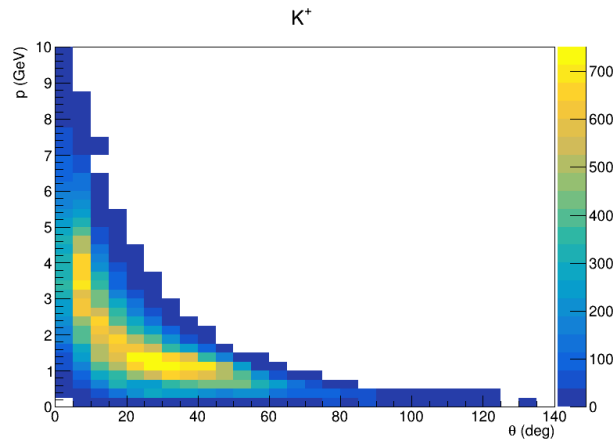


Figure 7.4: Example plot for momentum vs polar angular for all the experimental K^+ tracks for the Fall 2018 data set.

The Λ invariant mass spectrum is very clean with almost no apparent background, as required by the kinematic fit. By examining the various other combinations in the channel, it can be seen that there is a strong ϕ meson signal in the $K^+ K^-$ invariant mass spectrum, as seen in figure ???. Therefore, there is a strong presence of $\gamma p \rightarrow K^+ \phi \Lambda$. This results from either the reaction where the Λ and K^+ couple to the $N^*(1535)$ resonance as shown in the Feynman diagram in figure 7.5 [43] or from the reaction $\Lambda^* \rightarrow \Lambda \phi$. The K^+ and K^- both have a small polar angle and thus travel along the beam line, which may provide evidence of the former reaction. The ϕ meson has a mass of 1.02 GeV. All events in which the $K^+ K^-$ invariant mass fell between 1.00 to 1.05 GeV were removed.

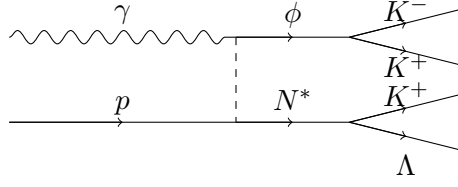


Figure 7.5: Possible reconstruction chains for background reaction $\gamma p \rightarrow \phi N^* \rightarrow K^+ K^+ K^- \Lambda$.

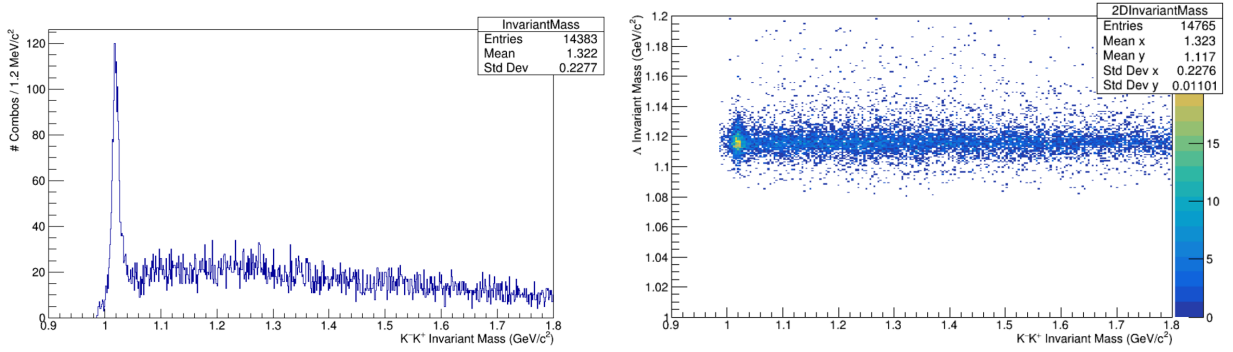


Figure 7.6: (left) Invariant mass histogram of K^+K^- showing strong signal for ϕ background; (right) Invariant mass of $p\pi^-$ versus the invariant mass K^+K^- showing clean signal Λ signal and clear correlation with ϕ .

7.2.1 Second Look

A subsequent look into this channel followed the approach of the $\Xi^-(1320)$ by removing the stringent timing requirements on the individual particles in each of the detectors. This new approach kept the process of removing the ϕ meson and χ^2/NDF requirement on the events. The effect of the χ^2/NDF can be seen for all the data sets in figure 7.7. It can be seen that for χ^2/NDF values greater than 3 are composed significantly of background.

This second look at the data added a requirement on the flight significance of the Λ . The Λ has a detached vertex of approximately 8cm which should be evident in the data. The flight significance is the path length traveled by the Λ before its decay divided by the uncertainty in that value. This value is shown in the units of σ . Therefore, a 5σ cut is that which keeps the events with a flight significance greater than 5. This value can be used to clean up the Λ distribution as the invariant mass is artificially clean.

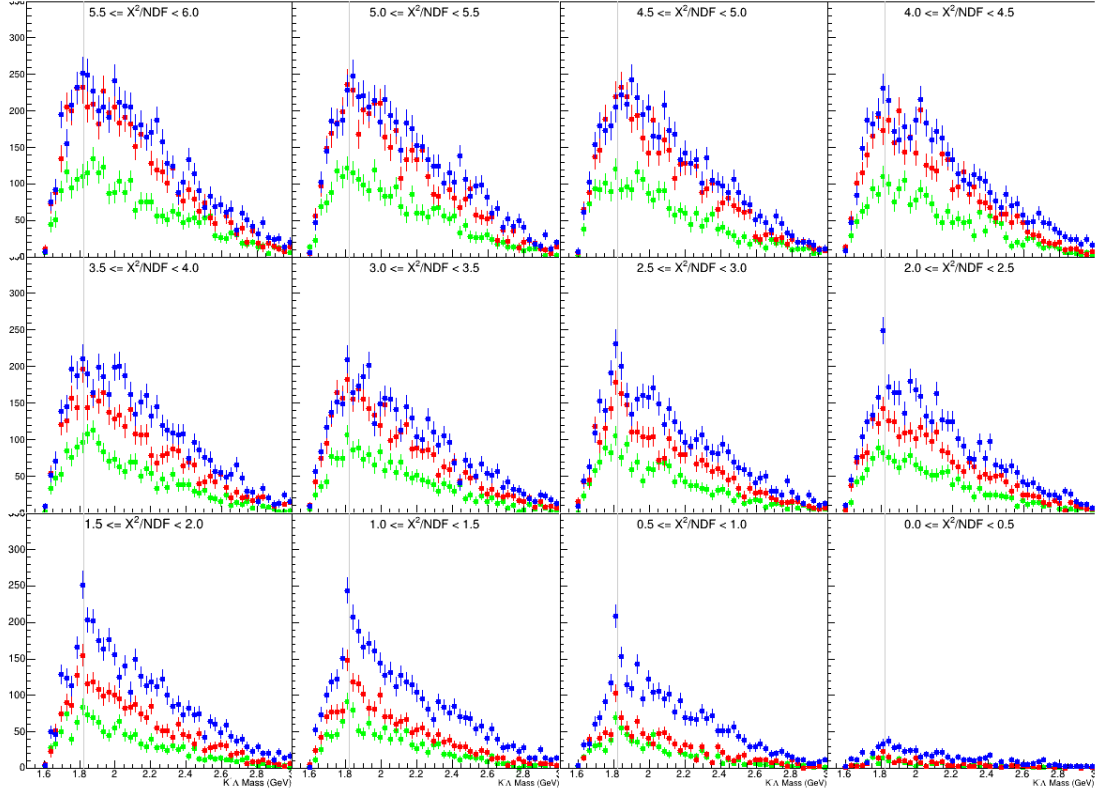


Figure 7.7: The distribution of the $K^- \Lambda$ invariant mass while stepping through the values for χ^2/NDF for Spring 2017 (green), Spring 2018 (red), and Fall 2018 (blue).

The distributions in figures 7.8 show the effect as the value is stepped through with a requirement that the χ^2/NDF is less than 5. Background in this distribution peaks at a flight significance of 0σ . The overall total distributions for both the χ^2/NDF and the flight significance versus the $K^- \Lambda$ invariant mass can be seen in figure 7.9. The band for $\Xi^-(1820)$ can be seen for low χ^2/NDF and for high values of the flight significance.

7.3 Results

After requiring these selection criteria and removing the scaled accidental beam photons, the resulting invariant mass distributions for $K^- \Lambda$ are shown for each data set in figure 7.10. These distributions require a χ^2/NDF less than 3.5, the same as $\Xi^-(1320)$, and a flight significance greater than 1σ . A possible signal for $\Xi^-(1820)$ is seen in each $K^- \Lambda$ invariant mass spectrum.

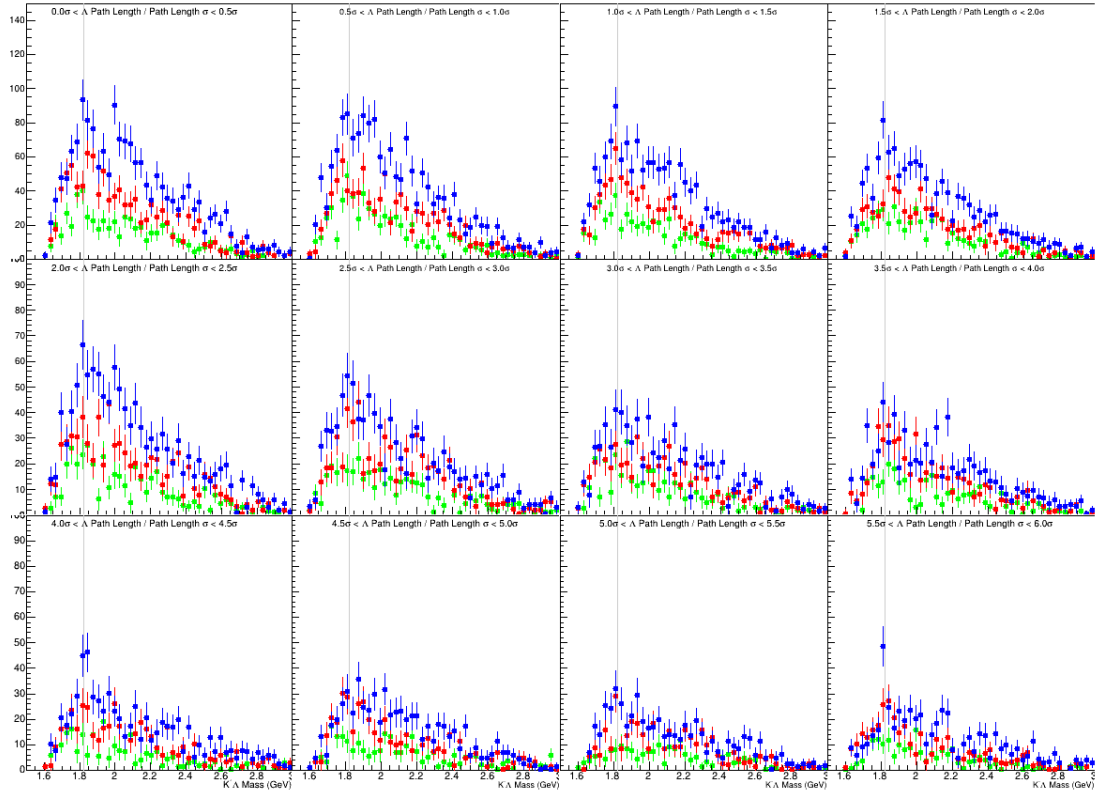


Figure 7.8: The distribution of the $K^- \Lambda$ invariant mass while stepping through the values for the flight significance for Spring 2017 (green), Spring 2018 (red), and Fall 2018 (blue).

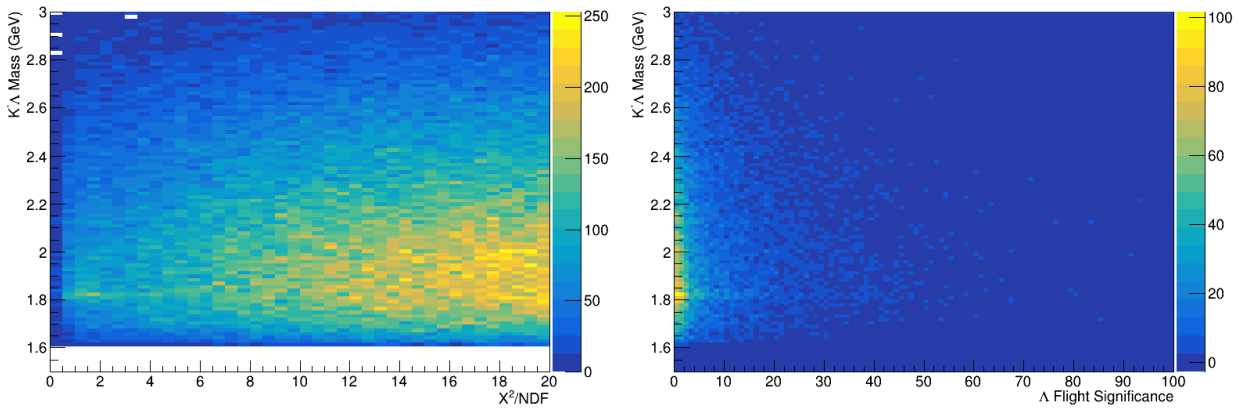


Figure 7.9: The distribution of the $K^- \Lambda$ invariant mass versus χ^2/NDF (left) and versus the flight significance of Λ for the Fall 2018 data set.

The signal is fit with a Voigtian function, which is a convolution of a Gaussian and a Breit-Wigner function. As detector resolution is comparable to that of the natural width for $\Xi^-(1820)$, both the natural width and the detector resolution account for the width of the peak. For this fit, the detector resolution was taken from the $\Xi^-(1320)$ invariant mass. The known width of for $\Xi^-(1820)$ is 24_{-10}^{+15} MeV [1]. The fit is allowed to vary from 15 Mev to 100 MeV.

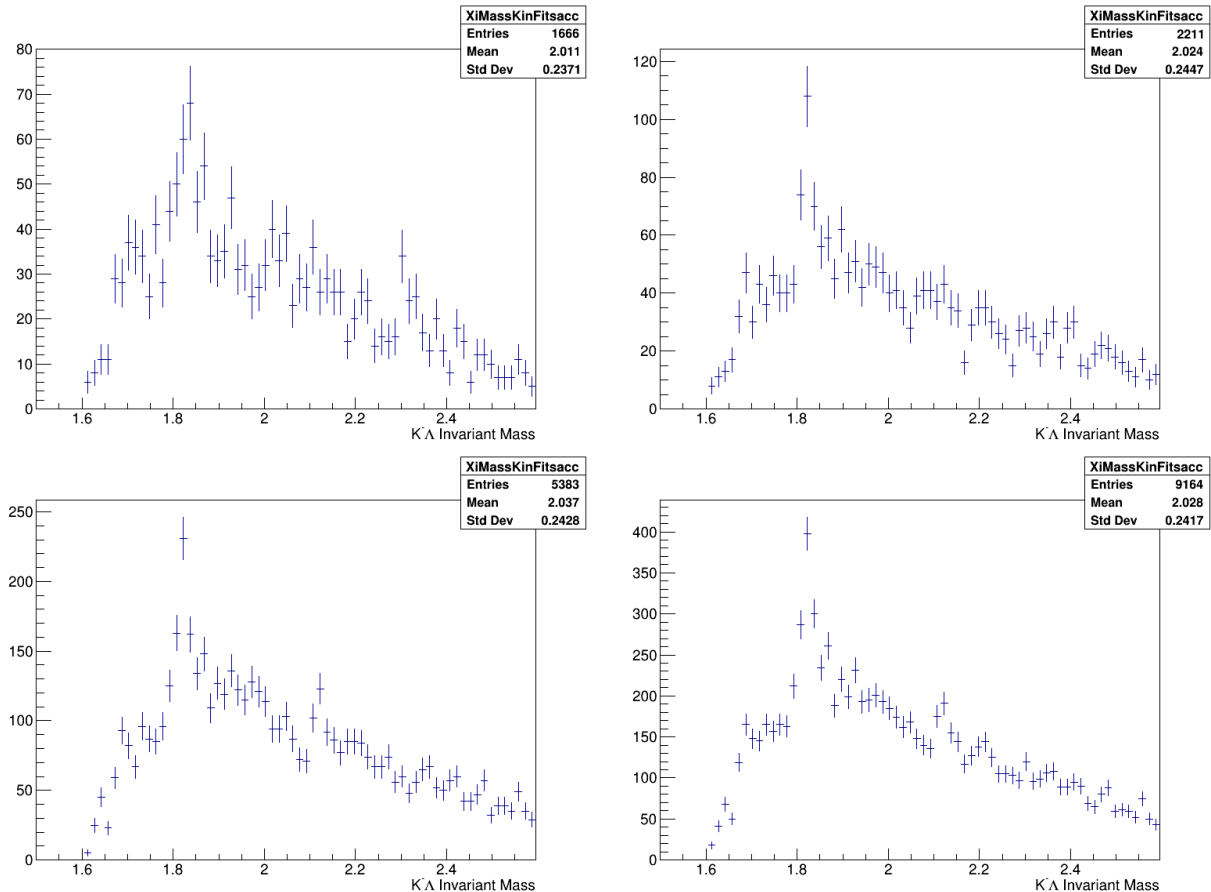


Figure 7.10: Invariant mass spectrum for ΛK^- for Spring 2017 (top left), Spring 2018 (top right), and Fall 2018 (bottom left). The combined distributions is shown in the bottom right. This decay channel has known branching ratios for the states: $\Xi^-(1690)$, $\Xi^-(1820)$, $\Xi^-(1950)$, $\Xi^-(2030)$, and $\Xi^-(2120)$ [1].

The background is modeled as a reverse Argus function. An Argus function is used to more accurately parametrize threshold behavior developed for the upper threshold of B meson decays [44]. This function has the form as shown in equation 7.1 where a and b are free parameters, m_0 is

the threshold mass, and m is invariant mass.

$$am\sqrt{1 - \frac{m^2}{m_0^2}} * e^{-b(1 - \frac{m^2}{m_0^2})} \quad (7.1)$$

The background in for Cascade baryon production rises from threshold, thus the Argus function is modified to reflect a production threshold, as shown in equation 7.2. In this case, a represents the number of background events, b is a free parameter, m_0 is the production threshold mass, and m is the $K\Lambda$ mass.

$$am\sqrt{\frac{m^2}{m_0^2} - 1} * e^{-b(\frac{m^2}{m_0^2} - 1)} \quad (7.2)$$

There is evidence for the excited Cascade baryon $\Xi^-(1820)$ with statistical fluctuations near the masses of other known excited states. The resulting fits are shown in figures 7.11. The threshold mass is consistent among all the fits at 1610 – 1611 MeV for three of the fits (Spring 2017, Spring 2018, and the combined data set). The Fall 2018 threshold mass is a bit different at 1623 MeV. The resulting width from each the fits varies from each data set from 42 MeV in Spring 2017, 15 MeV in Spring 2018, to 31 MeV in Fall 2018. The combined data set results in a width of 28 MeV.

The local significance of the peak at 1820 MeV is determined via a null hypothesis method using equation 7.3. This considers the difference in how good the resulting fit works with and without the added peak in the model.

$$Significance = \sqrt{[-2 \ln L(H_0)] - [-2 \ln L(H)]} \quad (7.3)$$

The peak for $\Xi^-(1820)$ is clearly in each of the distributions and more tenuous evidence for possible other excited states. The $\Xi^-(1820)$ peak has a significance of 4.4σ for Spring 2017, 6.4σ for Spring 2018, 9.2σ for Fall 2018, and 11.5σ for the combined data. The resultant combined GlueX Phase-I data have 694 ± 79 events. In order to do a meaningful analysis beyond the first observation of a state in the first excitation band, more events will be needed.

7.3.1 Second Look

After applying the new cuts to the data and removing the overly stringent timing cuts, the new distributions are shown in figure 7.12. The peak for $\Xi^-(1820)$ is still evident in the $K^-\Lambda$ invariant mass distributions, but with significantly more statistics. The re-evaluation of the selection criteria resulted in over three times the amount of signal events with the combined data. Figure 7.13 shows

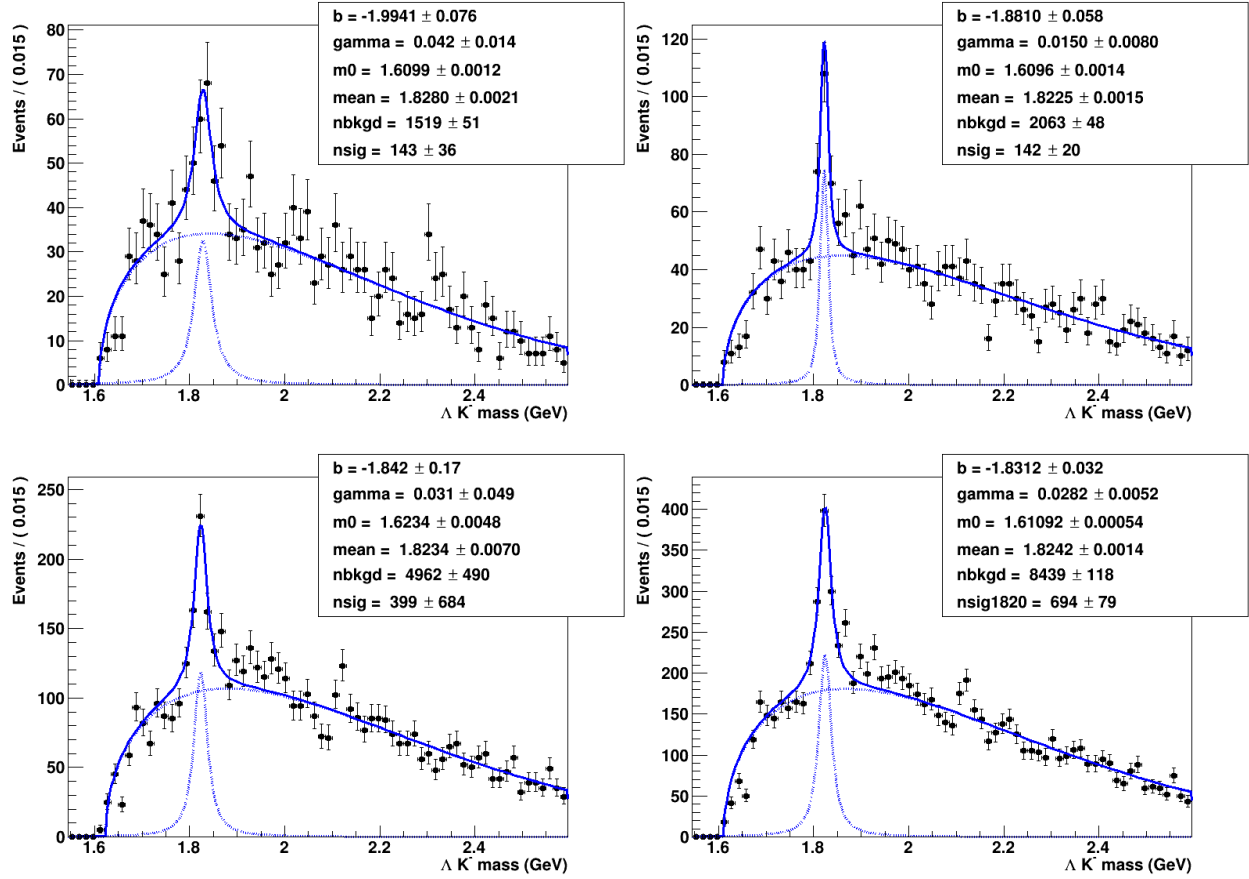


Figure 7.11: The fitted invariant mass spectrum for ΛK^- for Spring 2017 (top left), Spring 2018 (top right), and Fall 2018 (bottom left). The combined distributions is shown in the bottom right. This decay channel has known branching ratios for the states: $\Xi^-(1690)$, $\Xi^-(1820)$, $\Xi^-(1950)$, $\Xi^-(2030)$, and $\Xi^-(2120)$ [1].

these same histograms with the previously discussed fit applied. The peak for $\Xi^-(1820)$ now has a significance of 5.8σ for Spring 2017, 9.5σ for Spring 2018, 12.4σ for Fall 2018, and 16.6σ for the combined data. There is no doubt that $\Xi^-(1820)$ is in the data, which makes this the first state in the first excitation band to be seen in photoproduction. Additionally, there are other statistical fluctuations that need to be explored in these distributions. It is likely that there are other excited states within this reaction. There are several other states with known branching ratios to ΛK , such as $\Xi^-(1690)$, $\Xi^-(1950)$, $\Xi^-(2030)$, and $\Xi^-(2120)$.

Phase-II of GlueX should result in even more statistics, and as previously mentioned, will include the addition of the DIRC detector. Considering the momentum versus polar angle distribution

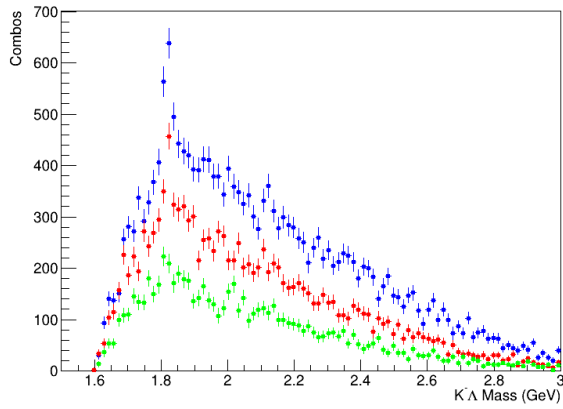


Figure 7.12: The invariant mass spectrum for ΛK^- for Spring 2017 (green), Spring 2018 (red), and Fall 2018 (blue) with the new selection requirements.

for this channel, shown in figure 7.4, it is obvious that increased pion/kaon separation at higher momentum will only improve the ability to detect these excited states. This should prove fruitful in the identification of the states within the first excitation band.

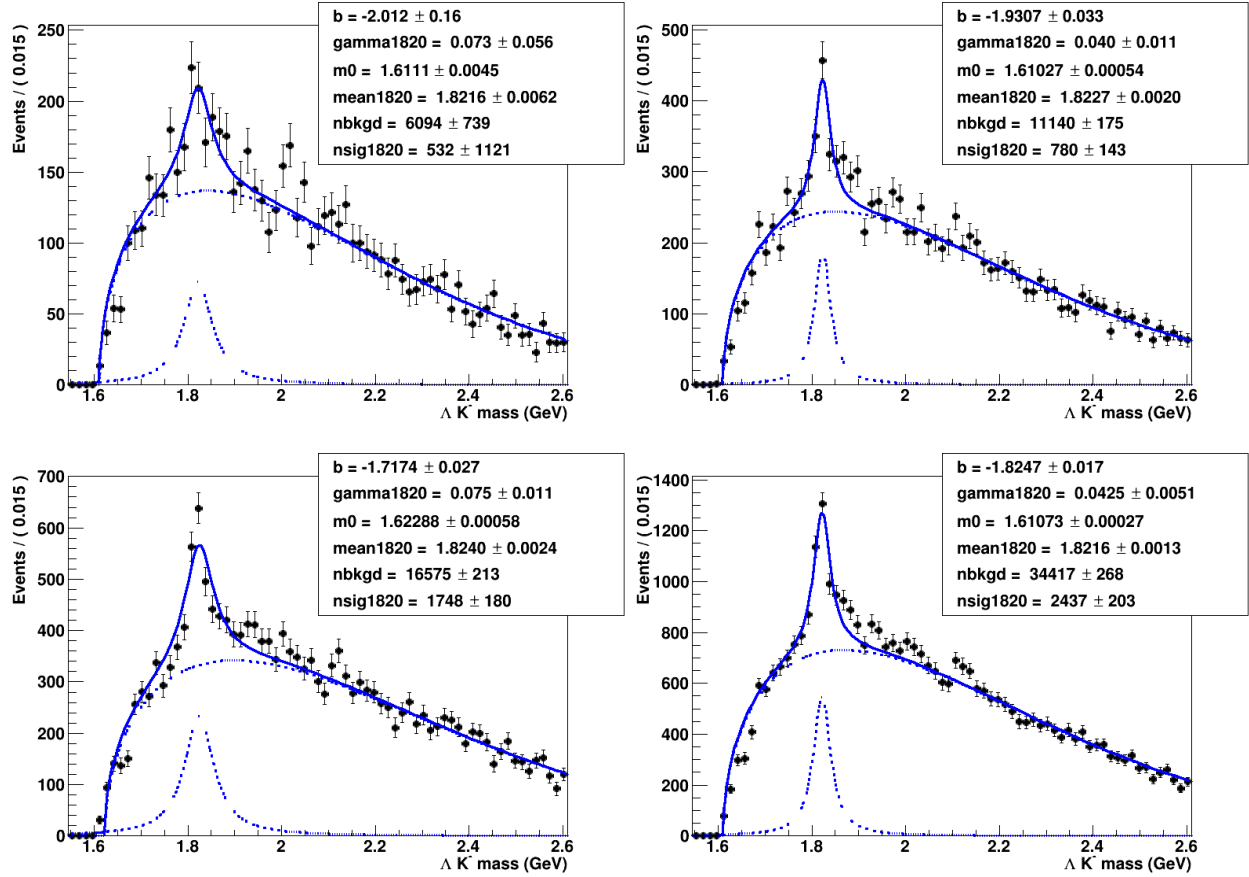


Figure 7.13: The new fitted invariant mass spectrum for ΔK^- for Spring 2017 (top left), Spring 2018 (top right), and Fall 2018 (bottom left). The combined distributions is shown in the bottom right. This decay channel has known branching ratios for the states: $\Xi^- (1690)$, $\Xi^- (1820)$, $\Xi^- (1950)$, $\Xi^- (2030)$, and $\Xi^- (2120)$ [1].

CHAPTER 8

SUMMARY AND OUTLOOK

Modern nuclear physics strives to understand the nature of the quarks and gluons in hadrons. The underlying patterns of hadrons are essential for understanding their structure. In order to understand the quantum chromodynamics, the full spectrum of hadrons and their properties is needed. Nucleons and Deltas have been extensively studied in previous experiments, particularly by the CLAS experiment at Jefferson Lab. Hyperons are the next logical step to study to understand QCD. The spectrum of hyperons is needed to further advance QCD. As the strangeness of a baryon increases, less is known about the corresponding states. GlueX has higher beam energies than previous photoproduction experiments. This work focused on doubly-strange baryons as determining the properties of known states and mapping out the spectrum of excited states is beneficial in understanding the underlying pattern of baryons.

The goal of this research is to improve the understanding of Cascade baryons. Only six resonances are certain to exist with at least 25 states expected based off of Nucleons and Deltas. Of the known states, only three have spin-parity measurements. This work shows some of the feasibility, and took the initial steps of a fruitful program. Several properties of the Cascade baryons are understudied and are of interest. These measurement of properties include: branching ratios, isospin mass splittings, cross sections, and polarization observables. The t -channel production mechanism is also not yet well understood. To aid in this, measurement of the properties of the intermediate hyperon, and of the exchange particle in a t -channel production mechanism will further the knowledge about the production mechanism.

This work discussed the production cross section of the ground state Cascade baryon. While some systematic uncertainties are still being studied before GlueX is ready to publish cross sections, this channel has shown useful in the progress of the collaboration. There are some differences apparent among the run periods which appear in all the channels under investigation in GlueX currently. The performance of the Monte Carlo efficiency and the inclusion of all of phase space is also being looked into.

This work also served as an initial look into the excited Cascade spectrum. There was a first observation of an excited state in photoproduction. A significant observation was made in the GlueX Phase-I data using stringent requirements on the events. Loosening the requirements and following an additional approach showed a more significant result with much more statistics. This shows the feasibility with other channels and regaining statistics through different approaches. Following this work, several other members of the collaboration are studying other decay channels of interest. At the end of this document in appendix B, several channels for all the known states are shown, many of which will be studied. There are still many channels to be studied within GlueX and improvements to be made for more observations of excited states.

The ground state Cascade baryon will continue to be studied with the GlueX Phase-I data. Other measurements of interest that are feasible include those previously mentioned as well as the parity of the ground state, and the beam asymmetry both for the intermediate hyperon and for the three-body production of the Cascade baryon. The ground state Cascade baryon parity measurement is of particular interest as it has never been measured. It decays weakly, which violates parity, and therefore the parity cannot be determined from the decay products. A possibility is to use the intermediate hyperons, such as Λ^* or Σ^* as a way to determine the parity of Cascade baryons. This also allows for determination of which excited hyperons are in fact the intermediate particles of the Cascade baryon reaction. It may be possible to use the angular distribution of the decay to determine the moments, which can then be related to the parity of the Cascade resonances [19, 41].

Baryon spectroscopy provides insight on the degrees of freedom associated with excited hadrons. In particular, studying multi-strange baryons will help in understanding the structure of all baryons since the parity of a baryon heavily depends on the internal structure. Multi-strange baryons are considered to be the link between light-flavor and the heavy-flavor regime. Thus, understanding the nature of the Cascade spectrum will provide useful insight of QCD in the non-perturbative regime.

APPENDIX A

TABULATED RESULTS

Contained in this appendix are the tabulated results for cross section as well as the values that make up the cross section.

Table A.1: The values for each run period used for the total cross section. The quoted uncertainty on all values is statistical.

Energy Bin (GeV)	Signal Yield	MC Yield	Thrown Yield	Efficiency*BR
– Run Period 2017-01: Reconstruction version 03, Analysis Launch version 20 –				
6.4 - 6.9	162 ± 14	411 ± 20	61320 ± 248	0.671 ± 0.033
6.9 - 7.4	152 ± 0	427 ± 21	52247 ± 229	0.816 ± 0.04
7.4 - 7.9	315 ± 20	1155 ± 34	131969 ± 363	0.875 ± 0.026
7.9 - 8.4	508 ± 26	2658 ± 52	277535 ± 527	0.958 ± 0.019
8.4 - 8.9	587 ± 28	3703 ± 61	369893 ± 608	1 ± 0.017
8.9 - 9.4	75 ± 9	1091 ± 33	111220 ± 333	0.981 ± 0.03
9.4 - 9.9	171 ± 15	1601 ± 40	155795 ± 395	1.03 ± 0.026
9.9 - 10.4	113 ± 12	1292 ± 36	134419 ± 367	0.961 ± 0.027
10.4 - 10.9	128 ± 13	1100 ± 33	117443 ± 343	0.936 ± 0.028
– Run Period 2018-01: Reconstruction version 02, Analysis Launch version 03 –				
6.4 - 6.9	291 ± 18	244 ± 16	49735 ± 223	0.49 ± 0.032
6.9 - 7.4	242 ± 18	284 ± 17	50678 ± 225	0.561 ± 0.033
7.4 - 7.9	509 ± 26	711 ± 27	120566 ± 347	0.59 ± 0.022
7.9 - 8.4	776 ± 33	1605 ± 40	255426 ± 505	0.628 ± 0.016
8.4 - 8.9	973 ± 37	2508 ± 50	365220 ± 604	0.687 ± 0.014
8.9 - 9.4	257 ± 19	631 ± 25	99693 ± 316	0.633 ± 0.025
9.4 - 9.9	337 ± 22	902 ± 30	141338 ± 376	0.638 ± 0.021
9.9 - 10.4	260 ± 19	825 ± 29	124303 ± 353	0.664 ± 0.023
10.4 - 10.9	273 ± 22	731 ± 27	106821 ± 327	0.685 ± 0.025
– Run Period 2018-08: Reconstruction version 02, Analysis Launch version 02 –				
6.4 - 6.9	291 ± 19	343 ± 19	49693 ± 223	0.69 ± 0.037
6.9 - 7.4	350 ± 23	399 ± 20	52063 ± 228	0.767 ± 0.039
7.4 - 7.9	586 ± 30	823 ± 29	113096 ± 336	0.727 ± 0.025
7.9 - 8.4	978 ± 36	2004 ± 45	260456 ± 510	0.769 ± 0.017
8.4 - 8.9	1057 ± 37	3053 ± 55	383466 ± 619	0.796 ± 0.014
8.9 - 9.4	328 ± 21	839 ± 29	102397 ± 320	0.819 ± 0.028
9.4 - 9.9	316 ± 22	1221 ± 35	142348 ± 377	0.858 ± 0.025
9.9 - 10.4	317 ± 21	1057 ± 33	133110 ± 365	0.794 ± 0.025
10.4 - 10.9	295 ± 20	904 ± 30	107062 ± 327	0.844 ± 0.028
– Run Period 2018-08 Low Energy: Reconstruction version 02, Analysis Launch version 05 –				
3 - 4.5	29 ± 5	101 ± 10	17382 ± 132	0.581 ± 0.058
4.5 - 6	53 ± 8	269 ± 16	24088 ± 155	1.12 ± 0.068

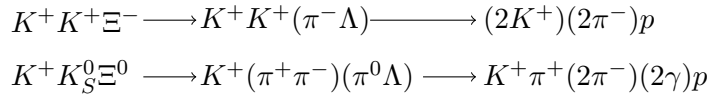
APPENDIX B

DECAY CHANNELS

Provided here are a subset of the decay modes that can be considered for a Cascade baryon analysis. Table B.1 shows all the possible decays listing in the Particle Data Group’s review for each particle and the corresponding branching ratios [1]. In the following reactions, only the subsequent decays that have the highest branching ratio are considered. This is done for two reasons. First it will be the overall reaction with the highest statistics due to the highest branching ratio. Secondly, the decay modes shown tend to be those with higher efficiencies for GlueX and are the decays that should be considered first and foremost. For example, in all cases the decay $\Lambda \rightarrow p\pi^-$ is used, while $\Lambda \rightarrow n\pi^0$ is never used.

After each construction of the decay modes, the known branching ratios for the known lowest mass states, up to $\Xi(2250)$, are included with the varying degrees of certainty. The quoted branching ratios include not known to decay via this mechanism (-), unknown branching ratio with little certainty (?), unknown branching ratio but known to decay via this process (seen), a qualitative branching ratio (small/large), and a quantitative branching ratio.

The two channels for the octet ground state Cascade baryons $\Xi(1320)$ are those shown in Figure B.1. These are the highest branching ratio decays of the octet ground state of the Ξ baryons. The two channels have the highest cross section of the Cascade baryons. These channels can be used to obtain the pseudo-two body beam asymmetries, cross sections, and isospin mass splittings. This analysis performed that of the cross section for the negatively-charged state.



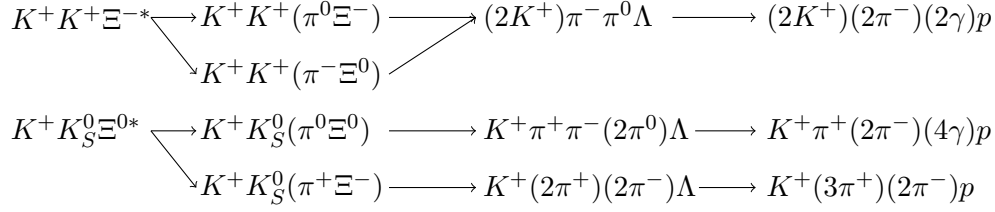
	$\Xi(1320)$	$\Xi(1530)$	$\Xi(1620)$	$\Xi(1690)$	$\Xi(1820)$	$\Xi(1950)$	$\Xi(2030)$	$\Xi(2120)$	$\Xi(2250)$
BR	> 0.99	-	-	-	-	-	-	-	-

Figure B.1: Possible reconstruction chains of interest for $\Xi \rightarrow \Lambda\pi$, the octet ground state using the previously mentioned decays. Branching ratios are those from the PDG and current as of the 2019 update [1].

Table B.1: Decay channels of interest and branching ratios from the PDG Review [1]

Decay	BR	Decay	BR	Decay	BR
$\Xi^0 \rightarrow \Lambda\pi^0$	0.995	$\Xi(1530) \rightarrow \Xi\pi$	1	$\Xi(1620) \rightarrow \Xi\pi$?
$\Xi^- \rightarrow \Lambda\pi^-$	0.999	$\rightarrow \Xi\gamma$	< 0.04		
$\Xi(1690) \rightarrow \Lambda K$	seen	$\Xi(1820) \rightarrow \Lambda K$	large	$\Xi(1950) \rightarrow \Lambda K$	seen
$\rightarrow \Sigma K$	seen	$\rightarrow \Sigma K$	small	$\rightarrow \Sigma K$	possibly
$\rightarrow \Xi\pi$	seen	$\rightarrow \Xi\pi$	small	$\rightarrow \Xi\pi$	seen
$\rightarrow \Xi(1530)\pi$?	$\rightarrow \Xi(1530)\pi$	small	$\rightarrow \Xi(1530)\pi$?
$\rightarrow \Xi\pi\pi$	possibly	$\rightarrow \Xi\pi\pi$?	$\rightarrow \Xi\pi\pi$?
$\Xi(2030) \rightarrow \Lambda K$	~ 0.2	$\Xi(2120) \rightarrow \Lambda K$	seen	$\Xi(2250) \rightarrow \Xi\pi\pi$?
$\rightarrow \Sigma K$	~ 0.8			$\rightarrow \Lambda K\pi$?
$\rightarrow \Xi\pi$	small			$\rightarrow \Sigma K\pi$?
$\rightarrow \Xi(1530)\pi$	small				
$\rightarrow \Xi\pi\pi$	small				
$\rightarrow \Lambda K\pi$	small				
$\rightarrow \Sigma K\pi$	small				
$\Xi(2370) \rightarrow \Lambda K\pi$	seen	$\Xi(2500) \rightarrow \Lambda K$?		
$\rightarrow \Sigma K\pi$	seen	$\rightarrow \Sigma K$?		
$\rightarrow \Omega K$?	$\rightarrow \Xi\pi$?		
$\rightarrow \Lambda K^*(892)$?	$\rightarrow \Xi(1530)\pi$?		
$\rightarrow \Sigma K^*(892)$?	$\rightarrow \Xi\pi\pi$	seen		
$\rightarrow \Sigma(1385)K$?	$\rightarrow \Lambda K\pi$	seen with \downarrow		
		$\rightarrow \Sigma K\pi$	seen with \uparrow		
$\Lambda \rightarrow p\pi^-$	0.64	$\Sigma^+ \rightarrow p\pi^0$	0.52	$\Sigma^0 \rightarrow \Lambda\gamma$	1
$\rightarrow n\pi^0$	0.36	$\rightarrow n\pi^+$	0.48	$\rightarrow \Lambda\gamma\gamma$	< 0.03
$\Sigma^- \rightarrow n\pi^-$	0.998	$\pi^0 \rightarrow \gamma\gamma$	0.988		
$K_S^0 \rightarrow \pi^+\pi^-$	0.69	$K_L^0 \rightarrow \pi^0\pi^0\pi^0$	0.195		
$\rightarrow \pi^0\pi^0$	0.31	$\rightarrow \pi^+\pi^-\pi^0$	0.125		
		$\rightarrow \pi^\pm e^\mp \nu_e$	0.406		

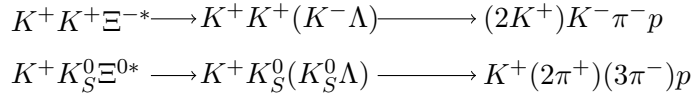
The reactions shown in figure B.2 have the next highest cross section and is a channel of interest. The $\Xi^* \rightarrow \Xi\pi$ decay is the primary decay for $\Xi(1530)$ which is the ground state of the decuplet and analogous to a ground state Δ baryon. This decay channel is also of particular interest because it is the only known decay of the $\Xi(1620)$, a one-star state. This state has only recently been seen at BELLE after not being seen since the 1980s [45]. This channel is currently under study by fellow GlueX collaboration members.



	$\Xi(1320)$	$\Xi(1530)$	$\Xi(1620)$	$\Xi(1690)$	$\Xi(1820)$	$\Xi(1950)$	$\Xi(2030)$	$\Xi(2120)$	$\Xi(2250)$
BR	-	1	?	seen	small	seen	small	-	-

Figure B.2: Possible reconstruction chains of interest for $\Xi^* \rightarrow \Xi\pi$ using the previously mentioned decays. Branching ratios are those from the PDG and current as of the 2019 update [1].

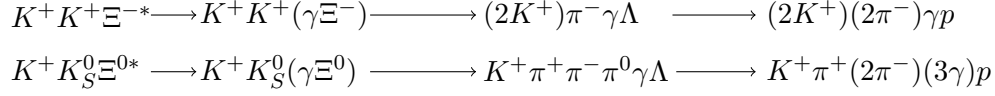
Another channel that has been extensively studied by this analysis (chapter 7) is the reaction shown in Figure B.3. This reaction is believed to be the largest branching ratio for the $\Xi(1820)$ which is predicted to be the first excitation of the decuplet ground state, $\Xi(1530)$. The first reaction of the two shown in the figure is of particular interest because of the expectation that it should be a narrow state due to its decoupling from the more common π decay ($\Xi^* \rightarrow \Xi\pi$) as discussed in 7.1. At the start of the analysis, there was no previous observation of an excited resonance of the Ξ baryons using photoproduction.



	$\Xi(1320)$	$\Xi(1530)$	$\Xi(1620)$	$\Xi(1690)$	$\Xi(1820)$	$\Xi(1950)$	$\Xi(2030)$	$\Xi(2120)$	$\Xi(2250)$
BR	-	-	-	seen	large	seen	~ 0.2	seen	-

Figure B.3: Possible reconstruction chains of interest for $\Xi^* \rightarrow \Lambda K$ using the previously mentioned decays. Branching ratios are those from the PDG and current as of the 2019 update [1].

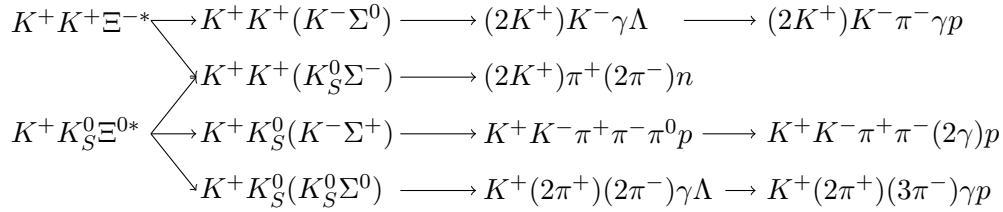
The reactions shown in figure B.4 are a radiative decay known for the decuplet ground state $\Xi(1530)$. Not much is known about this decay mechanism. The branching ratio quoted here is an upper limit on the branching ratio of less than 4%. While this channel will be experimentally complicated to study because of its small branching ratio and lone photon, it is a useful channel in providing information about the form factors.



	$\Xi(1320)$	$\Xi(1530)$	$\Xi(1620)$	$\Xi(1690)$	$\Xi(1820)$	$\Xi(1950)$	$\Xi(2030)$	$\Xi(2120)$	$\Xi(2250)$
BR	-	< 0.04	-	-	-	-	-	-	-

Figure B.4: Possible reconstruction chains of interest for $\Xi \rightarrow \Xi \gamma$ using the previously mentioned decays. Branching ratios are those from the PDG and current as of the 2019 update [1].

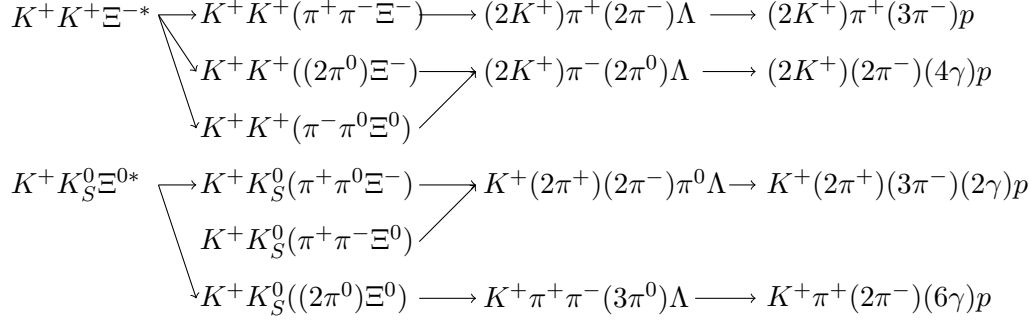
Analogous to the ΛK decay channel, there are also several ΣK decay channels as the Σ baryon has 3 isospin related states. These channels are more computational complicated than the $K\Lambda$ as each either has photons or an intermediate Λ baryon to consider.



	$\Xi(1320)$	$\Xi(1530)$	$\Xi(1620)$	$\Xi(1690)$	$\Xi(1820)$	$\Xi(1950)$	$\Xi(2030)$	$\Xi(2120)$	$\Xi(2250)$
BR	-	-	-	seen	small	possibly	~ 0.8	-	-

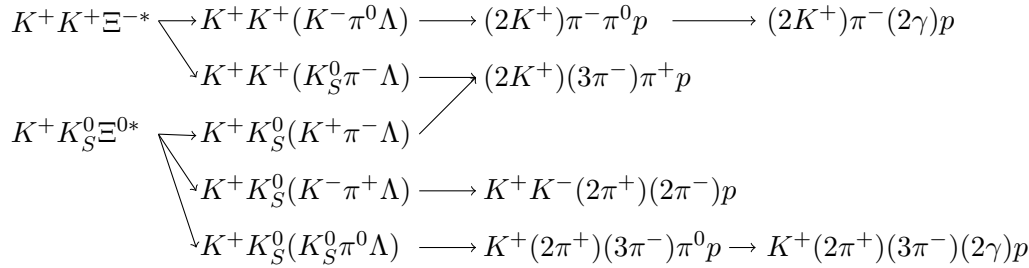
Figure B.5: Possible reconstruction chains of interest for $\Xi^* \rightarrow \Sigma K$ using the previously mentioned decays. Branching ratios are those from the PDG and current as of the 2019 update [1].

The last two decay mechanisms of interest are of those for higher mass excited states as shown in figures B.6 and B.7. They are at the limit of what GlueX can see experimentally. These include the decay $\Xi^* \rightarrow \Xi \pi \pi$ and $\Xi^* \rightarrow KY \pi$, respectively. Both of these will likely be the last of the Ξ channels to consider at GlueX.



	$\Xi(1320)$	$\Xi(1530)$	$\Xi(1620)$	$\Xi(1690)$	$\Xi(1820)$	$\Xi(1950)$	$\Xi(2030)$	$\Xi(2120)$	$\Xi(2250)$
BR: 2-body	-	-	-	?	small	?	small	-	-
BR: 3-body	-	-	-	possibly	?	?	small	-	?

Figure B.6: Possible reconstruction chains of interest for $\Xi^* \rightarrow \Xi \pi \pi$ through a three-body decay or via a two-body decay with an intermediate $\Xi(1530)$ using the previously mentioned decays in B.2. Branching ratios are those from the PDG and current as of the 2019 update [1].



	$\Xi(1320)$	$\Xi(1530)$	$\Xi(1620)$	$\Xi(1690)$	$\Xi(1820)$	$\Xi(1950)$	$\Xi(2030)$	$\Xi(2120)$	$\Xi(2250)$
BR	-	-	-	-	-	-	small	-	?

Figure B.7: Possible reconstruction chains of interest for $\Xi^* \rightarrow K \Lambda \pi$ using the previously mentioned decays. Branching ratios are those from the PDG and current as of the 2019 update [1].

BIBLIOGRAPHY

- [1] M. Tanabashi et al. Review of Particle Physics. *Phys. Rev. D*, 98(3):030001, 2018.
- [2] Charles M. Jenkins et al. Existence of Xi Resonances Above 2-gev. *Phys. Rev. Lett.*, 51:951–954, 1983.
- [3] Spring 2017 analysis launch cuts. https://halldweb.jlab.org/wiki/index.php/Spring_2017_Analysis_Launch_Cuts, December 2017.
- [4] Siegfried Bethke. Experimental tests of asymptotic freedom. *Prog. Part. Nucl. Phys.*, 58:351–386, 2007.
- [5] Robert G. Edwards, Nilmani Mathur, David G. Richards, and Stephen J. Wallace. Flavor structure of the excited baryon spectra from lattice QCD. *Phys. Rev. D*, 87(5):054506, 2013.
- [6] Jefferson Lab photos. <https://www.flickr.com/photos/jeffersonlab/>, June 2017.
- [7] L. Guo et al. Cascade production in the reactions $\gamma p \rightarrow K^+ K^+ (X)$ and $\gamma p \rightarrow K^+ K^+ \pi^- (X)$. *Phys. Rev.*, C76:025208, 2007.
- [8] J. T. Goetz et al. Study of Ξ^* Photoproduction from Threshold to $W = 3.3$ GeV. *Phys. Rev.*, C98(6):062201, 2018.
- [9] H. Al Ghoul et al. Measurement of the beam asymmetry Σ for π^0 and η photoproduction on the proton at $E_\gamma = 9$ GeV. *Phys. Rev. C*, 95(4):042201, 2017.
- [10] M. Dugger and others. Hall D / GlueX Technical Construction Report. 2017.
- [11] Eric Pooser et al. The GlueX Start Counter Detector. *Nucl. Instrum. Meth. A*, 927:330–342, 2019.
- [12] GlueX photos. <https://gluexweb.jlab.org/photos/>, June 2017.
- [13] M. Dugger et al. A study of decays to strange final states with GlueX in Hall D using components of the BaBar DIRC. 8 2014.
- [14] M. Dugger et al. A study of meson and baryon decays to strange final states with GlueX in Hall D (A proposal to the 39th Jefferson Lab Program Advisory Committee). 10 2012.
- [15] Ani Aprahamian et al. Reaching for the horizon: The 2015 long range plan for nuclear science. 10 2015.

- [16] David J. Gross and Frank Wilczek. Ultraviolet Behavior of Nonabelian Gauge Theories. *Phys. Rev. Lett.*, 30:1343–1346, 1973.
- [17] H.David Politzer. Reliable Perturbative Results for Strong Interactions? *Phys. Rev. Lett.*, 30:1346–1349, 1973.
- [18] D. Teodoro et al. A Spin Determination of the Ξ^* (1820) Resonance. *Phys. Lett. B*, 77:451–453, 1978.
- [19] S.F. Biagi et al. Ξ^* Resonances in Ξ - Be Interactions. 2. Properties of Ξ (1820) and Ξ (1960) in the Lambda anti-K0 and Sigma-0 anti-K0 Channels. *Z. Phys. C*, 34:175, 1987.
- [20] B.A. Mecking et al. The CEBAF Large Acceptance Spectrometer (CLAS). *Nucl. Instrum. Meth. A*, 503:513–553, 2003.
- [21] K. Nakayama et al. Photoproduction of Ξ off nucleons. *Phys. Rev. C*, 74:035205, 2006.
- [22] GlueX Collaboration. <http://www.gluex.org/Gluex/Collaboration.html>, June 2020.
- [23] S. Adhikari et al. The GlueX Beamline and Detector. 5 2020.
- [24] C.W. Leemann, D.R. Douglas, and G.A. Krafft. The Continuous Electron Beam Accelerator Facility: CEBAF at the Jefferson Laboratory. *Ann. Rev. Nucl. Part. Sci.*, 51:413–450, 2001.
- [25] M. Dugger et al. Design and construction of a high-energy photon polarimeter. *Nucl. Instrum. Meth. A*, 867:115–127, 2017.
- [26] S. Adhikari et al. Beam Asymmetry Σ for the Photoproduction of η and η' Mesons at $E_\gamma = 8.8$ GeV. *Phys. Rev. C*, 100(5):052201, 2019.
- [27] S. Adhikari et al. Measurement of the Photon Beam Asymmetry in $\vec{\gamma}p \rightarrow K^+\Sigma^0$ at $E_\gamma = 8.5$ GeV. 3 2020.
- [28] F. Barbosa and others. Pair spectrometer hodoscope for Hall D at Jefferson Lab. *Nucl. Instrum. Meth. A*, 795:376–380, 2015.
- [29] N.S. Jarvis et al. The Central Drift Chamber for GlueX. *Nucl. Instrum. Meth. A*, 962:163727, 2020.
- [30] L. Pentchev et al. Studies with cathode drift chambers for the GlueX experiment at Jefferson Lab. *Nucl. Instrum. Meth. A*, 845:281–284, 2017.
- [31] Tegan D. Beattie et al. Construction and Performance of the Barrel Electromagnetic Calorimeter for the GlueX Experiment. *Nucl. Instrum. Meth. A*, 896:24–42, 2018.

- [32] K. Moriya et al. A measurement of the energy and timing resolution of the GlueX Forward Calorimeter using an electron beam. *Nucl. Instrum. Meth. A*, 726:60–66, 2013.
- [33] S. Agostinelli et al. GEANT4: A Simulation toolkit. *Nucl. Instrum. Meth. A*, 506:250–303, 2003.
- [34] P. Mattione. Least Squares Kinematic Fitting of Physics Reactions. 2016.
- [35] P. Avery. Applied Fitting Theory VI. 1999.
- [36] J.W. Rohlf. *Modern Physics from alpha to Z0*. Wiley, 1994.
- [37] W Verkerke and D Kirkby. Roofit users manual, Sep 2019.
- [38] MCwrapper. https://github.com/JeffersonLab/gluex_MCwrapper.
- [39] P. Eugenio. Genr8: A General Monte Carlo Event Generator. 1998.
- [40] Mark Mitchell et al. Engauge Digitizer: Version 11.2 , May 2019.
- [41] K. Nakayama et al. Model-independent determination of the parity of Ξ hyperons. *Phys. Rev. C*, 85:042201, 2012.
- [42] Kuang-Ta Chao, Nathan Isgur, and Gabriel Karl. Strangeness -2 and -3 Baryons in a Quark Model With Chromodynamics. *Phys. Rev. D*, 23:155, 1981.
- [43] Qi-Fang L et al. Nucleon resonances in the $\gamma p \rightarrow \phi K^+ \Lambda$ reaction near threshold. *Phys. Rev. C*, 91(3):035204, 2015.
- [44] H. Albrecht et al. Measurement of the polarization in the decay $B \rightarrow J / \psi K^*$. *Phys. Lett. B*, 340:217–220, 1994.
- [45] M. Sumihama et al. Observation of $\Xi(1620)^0$ and evidence for $\Xi(1690)^0$ in $\Xi_c^+ \rightarrow \Xi^- \pi^+ \pi^+$ decays. *Phys. Rev. Lett.*, 122(7):072501, 2019.

BIOGRAPHICAL SKETCH

I attended a small private school, Ohio Northern University (ONU) for my undergraduate education where I earned a Bachelor's of Science as a double major in Physics and Applied Mathematics in 2015. During my time at ONU, I was able to participate in several research groups including research in computational solid state physics, mathematical physics, and computational physical chemistry. I also had the opportunity to intern at Argonne National Laboratory performing research in accelerator physics. The research in solid state, mathematical, and accelerator physics are described in the following paragraphs.

My main research project during my undergraduate career consisted of computationally determining surface characteristics for doped semiconductors. Under the guidance of Dr. Mellita Caragiu at ONU, and in collaboration with the research group of Dr. R. Diehl, at Penn State University, I conducted computational solid state physics to create theoretical energy versus intensity graphs for electron scattering in low energy electron diffraction. These graphs are then compared to experimental results obtained by Dr. Diehl's research group. By comparing the experimental with theoretical results, we were able to determine the geometrical coordinates of atoms that are adsorbed to surfaces. I worked with Dr. Caragiu for nearly 3 years, and during this project I earned a departmental research award every year I was a part of the project. I am very grateful for the experience and opportunity. The knowledge gained has been invaluable, both in research practices and academic knowledge, as I feel that this experience helped me to become a better scientist.

My senior year I started a research project exploring the mathematics behind problems pertaining to nuclear isospin in systems of particles, under the guidance of Dr. Bill Fuller at ONU. The project included deriving the multiplets for many particle systems from the representation of the individual isospins as well as examining the coherent spin states. The goal of the project was to receive an introduction to the representation theory of Lie groups and its application to particle and nuclear physics. This research resulted in me being awarded the William Rowan Hamilton Research award which is presented to one student who performed outstanding research in applied mathematics. It was a part of my senior capstone for my major in mathematics, and was used as a way to bridge the gap to research in hadronic physics.

I was fortunate to be able to participate in an internship at Argonne National Laboratory for the summer of 2014. This internship was specifically within the Accelerator Systems Division of the Advanced Photon Source under the Lee Teng Undergraduate Internship in Accelerator Science and Engineering. As an added benefit that has been immensely invaluable, I was sent to the US Particle Accelerator School. I successfully completed the Fundamentals of Accelerator Physics and Technology course combined with the Simulations and Measurements Lab. This intensive two week course provided me with working knowledge of the many kinds of accelerators and their components, which I was able to directly apply to my summer research project. Under Dr. Ali Nassiri and Dr. Bob Kustom, I conducted initial design simulations using Microwave Studio for a sample of magnesium diboride in a fabryperot open resonator. The project is working towards finding a method to use this material in cryogenfree radio frequency cavities. The use of magnesium diboride in radio frequency cavities would allow for operation at higher temperatures and for a higher accelerating gradient beyond the limit caused by the quench field of niobium.

I started at Florida State University in the Fall of 2015, where I joined the research group lead by Dr. Volker Crede that semester. During the summer of 2016, I started the work presented here. The proposal for which granted me the National Science Foundation Graduate Research Fellowship to fund the next three academic years. The work presented here was shown at the International Conference on Meson-Nucleon Physics at Carnegie Melon in 2019, at APS Division of Nuclear Physics National Meeting in Pittsburgh in 2017, at the Jefferson Lab Users Organization meeting in 2019, at 8 of the 12 GlueX Collaboration meetings that occurred during my tenure with GlueX, and at 4 seminars in the Physics department or at the University.

During my time with the GlueX Collaboration, I started and convened the hyperon working group for its entirety. The group started in April 2019 as an informal meeting and was promoted to an official GlueX meeting in July 2019. As convener of the working group, I was one of five analysis leaders under the Physics Analysis Coordinator. My time as convener working group presented me with valuable experience mentoring other graduate students around the globe. In June 2020, this meeting was retired as the GlueX working groups were restructured.

In April 2020, due to the combination of the work described herein and my leadership in GlueX, I was awarded the John D. Fox scholarship in nuclear physics by the Department of Physics at Florida State University.